

Alma Mater Studiorum – Università di Bologna

DOTTORATO DI RICERCA IN
Disegno e Metodi dell'Ingegneria Industriale

Ciclo XXII

Settore scientifico-disciplinare di afferenza: ING-IND06

TITOLO TESI

Experimental analysis of coaxial jets: instability, flow and
mixing characterization

Presentata da: Antonio Segalini

Coordinatore Dottorato

Relatore

Prof.Ing. Franco Persiani

Prof.Ing. Alessandro Talamelli

Esame finale anno 2010

©Antonio Segalini 2010

Antonio Segalini 2010, **Experimental analysis of coaxial jets: instability, flow and mixing characterization**

II Facoltà di ingegneria, 47121 Forlì, Italy

Abstract

The velocity and mixing field of two turbulent jets configurations have been experimentally characterized by means of cold- and hot-wire anemometry in order to investigate the effects of the initial conditions on the flow development. In particular, experiments have been focused on the effect of the separation wall between the two streams on the flow field. The results of the experiments have pointed out that the wake behind a thick wall separating wall has a strong influence on the flow field evolution. For instance, for nearly unitary velocity ratios, a clear vortex shedding from the wall is observable. This phenomenon enhances the mixing between the inner and outer shear layer. This enhancement in the fluctuating activity is a consequence of a local absolute instability of the flow which, for a small range of velocity ratios, behaves as a hydrodynamic oscillator with no sensibility to external perturbations. It has been suggested indeed that this absolute instability can be used as a passive method to control the flow evolution.

Finally, acoustic excitation has been applied to the near field in order to verify whether or not the observed vortex shedding behind the separating wall is due to a global oscillating mode as predicted by the theory. A new scaling relationship has been also proposed to determine the preferred frequency for nearly unitary velocity ratios. The proposed law takes into account both the Reynolds number and the velocity ratio dependence of this frequency and, therefore, improves all the previously proposed relationships.

*Everything should be made as simple as possible, but not one bit simpler.*¹

Albert Einstein (1879–1955)

¹Personal re-reading. *Many industrial burners can be schematized as coaxial jets, but not single jets*

Contents

Abstract	ii
Chapter 1. Introduction	1
Chapter 2. Fluid dynamics background	8
2.1. Instability backgrounds	12
2.2. Classical shear layers	14
2.3. Coaxial jets	21
Chapter 3. Experimental setup	32
3.1. The facility	32
3.2. Measurement techniques	35
3.3. Experiments with acoustic excitation	39
3.4. Initial conditions	41
3.5. Accuracy Tests	42
Chapter 4. Effects of vortex shedding in the near field	46
4.1. Generalities	46
4.2. Vortex shedding effect on interacting shear layers	47
4.3. Vortex shedding as a passive flow control mechanism	50
4.4. Vortex shedding effect on the turbulence activity	51
Chapter 5. Dominant instabilities in the near field	55
5.1. Generalities	55
5.2. Low velocity ratio region	56
5.3. High velocity ratio region	58
5.4. Intermediate velocity ratio region	60
Chapter 6. Flow and mixing in coaxial jets with different initial conditions	67
6.1. Generalities	67

6.2. Centerline analysis	68
6.3. Velocity profiles	69
6.4. Concentration profiles	78
6.5. Spectral analysis	81
6.6. Conditional sampling analysis	89
6.7. Reynolds and heat fluxes	90
6.8. Joint probability density functions	95
Chapter 7. Effect of acoustic forcing in the near field	100
7.1. Generalities	100
7.2. Acoustic excitation effects	101
Chapter 8. Conclusions	111
Appendix A. The effect of oblique waves on jet turbulence	115
A.1. Introduction	115
A.2. Experimental setup	116
A.3. Results, discussion and conclusions	117
Appendix B. Effect of probe alignment error in the mean and rms estimation of a turbulent boundary layer	120
B.1. Generalities	120
B.2. Theoretical results	120
B.3. Numerical results	126
Acknowledgements	132
Appendix C. Effect of position uncertainty on the estimation of the Kármán constant for turbulent boundary layers	134
C.1. Continuous approach	134
C.2. Discrete approach	137
Acknowledgements	141
References	143

CHAPTER 1

Introduction

Amongst the different engineering fields, fluid mechanics is still one of the most fascinating and, at the same time, most challenging. The importance of this subject is reflected by the consideration that our life is always surrounded by fluids and, by just looking around, it is possible to see several phenomena where fluid mechanics is involved: the wind over trees, the wake behind a car or a boat, the motion of our blood and so on.

To describe the fluid motion it is possible to use the basic conservation laws (mass, momentum and energy conservation) considering the fluid as a continuum with infinite particles which interact each other in a certain way. The resulting equations are rather complex and difficult to solve analytically, except for few simple but very important cases (Batchelor 2002). For instance, the description of flow motion around airfoils follows directly from these equations together with some simplifying assumptions that Prandtl did at the beginning of the last century.

A phenomenon which increases the degree of complexity of the problem is the experimental observation that up to a certain flow speed the motion is steady and regular (*laminar* regime). Beyond this velocity the flow becomes gradually unsteady and irregular and it is named *turbulent*. The presence of this unsteadiness or fluctuations changes radically the flow behavior. As an example it is possible to observe figure 1.1 where a laminar and a turbulent pipe flow visualizations are reported. It is evident that the laminar region is smoother than the turbulent one which presents several vortices clearly detectable from the ink path. This phenomenon becomes more and more irregular and complex by increasing the flow velocity.

Reynolds (1883) was the first to characterize the turbulence phenomenon in pipes with different fluids and pipe diameter. He defined a characteristic number (called Reynolds number in his honor) by scaling the velocity with the pipe diameter D and the fluid kinematic viscosity ν (namely $Re = UD/\nu$). He noted that the transition from the laminar to the turbulent regime happened at a Reynolds number of about 13000. It is interesting to note that the laminar pipe flow (also called Hagen-Poiseuille flow) is theoretically stable to infinitesimal disturbances, as predicted by linear stability theory (more deeply discussed in chapter 2), for all Reynolds number and, indeed, the transition

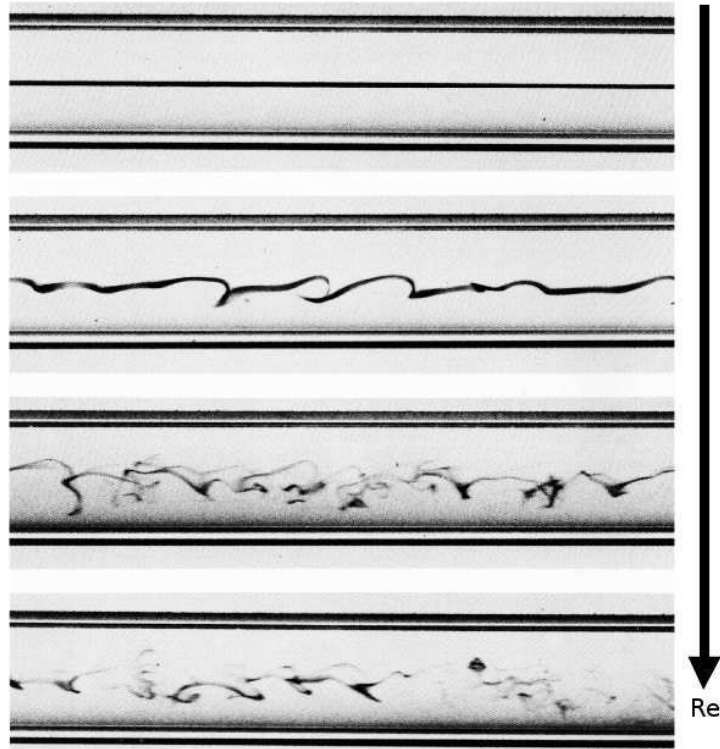


FIGURE 1.1. Comparison between laminar and turbulent flow in a pipe for different Reynolds numbers. Ink was injected upstream to follow a smokeline (Van Dyke 1982).

should not take place in pipes. Many theoreticians tried to explain this paradox but only recently this aspect has been clarified by introducing the by-pass transition concept and by considering the non-normality of the stability operator (Schmid & Henningson 2001). On the contrary, jets are very sensitive to external perturbations due to the inviscid instability of the velocity profile. The transition between the laminar to the turbulent state is a gradual process, which begins in the axisymmetric shear layer close to the inflectional points and then spreads towards the centerline.

To understand and predict the dynamical evolution of every flow there are three main approaches:

- **analytical.** The equations of motion are solved in an exact or approximate way obtaining a mathematical expression for the physical quantities we are looking for. This approach is usually the best since it gives complete information regarding the flow field, but is not always

feasible because only rarely the equations can be solved in closed form. Also, while there are many laminar flows where the solution of the equations is known, this is not the case of turbulent flows, where even very simple cases are not solved. For instance, there exists the analytical solution of the laminar jet (Schlichting 1968), but since the jet becomes turbulent at very low Reynolds numbers, it does not have any practical application;

- **numerical.** The equations of motion are solved by means of a computer simulation. It is not possible anymore to obtain a closed form description and so trends have to be evaluated with several simulations just by changing the operating parameters. Also, while in laminar flows the numerical solutions may be very accurate, in the turbulent regime a complete description of the flow is related to the description of the dynamics of all the turbulent scales (from the smallest to the biggest), forcing the discretization of the flow domain to become finer and finer, saturating consequently the actually available computational resources. This restricts the application of numerical solutions of the Navier-Stokes equations only to low Reynolds number flows which today are still far from most industrial cases. Other approaches avoid to simulate the smallest vortices (LES) or they try to simulate just the averaged field (RANS): these methods permit the simulation of high Reynolds number flows but they need some analytical expressions to take into account the interactions between the different vortices or between the turbulent and mean flow. These expressions are today still missing and only semi-empirical models are available which have been calibrated in simple flows and applied to more complex situations, with the hope that they will give a reasonable solution close to the real one.
- **experimental.** The flow is reproduced in laboratory and physical quantities are measured. Even with this approach it is possible to obtain discrete results (one for each experiment) which are affected by measurement errors and by a lack of knowledge of the exact boundary conditions. On the other hand, measurements of real flows do not need almost any modeling and the errors are anyway bounded by the measurement uncertainties.

Due to our lack of a full comprehension of turbulent flows, a lot of research efforts have been spent in simple basic flows (like jets, wakes and boundary layers) with the hope to enhance our understanding of turbulent mechanisms, especially regarding the flow dynamics and control.

From the industrial point of view, the comprehension of flow phenomena is of course fundamental since it is a first step towards the possibility to control their behavior. For instance, industrial burners are classical prototypes of this philosophy: many industries have been recently forced to sensibly reduce their

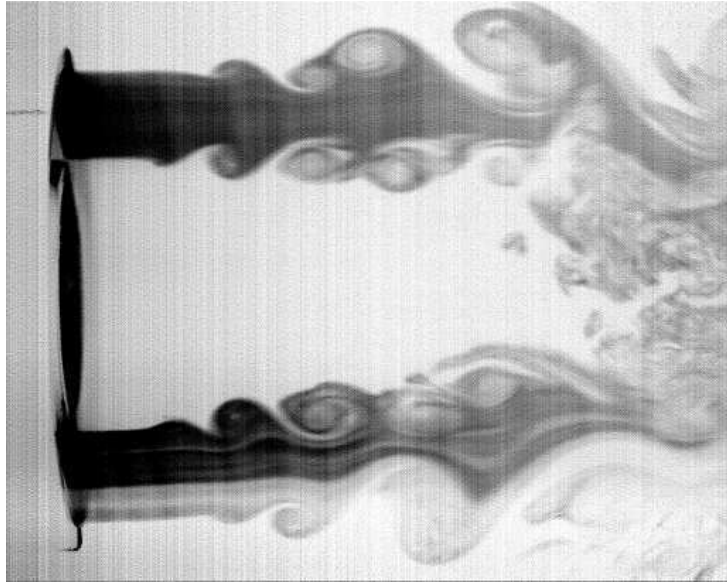


FIGURE 1.2. Flow visualization of two coaxial jets where the outer one has been seeded with smoke.



FIGURE 1.3. Flow visualization of an azimuthally excited jet where the stream has been seeded with smoke.

pollution from the combustion processes. To achieve this task and, simultaneously, to have an efficient industrial process, the combustion must happen near critical conditions where flame instability mechanisms could have place. Therefore, the fluid dynamic research in the mixing and combustion area has been greatly encouraged by many industries which are very interested to the practical implications of the outcomes.

Amongst the real industrial geometries, many combustion chambers are designed to maximize the mixing between fuel and oxidizer to increase the efficiency of the combustion process. Many real burners resemble single or coaxial jets where the streams are composed by different gases and combustion phenomena are present. The combustion of species is an exothermic phenomenon which usually has place at the interface between the gases. The dynamics of this interface is certainly affected by the combustion as well as by the transport mechanisms provided by the flow itself. By neglecting the presence of combustion, or restricting the study to a "cold" fluid mechanics, it is possible to highlight many aspects of the fluid transport effect, justifying our attempt to characterize these flows with an experimental setup where the streams are composed by just air.

Besides the characterization of the velocity field, the study of mixing between fluids is an important aspect when we consider industrial applications. Here and in the followings, we will use the term *mixing* to define the evolution process from the initial segregation of two or more species to the final homogeneous state. The mixing process can be described by the instantaneous concentration of the involved species which will be referred as *scalar* concentration $\theta(\mathbf{x}, t)$. When a scalar is able to influence the flow field it is named *active*, otherwise it is named *passive*. It is stressed again that the combustion process is related to active scalars, which affect the flow in sensible way, but many mixing mechanisms can be understood just by studying passive scalar dynamics which is easier to investigate in experiments and numerical simulations.

Until now we have discussed of the necessity to understand and solve the equations of motions, or to have enough experimental data to determine if a process is performed in the best way possible or not. On the other hand, a process can be forced to follow a certain direction by applying specific actions which are classified as *flow control*. This aspect has received recently a lot of attentions due to the improvements obtained in many situations. A first classification can be made by considering the energy requirement of the control to perform its action: if the control does not need energy from outside the flow system, it is named *passive* (i.e. a change in the boundary conditions or the use of an absolutely unstable region, for instance), otherwise *active* (i.e. the application of acoustic forcing or suction, for instance).¹

In the present thesis the effects of flow control in two basic flows will be investigated experimentally by means of passive and active methods to pursue the possibility of mixing enhancement or reduction as well as the effect of flow control on the flow field. The two investigated flows are the coaxial jets and the single jet. In the former case, the velocity and mixing will be characterized for two different nozzle geometries where one of them allows the presence of an

¹Other definitions of active/passive flow controls have been reviewed by Gad-el-Hak *et al.* (1998).

absolutely unstable region (Talamelli & Gavarini 2006) while, in the latter one, acoustic excitation will be applied to the lip to excite the flow and to trigger the formation of azimuthal modes and streamwise streaks like in boundary layers (Elofsson & Alfredsson 1998). The experimental approach has been preferred because such complex flow fields are still far from being numerically simulated at high Reynolds numbers due to the limited computational power. Two flow visualizations are reported in figures 1.2 and 1.3 as an example. To differentiate the streams, one has been seeded with smoke. This method provides some qualitative information concerning the mixing evolution in space as well as shape and dimensions of vortices.

The study of the velocity and mixing field in jets is important from both the research and the applicative point of view. Real industrial configurations are more complex than simple shear layers present in laboratory due to the presence of combustion, swirl and confinement for instance. Several experiments are still focused on simple shear flows since the turbulent dynamics of simple flows are present in more complex applications. Coaxial jets are by far more complex than simple shear layers due to the high number of parameters involved. They represent a further step towards the application of simple arguments in a real industrial flow because the flow field is a prototype of industrial burners but still simple enough to be characterized in a research laboratory. Many important researches have highlighted several key features of coaxial jets, but an extensive characterization in terms of velocity and mixing field is still missing and, therefore, motivates this thesis. Many aspects of the flow field will be discussed here, ranging from the velocity and mixing characterization for different operating conditions, to an investigation of the dominant instabilities present in this flow. On the other hand, simple jets have been studied by many authors, but there are some aspects related to the effect of acoustic excitation (i.e. active control) on the flow field still to be investigated and, therefore, an attempt has been done here by using different kinds of acoustic forcing.

This thesis shall continue with an essay of the fluid dynamics backgrounds related to the present research as well as a literature review on coaxial jets flow in chapter 2, while chapter 3 describes the coaxial jet facility and the experimental methods used in this work. In chapter 4 evidences of the vortex shedding effects will be proposed with some considerations on the coaxial jets flow while in chapter 5 the main instabilities observable in coaxial jets will be further discussed. Chapter 6 deals with the flow characterizations for different velocities and boundary conditions while chapter 7 treats the coaxial jets response to acoustic excitation for different velocity ratios. The conclusions of the coaxial jets experiments are reported in chapter 8 which concludes the part related to coaxial jets.

The main results from the experiments on azimuthal acoustic forcing of a single axisymmetric jet have been reported in the first appendix A which is stand-alone. This latter part is the result of an experimental campaign that

the author performed at the Royal Institute of Technology (KTH), together with Dr. R. Örlü and prof. P.H. Alfredsson, during 2008 on jet turbulence as well as on turbulent boundary layers for the KTH Jamboree. In the other two appendices several theoretical results will be presented: most of them are related to possible error sources in measurements of turbulent boundary layers, especially on the effects of spatial resolution of hot-wires and Kármán constant related issues which are still a big source of debates and uncertainties.

CHAPTER 2

Fluid dynamics background

When two fluids with different density, momentum or energy meet, the contact surface is discontinuous for some of these physical quantities. Nature imposes that real fluids cannot handle discontinuities inside the flow domain and, therefore, such discontinuities are eliminated by different processes which tend to smooth out the variations of all physical quantities across the surface. Real flows encountered in industrial practice are usually more complex than this simple case. However, it is also true that the most important phenomena take place in high gradients regions and indeed, despite the higher complexity of an industrial configuration, several complex flows can be characterized, at least at the beginning, as a superposition of different evolving surfaces where high physical gradients have place, generically called *shear layers*.

The most famous shear layers affected by momentum gradients are reported in figure 2.1 and are:

- *the boundary layer*: region of fluid around a moving wall which is influenced by the presence of the wall. In this region viscosity and turbulence effects play an important role altering significantly the local flow. Theoretically, all the fluid is affected by the presence of the wall, but only the boundary layer is subject to significant modifications;
- *the mixing layer*: flow generated by two fluids moving in the same direction but with different velocity values;
- *the jet*: flow generated by a fluid that exits through a nozzle in a quiescent environment;
- *the wake*: flow behind bodies which move inside a fluid at rest.

From the Navier-Stokes equations it is possible to deduce that the only mechanisms able to smooth out the gradients are convective and diffusive forces. The formers are due to the inertia of fluid particles and the latter to molecular transfer processes. It is clear that, when the flow velocity is low enough, the inertia of the particle is low and only the diffusive forces are able to smooth out gradients. The opposite process happens when the velocity is high enough. To quantify this “enough”, a dimensional analysis is performed on the basic equations and some dimensionless numbers are extracted. The most famous

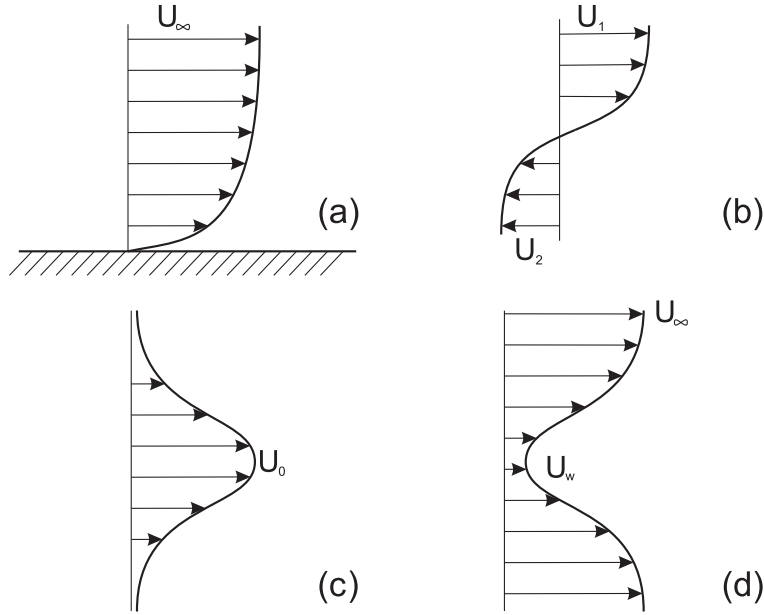


FIGURE 2.1. Sketch of the classical shear layers. (a) boundary layer (b) mixing layer (c) jet (d) wake.

dimensionless number is the *Reynolds number* defined as:

$$Re = \frac{UL}{\nu}$$

where U and L are a characteristic velocity and length scale of the flow while ν is the kinematic fluid viscosity. The Reynolds number is the ratio of convective forces over viscous forces and plays an important role in fluid mechanics. If Re is low enough there is the dominance of the viscous terms, while in the opposite case the convective terms prevail. In the former situation the flow is smooth and regular and it is referred as *laminar*. In the latter case (i.e high Reynolds number flows) the flow presents unsteadiness and complex interactions between whole fluid parcels and it is referred as *turbulent*. Since this thesis will focus mostly on the velocity field, it is important to point out now that in the following only velocity differences across shear layers will be considered.

The equation which governs the motion of an incompressible newtonian fluid and the dynamics of a passive scalar, which satisfies Fick's law of molecular diffusion, are (Kundu & Cohen 2002):

$$\begin{aligned}
& \nabla \cdot \mathbf{u} = 0 \\
& \frac{\partial \mathbf{u}}{\partial t} + \nabla \cdot (\mathbf{u}\mathbf{u}^t) = -\frac{1}{\rho} \nabla p + \frac{1}{Re} \nabla^2 \mathbf{u} \\
& \frac{\partial \theta}{\partial t} + \nabla \cdot (\theta \mathbf{u}) = \frac{1}{Pe} \nabla^2 \theta
\end{aligned} \tag{2.1}$$

where $\mathbf{u} = (u, v, w)$ is the velocity vector, p and ρ the mechanical pressure and the fluid density, respectively. The third equation is the scalar θ diffusion equation which is affected by the diffusive term, modulated by the Peclet number $Pe = UL/\alpha$ (where α is the scalar diffusivity), analogous of the Reynolds number for the momentum diffusion.

Laminar solutions of the Navier-Stokes equations are possible analytically and numerically. The stability analysis of these solutions is then investigated to assess their behavior when small perturbations are present. If these perturbations will decay, the flow is said to be *stable*, otherwise *unstable*¹. Most laminar solutions are stable if the Reynolds number is low enough (Schlichting 1968). For all real flows, however, there exists a critical Reynolds number above which a transition towards a different state begins. The value of this threshold is flow-dependent but it is usually smaller than the Reynolds number of most industrial flows, which means that the study of turbulent flows in real applications is important and inevitable. The transition towards turbulence is not always a "bad thing" because, depending on the particular application, the turbulent state has several advantages and disadvantages related to the relative increase of mixing capacity and frictional drag.

Despite the amount of researches involved in the study of simple turbulent shear layers, a complete description of the flow field from a certain initial condition is still missing. The non-linearity of the Navier-Stokes equations in their convective term causes the chaotic behavior observed in many flows, which results in an extreme sensibility to the initial and boundary conditions that affects the flow behavior (Ottino 1990; Broze & Hussain 1996; Fountain *et al.* 2000). As pointed out by Drazin (1992) even an infinitesimal variation of the initial conditions of a non-linear system can affect sensibly the whole dynamics after enough time. This means that, even with a perfect experiments where all the boundary conditions are known up to a finite accuracy level, soon or later it will be impossible to know the exact velocity at a certain point in the time-space frame.

Even if the full characterization of a turbulent flow is still an impossible task, several approaches have been able to highlight many important aspects of the investigated flows. The statistical approach has been historically the

¹Non-normality of the stability operator will not be considered here (Schmid & Henningson 2001).

first since Reynolds (1883) described the turbulence as a superposition of random processes that can be characterized statistically. The flow field is indeed decomposed in a mean part and a fluctuating part through the definition of a proper average operator $\langle \cdot \rangle$. In this way the velocity field is decomposed in an averaged part and a fluctuating one as:

$$\mathbf{u} = \langle \mathbf{u} \rangle (\mathbf{x}, t) + \mathbf{u}' (\mathbf{x}, t) \quad (2.2)$$

where $\langle \mathbf{u}' \rangle (\mathbf{x}, t) = 0 \forall (\mathbf{x}, t)$.

While this approach has been widely used in practice, due to its simplicity and usefulness in estimating practical average quantities (like the mean skin friction of the flow over a wall or the mean heat transfer coefficient, for instance), the drawback is that the theoretical behavior of averaged quantities is governed by the Reynolds Averaged Navier-Stokes equations (RANS) which are:

$$\begin{aligned} \nabla \cdot \langle \mathbf{u} \rangle &= 0 \\ \frac{\partial \langle \mathbf{u} \rangle}{\partial t} + \nabla \cdot (\langle \mathbf{u} \rangle \langle \mathbf{u}^t \rangle + \langle \mathbf{u}' \mathbf{u}'^t \rangle) &= -\frac{1}{\rho} \nabla \langle p \rangle + \frac{1}{Re} \nabla^2 \langle \mathbf{u} \rangle \\ \frac{\partial \langle \theta \rangle}{\partial t} + \nabla \cdot (\langle \theta \rangle \langle \mathbf{u} \rangle + \langle \theta' \mathbf{u}' \rangle) &= \frac{1}{Pe} \nabla^2 \langle \theta \rangle \end{aligned} \quad (2.3)$$

which are unclosed due to the presence of the extra-terms called Reynolds stresses $\langle \mathbf{u}' \mathbf{u}'^t \rangle$ and scalar fluxes $\langle \theta' \mathbf{u}' \rangle$. Many models have been developed to estimate these terms from the mean quantities but, even if there have been good results for some flows, a general turbulence model able to predict accurately the average quantities of a turbulent flow is still missing.

The second approach has been developed in the last 40 years after the identification of ordered structures embedded in turbulent flows (Crow & Champagne 1971). This idea changed completely the way turbulent flows were considered: after the introduction of the coherent structure concept, turbulence was viewed as a superposition of vortices of different scales, each one following its proper dynamics. The identification of such structures is still a matter of debate since there is no agreement on the definition of such structures and even less agreement in the optimal way to identify them (Jeong & Hussain 1995). Despite the lack of solid mathematical foundations of the coherent structures concept, great advances have been obtained by means of the application of these ideas to many flows (Zaman & Hussain 1984; Zhou *et al.* 1999, for instance).

The introduction of acoustic excitation in turbulent flows has enhanced our comprehension about vortex structures embedded in the flow field due to the presence of a periodic event which forces the flow to follow such periodicity. It is still unclear whether or not the structures that are educed with the acoustic excitation, are still observable without. However, as underlined by

Hussain (1986), the acoustic forcing is just a deterministic perturbation imposed to the flow which does not change the flow internal dynamics, provided that the forcing amplitude is not strong enough to affect significantly the flow. The introduction of this coherent excitation reduced the jitter phenomenon of vortex formation and made the measurements less affected by the randomness of turbulence. The introduction of conditionally sampled techniques as well as numerical simulations (DNS) and new optical measurement techniques (PIV), gave also the opportunity to characterize the vortex structures and to follow their dynamics in a whole field.

To enhance our comprehension regarding the birth of such structures, many theoretical approaches have been developed (Schoppa & Hussain 2002; Nickels & Marusic 2001, for instance) but most of them rely on the stability analysis of the base flow where some infinitesimal waves are superposed. This approach permits a simple analytical tractation together with a clear description of the instability evolution in its first stages. The study of simple shear flows highlighted several properties of turbulent flows and of vortex dynamics connected to the instability properties of the flow itself. In the following paragraphs, few instability ideas will be recalled together with the most important experimental results regarding vortex formation and dynamics in shear layers.

2.1. Instability backgrounds

Hydrodynamic stability theory is concerned with the response of a laminar flow to a disturbance of small or moderate amplitude. If the flow returns to its original laminar state one defines the flow as *stable*, whereas if the disturbance grows and causes the laminar flow to change into a different state, one defines the flow as *unstable*. The stability analysis of a certain flow is usually performed by linearizing the Navier-Stokes equations around a certain base flow where a small perturbation is included. In the particular case of steady parallel base flows, this perturbation is supposed to be homogeneous in time and space and, indeed, it is described as a sine wave $u'(x, y, t) = \hat{u}(y)e^{i(\alpha x - \omega t)}$, where $\hat{u}(y)$ is the y -dependent amplitude and α and ω are the complex wavenumber and frequency, respectively. If the wave is unstable, its growth rate σ is positive and negative otherwise. The interested reader is forwarded to stability textbooks as the one by Schmid & Henningson (2001) and Drazin (2002).

Linear stability theory has been extremely successful in predicting many essential features of the initial development of a variety of flow instabilities. In any such comparison one has to choose between temporal theory and spatial theory. In temporal stability calculations it is implicitly assumed that disturbances evolve in time from some initial spatial distribution. The wavenumber α is taken to be real and the goal of linear theory is then to determine the complex frequency ω as a function of α . However, in the experimental study of parallel-flow instabilities, such as free shear flows and boundary layers, the instability process is very often controlled by periodically forcing the flow at a

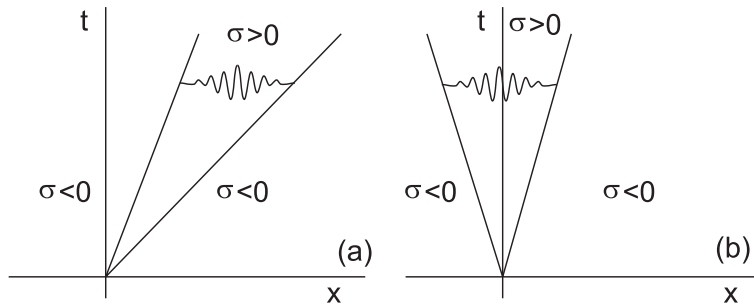


FIGURE 2.2. Sketch of different instability characters in the $x - t$ diagram. (a) convective instability (b) absolute instability.

given frequency. This introduces the spatial approach where the real frequency ω is taken to be real and the goal of linear theory is then to determine the complex wavenumber α as a function of ω . The experience has shown that the spatial approach results are closer to experiments than the temporal ones.

2.1.1. Convective versus absolute instability

To assess the instability character of a certain flow, it is important to investigate the impulse response of the flow itself at various streamwise locations. If the localized disturbance generated by the impulse spreads both upstream and downstream of the location where it was originated, the flow is considered *absolutely unstable*. In case the disturbance is swept downstream or upstream of the source, the flow is *convectively unstable*. Figure 2.2 demonstrates the concept of absolute and convective instability with a $x - t$ diagram.

The mathematical details regarding this stability problem were treated by Huerre & Monkewitz (1985) and Schmid & Henningson (2001) and are based on the branch-points singularities of the dispersion relation for complex frequencies and wavenumbers. The dispersion relation $D(\alpha, \omega, \mu_0) = 0$ associates dynamic behavior in space and time for a certain value of the parameter μ_0 and is obtained by solving the stability equations (usually the Rayleigh or the Orr-Sommerfeld equation).

The concept of convective and absolute instability as discussed above applies only to parallel flows. However in many situations shear flows are not parallel but rather evolve in the streamwise direction. In this case the hypothesis of x as homogeneous direction no longer applies and the global approach must be pursued where the x dependence is unknown, rather than sinusoidal. As underlined by Chomaz (2005), the presence of local absolute instability is the necessary condition for the existence of a global instability mode, which implies that the fluid behaves as a nonlinear oscillator with no sensitivity to

external disturbances. Chomaz, Huerre & Redekopp (1988) pointed out that the presence of an absolute instability becomes a sufficient condition for the existence of a global mode if the absolutely unstable region has enough spatial extension.

Open shear flows may then be classified according to the nature of instability they can support. The response of convectively unstable flows, like mixing-layers, is determined by the spatial evolution of instability waves resulting from the amplification of an external input, as would be the case of a noise amplifier. In the case of an absolute unstable flow, like a bluff-body wake, the response could be affected by a global mode, exciting the flow at a specific frequency as an hydrodynamic oscillator.

For many nonparallel flows (such as spatially developing mixing layers, flat-plate boundary layers, and homogeneous jets) the mean flow is locally convectively unstable everywhere with respect to vortical fluctuations (see figure 2.3(a)). In such systems, any disturbance is advected by the flow as it is amplified. The medium is extremely sensitive to external coherent forcing. Measured frequency spectra are generally broadband. Self-sustained oscillations do not seem to be possible except for some induced by pressure waves feedback from the far field. In contrast, strong self-sustained oscillations can be obtained when one introduces a second streamlined or blunt body at a finite distance downstream (see figure 2.3(b)). The flow is still locally convectively unstable from the point of view of vorticity fluctuations but the dynamics of the flow are dominated by a feedback loop (Hussain & Zaman 1978). Theoretical and experimental evidences show that in the wake behind a body, self-sustained oscillations can also be produced by purely hydrodynamic means, without the need of any second body downstream (see figure 2.3(c)). In this class, the nature of the instability changes from locally absolute to locally convective and discrete tones appear in the frequency spectra.

2.2. Classical shear layers

Simple shear layers are an important benchmark to learn basic aspects of turbulent flows as well as a way to test easily our knowledge and models regarding several turbulence features, with the hope that similar concepts apply to more complex cases. A short survey of classical open shear layers will be presented hereby with a particular focus on previous results on vortex formation and dynamics.

2.2.1. *Mixing layers*

A mixing layer is the flow that forms between two uniform, nearly parallel streams of different velocities U_1 and U_2 (in the followings will be assumed $U_2 > U_1$ without any loss of generality). Here the dominant direction is x , while y and z denote the cross stream and spanwise directions. Two velocity

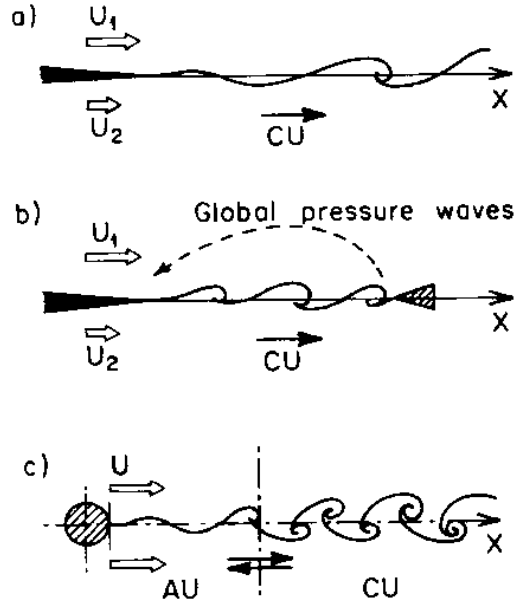


FIGURE 2.3. Classes of spatially developing flows. (a) no resonances; (b) hydroacoustic resonances; (c) hydrodynamic resonances (Chomaz *et al.* 1988).

scales can be defined, i.e. the characteristic convection velocity

$$U_c = \frac{U_1 + U_2}{2}$$

and the characteristic velocity difference

$$U_s = U_2 - U_1$$

The inflection point in the velocity profiles fulfills the Rayleigh criterion (Schmid & Henningson 2001) and indeed the flow could be inviscidly unstable. Since the critical Reynolds number of mixing layer is very low, the flow is unstable for all practical operating conditions.

As stated above, the initial discontinuity in velocity profile between the two initially segregated fluids cannot be sustained by the flow. Batchelor (2002) reported that a sinusoidal perturbation on a vortex sheet will necessarily lead to the formation of concentrated vortices (Kelvin-Helmholtz instability mechanism). Michalke (1965) characterized the spatial stability of an hyperbolic tangent profile, which allows a finite thickness of the layer and, indeed, closer to real ones where the splitter plate boundary layers smooth out the initial velocity profile. He found that this flow was unstable and reported that, for

an axisymmetric mixing layer, the maximum growth was observed at a dimensionless frequency f_{kh} of:

$$St_\theta = \frac{f_{kh}\theta}{U_s} = 0.017 \quad (2.4)$$

where θ is the momentum thickness of the boundary layer at the exit and St_θ is the Strouhal number based on θ . Once the perturbation starts to grow, the flow becomes more and more different: the perturbation is no more small and, at a certain point, it starts to interact non-linearly with the mean flow until the saturation. When this happens, there is the so called “roll-off” and strong vorticity concentrations will appear (Corcos & Sherman 1978).

Brown & Roshko (1974) did several flow visualizations by means of shadowgraph technique with two streams with different densities, observing the formation of clear structures (figure 2.4) which evolve by going downstream. In the laminar instability layer the spacing of the vortices was equal to the wavelength of the initial small disturbance from which they had developed. By going downstream this distance increased as x as well as the vortices diameter with a constant convective speed near U_c . On a dimensional basis, the requirements of constant convection velocity and increasing vortex size, imply a decreasing passage frequency, which means that some vortices must slow down with x . This paradox was solved by following single vortices and noting that, at certain random streamwise locations, two or even three vortices merged generating one bigger structure. This phenomenon of successive mergings of vortices is called *pairing* and governs the initial streamwise growth of mixing layers (Winant & Browand 1974). Thus, the vorticity initially contained in the basic velocity profile is being constantly redistributed into larger and larger vortices, their wavelength and strength being doubled after each interaction (Ho & Huerre 1984). It is still unclear whether or not these vortex interactions govern the large part of the entrainment rate of surrounding fluid. As pointed out by Hernan & Jimenez (1982) most of the entrainment takes place during the growth stage of the large eddies and not during pairing but more experimental evidences are needed to support these statements.

2.2.2. Jets

A jet is a fluid that steadily flows through a nozzle of diameter D , which produces (approximately) a flat-topped velocity profile with velocity U_o . The jet from the nozzle flows into an ambient of the same fluid, which is at rest at infinity. After the nozzle, the flow starts to interact with the surrounding fluid generating an axisymmetric shear layer which delimits the jet potential core where the velocity keeps the exit value with low fluctuations, as clearly shown in the flow visualization of figure 2.5. The potential core ends five diameters downstream the exit and thereafter the axisymmetric shear layer starts to merge. After thirty diameters, the flow reaches a balance between

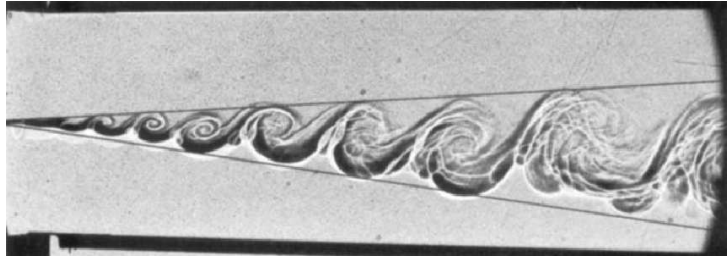


FIGURE 2.4. Shadowgraph of a mixing layer. Lines show an estimation of the thickness of the layer *versus* streamwise distance (Brown & Roshko 1974).



FIGURE 2.5. Flow visualization of the near field of a turbulent air jet at $Re = 8500$ (courtesy of Dr. R. Örlü).

turbulent convection and diffusion. In this latter region it is believed that the flow has lost its memory of the initial conditions and, indeed, a self-similar flow is expected, namely all the flow quantities should scale with a single length and velocity scale. The proper characteristic scales are the local centerline velocity and the jet width and many experiments confirm this property (Abramovich 1963). Even if the thin shear layer theory predicts this behavior, there are theoretical (George 1989) and experimental evidences (Hussain & Zedan 1978) that footprints of the initial conditions are still present in the self-similar region, usually called *far field*.

Batchelor & Gill (1962) were the first to investigate the instability of the top-hat velocity profile of a jet issuing from a nozzle modeling it as a cylindrical vortex sheet in an inviscid fluid. The authors demonstrated that the discontinuity of the velocity profile implies that this kind of flow is unstable to all the spatial disturbances (both axial and azimuthal perturbations). Lately, Becker & Massaro (1968) pointed out that the most amplified disturbance in

the jet shear layer had a wavelength determined by the effluent boundary layer thickness, which agrees with the theoretical predictions of Michalke (1965).

By means of acoustic excitation, two modes in jet turbulence have been highlighted. The first one, called “jet-column mode”, was discovered by Crow & Champagne (1971) and is related to the instability of the whole jet column downstream the nozzle. By exciting the jet at a Strouhal number

$$St_D = \frac{fD}{U_o} = 0.3$$

the centerline velocity rms showed a peak nearly 4 diameters downstream the exit, namely close to the end of the potential core.

Another important result regarding the highlighted by the acoustic excitation of the jet was obtained by Zaman & Hussain (1980), who proposed a scaling relationship to determine the preferred Strouhal number in the near field shear layer of a jet (the so-called “shear layer mode”):

$$St_\theta = \frac{f\theta}{U_o} = 0.012 \quad (2.5)$$

which is different from the one with maximum growth rate observed in plane mixing layers (Michalke 1965) and axisymmetric shear layers (Cohen & Wygnanski 1987*a*). Zaman & Hussain (1980) observed that the $St_\theta = 0.012$ corresponds to the natural roll-up frequency of the Kelvin-Helmholtz vortices, while $St_\theta = 0.017$ corresponds to the most amplified disturbance. This is still a controversial matter of debate because many experiments found roll-up Strouhal numbers between these two values. Even if there are many experimental and numerical results, the extreme sensibility of the jet to the initial and boundary conditions (Hussain & Zedan 1978) make the full characterization a non trivial task which can be pursued only with special facilities and special measurement equipments (Panchapakesan & Lumley 1993).

Downstream the first roll-up location, several subsequent pairing events take place until the shear layer thickness become of the same order of the jet diameter. Drubka, Reisenthel & Nagib (1989) suggested that, by going downstream, three or four stages of pairing have place until the end of the potential core and, indeed, these vortices interact giving birth to the jet column mode. This conjecture has still to be confirmed by more experimental data.

The stability analysis of Batchelor & Gill (1962) underlined also that the axisymmetric vortex sheet, which is a first model of the near field shear layer, is unstable to all disturbances, whether they axisymmetric or not. In particular, they stated that the linear stability of the velocity profile in the far field is affected only by the azimuthal mode $m = 1$ (i.e. helical vortices), while axisymmetric perturbations are stable. This latter aspect has been discussed by many authors with theoretical calculations (Strange & Crighton 1983) and complex experiments (Jung, Gamard & George 2004; Gamard, Jung & George

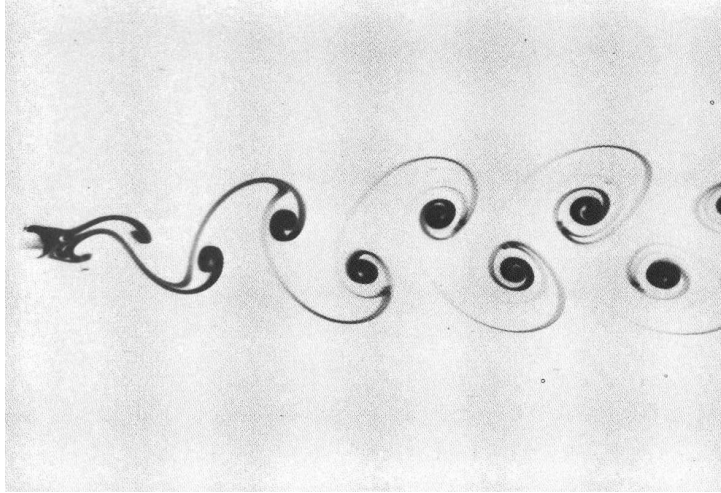


FIGURE 2.6. Von Kármán street behind a cylinder at $Re = 105$ (Van Dyke 1982).

2004; Iqbal & Thomas 2007) but today there are still many uncertainties related to this aspect. However, it seems to be clear today is that the dominant mode in the near field is strongly related to the initial and boundary conditions of the flow and, therefore, much more experimental data are needed to fully understand this complex dynamic.

2.2.3. *Wakes*

A wake is formed when an uniform stream flows over a body of arbitrary shape. This flow is particularly important from the applicative point of view because the velocity deficit in the wake is related to the drag experienced by the body (Anderson 1984). The length and velocity characteristic scales are respectively the wake width L and the maximum velocity deficit $\Delta U = U_\infty - U_w$ which are, like in all the previously cited shear layers, local quantities.

An important feature of this flow is that, above a critical Reynolds number vortices are created at the back of the body and detach periodically from either side of the body itself. Van Dyke (1982) showed in his book many pictures like figure 2.6 of shedding behind cylinders where the regularity of this flow can be further appreciated for different bodies. This unsteady flow is strongly periodic with a typical frequency f_{vs} which scales with the freestream velocity and the wake width as:

$$St_D = \frac{f_{vs} D}{U_\infty}$$

where $St_D \approx 0.2$ as a rule-of-thumb.

The instability behind the body is absolute for a certain length and a global oscillating mode appears. Therefore, the flow starts to oscillate at a precise frequency f_{vs} . At a certain x station, the instability is no more absolute and thereby the vortices are convected downstream by means of the mean flow until the vorticity transport and diffusion processes will annihilate them. The frequency f_{vs} is, as all the stability related quantities, function of the local mean velocity profile, which is a function of the Reynolds number which affects both the separating boundary layer thickness and the wake thickness (through the separation points position). The Strouhal number St_D is indeed a function of the Reynolds number as well as of the body geometry and of thermal conditions, as reviewed in the paper of Wang, Trávníček & Chia (2000) where many $St_D(Re)$ relationships were proposed.

2.2.4. Wake-Mixing layer interaction

It is useful to discuss now about the effect of the wake component on the evolution of a plane mixing layer. Boldman, Brinich & Goldstein (1976), by means of flow visualizations and of a numerical model, investigated the vortex shedding from a blunt trailing edge with unequal external velocities. The authors underlined that a complex transition between wake and mixing-layer behavior was observed when the velocity ratio of the two streams U_2/U_1 was increased. For equal velocities, a Von Kármán street appeared, with two rows of symmetric vortices in a staggered arrangement in the neighborhood of the inflectional points of the velocity profile. By increasing the velocity ratio, the vortices became progressively asymmetrical with bigger vortices on the high speed side which, for high enough U_2/U_1 , had the tendency to inglobate the smaller ones and, therefore, to recover the mixing layer vortex pattern.

Wallace & Redekopp (1992) studied the stability character of a family of wake-mixing layer profiles and found that the convective *versus* absolute instability character was strongly dependent on the velocity ratio of the two streams as well as on the velocity deficit of the base flow. Since this velocity deficit is reduced by going downstream due to the transport mechanisms, the spatial stability character changes being the flow absolutely unstable at the beginning and becoming convectively unstable afterward, as in classical wake flows. The effect of the wake of the splitter plate has been discussed also by Dziomba & Fiedler (1985) and Mehta (1991*a*) where they pointed out that the presence of the wake affects also the self-similar region of mixing layer which is generally quite far from the lip. Recently Laizet, Lardeau & Lamballais (2010) have performed some DNS for this flow using different types of separating wall, discovering that the vortex pattern behind the separating wall can be affected dramatically by the wall geometry.

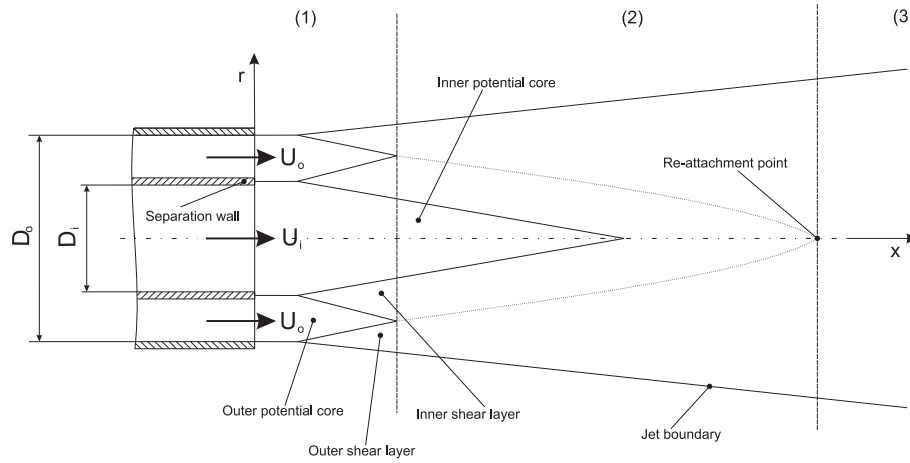


FIGURE 2.7. Sketch of the coaxial jets flow field.

2.3. Coaxial jets

Simple shear flows have been of great help to enhance our understanding of the transition process towards turbulence as well as to investigate the behavior of turbulence itself. However, most of the industrial geometries are more complex than the cited simple shear layers: they certainly have some region where the flow is driven by some of the classical instability mechanisms which drive the flow towards a certain state. The necessity to investigate more complex flows brought attentions towards other shear layers more similar to industrial flows. The coaxial jets flow is an important example of this approach because they are prototypes of industrial burners and of aircraft engines but, on the other hand, they are simple enough to be characterized in laboratory.

In the coaxial jets geometry, the presence of two shear layers that interact with each other is the breakthrough parameter that affects the fluid dynamic characterization in the near field region that, otherwise, could be described like the one of a simple axisymmetric jet. Several authors have studied the velocity and the passive scalar field of a coaxial jet geometry like Dahm, Frieler & Tryggvason (1992), Buresti, Talamelli & Petagna (1994), Villermaux & Rehab (2000), da Silva, Balarac & Métais (2003), Talamelli & Gavarini (2006) and among others, and all point out that this interaction makes this flow interesting from the research as well as from the industrial point of view.

In figure 2.7 a schematic representation of the flow field of a coaxial jets configuration is reported with the same subdivision made by Ko & Kwan (1976). The region (1) is called *initial merging zone* and is characterized by the segregation of the two shear layers by means of the inner and the outer potential cores. Downstream region (1), the two shear layers begin to merge and they

develop in region (2), also called *intermediate region*. Further downstream, the *fully merged zone* is approached (region (3)) in which the jets develop like an equivalent single one in the self-similar region. Despite the simplicity of the flow field, the parameters able to affect the flow are numerous. Amongst the most important there are:

- the diameter ratio $\beta = D_o/D_i$;
- the velocity ratio $r_u = U_o/U_i$;
- the inner velocity U_i ;
- the inner diameter D_i ;
- the shape of the separating wall and its thickness t at the trailing edge;
- the state of the boundary layers and their thicknesses;
- the freestream conditions.

One of the first models of coaxial jets was due to the investigations of Ko & Kwan (1976) which observed that, for low velocity ratios (namely $r_u < 0.7$), the coaxial jets can be described as a combination of single jets where the two shear layers generate their own proper instability almost independently. Dahm *et al.* (1992) performed many flow visualizations for different velocity ratios ($0.6 < r_u < 4.2$) observing a clear coupling between the two shear layers and, in particular, they reported a dominance of the outer shear layer which dictates the vortex formation in the inner shear layer (hereby the inner and outer shear layers will be called ISL and OSL, respectively). The latter observations have been also reported by other experiments (Rehab *et al.* 1997; Angele *et al.* 2006) and numerical simulations (da Silva *et al.* 2003) where all observed that, in the near field, the spectral peaks present in both shear layers are equal to the most unstable frequency of the OSL.

From these observations, the dominating parameters appear to be the outer jet velocity as well as the characteristics of the outermost boundary layer BL3 (the notation of the boundary layers will be presented in detail in chapter 3), for high velocity ratios, and parameters of both jets for low velocity ratios. However, Dahm *et al.* (1992) pointed out that the wake of the separation wall between the two streams had also an effect as well as the magnitude of both jet velocities. During the experimental campaign on aircraft engine noise of Olsen & Karchmer (1976), the authors recognized that, when the velocities of both streams were equal, a loud acoustic tone was perceived. They concluded by considering that tone as trailing edge noise due to flow separation at the wall between the two streams. The same year, by means of a 2D experiment on a mixing layer with a thick splitter plate, Boldman, Brinich & Goldstein (1976) showed that the observed tone was related to the trailing edge but, more specifically, was due to vortex shedding behind the separating wall present only when the inner and outer velocities were close to each other. By means of a simplified numerical model, they also showed that, when the velocity ratio is nearly unitary, there are two rows of staggered vortices with the same strength but,

when r_u departs from unity, the two rows become asymmetrical with stronger vortices on the high speed side. For very low velocity ratios the big vortices had the tendency to inglobate the smaller ones, and the Kelvin-Helmholtz vortex pattern is recovered. The theoretical study of Koch (1985) on 2D wakes with unequal velocities confirmed this trend and underlined that, for their base flow, the flow is absolutely unstable if the velocity ratio exceeds 0.5. Even if it was clear at that point that the flow behavior was altered by the wake of the separating wall, the first to characterize this effect were Buresti *et al.* (1994). The authors studied experimentally the velocity spectra in the inner shear layer of two coaxial jets evincing a relationship between the vortex shedding frequency f_{vs} and the average velocity of the two streams $U_m = (U_i + U_o)/2$ of the form

$$St_t = \frac{f_{vs} t}{U_m}$$

the defined Strouhal number was close to 0.24 up to a velocity ratio of $r_u \approx 2.27$ after which it started to increase. The high regularity of the shedding phenomenon, for some given operating conditions, was also investigated by Örlü *et al.* (2008a), where the authors used two wall geometries with different thickness to characterize the flow field with and without a noticeable wake width behind the separating wall. When the thick wall was mounted the magnitude of the dominant frequency increased with the average velocity of the jets, which was not the case when the sharp wall geometry was mounted. As stated in Talamelli & Gavarini (2006) and underlined in Örlü *et al.* (2008a), only a wall thick enough can create the conditions for a significant wake instability. A threshold thickness value to the onset of the wake instability could be expressed by using the results of Dziomba & Fiedler (1985) where the authors, studying the effect of initial conditions on mixing layers, found that for a separating wall thickness of less than 50% of the sum of the displacement thickness of both boundary layers there was no noticeable effect in the self-similar region.

The linear stability analysis of Talamelli & Gavarini (2006) on some coaxial jets base flows confirmed the presence of an absolute unstable mode inside a range of velocity ratios and shear layers momentum thickness. The dimensionless absolute frequency became constant if scaled with the average velocity of the two streams and the thickness of the wake. Even if the above mentioned study was made under the inviscid parallel flow assumption, viscous effects re-enter in the problem through the boundary layers thicknesses which affect the wake width. From these considerations and the application of Buckingham theorem (discussed in chapter 5), it turns out that the simple thickness of the splitter plate is a good scaling provided that the thickness of the side boundary layers are small compared to t , like in the facility of Buresti *et al.* (1994). Therefore, they have to be characterized and to be included somehow in the scaling if more accuracy is requested. A more critical assessment of this issue will be further discussed in chapter 5 where the interested reader is forwarded.

To conclude this section, different flow visualizations are reported on figures 2.8-2.10 to summarize the different flow aspects above discussed. Eight successive frames of a flow visualization movie are reported for three different velocity ratios, and with the two wall geometries, in order to appreciate the dynamics involved.

Figure 2.8 reports the flow visualization with $r_u = 0.2$, with the thick separating wall, where it is possible to see the faster evolution of the ISL vortices whereas the OSL shows only one big vortex after which the outer potential core ends and the two shear layers start to interact. The inner vortices are smaller and faster than the outer ones, as could be expected from the analysis of simple mixing layers. In this case no noticeable interaction seems to have place.

Figure 2.9 reports the flow visualization for unitary velocity ratio where the wake has its maximum effect. The ISL does not present anymore the Kelvin-Helmholtz vortices of the previous case, which are replaced by something closer to a Kármán vortex street. The OSL on the other hand, develops its own vortices with the same passage frequency of the inner layer vortices as underlined by Örlü *et al.* (2008a). The effect of the separating wall change is reported in figure 2.10 where a sharp wall has been used. The inner vortex street is completely absent in the near field, while some kind of vortex organization is observed one inner diameter downstream the jets exit with a low mixing rate. If we assume that the length of the region of absolutely unstable flow scales with the thickness of the wall, it can be conjectured that this vortex organization is driven by external perturbations amplified by the instability of the mean flow and, therefore, far from the instability character that the flow with the thick separating wall presented.

By increasing the velocity ratio up to $r_u = 1.5$ the flow pattern changes again (figures 2.11-2.12). A stronger vortex organization is still observable with the thick wall but without any resemblance with the staggered vortex pattern of the unitary velocity ratio case. Due to a higher perturbation level introduced by the wake, both shear layers appear to be more fluctuating, with bigger vortices slightly irregular.

On the other hand, figure 2.13 shows another completely different flow pattern dominated by the outer shear layer which imposes its own dynamics. After the first roll-up the ISL and OSL vortices appear radially aligned and no azimuthal change is observed. The inner potential core is shorter than before and big interacting vortices are observed in the outer layer. This picture agrees with the findings of Dahm *et al.* (1992) and da Silva *et al.* (2003) and underlines the concept of “lock-in phenomenon” expressed before.

2.3.1. Flow control in coaxial jets

As stated in the introduction, flow processes can be studied and optimized by solving the conservation equations. Sometimes specific actions can improve the

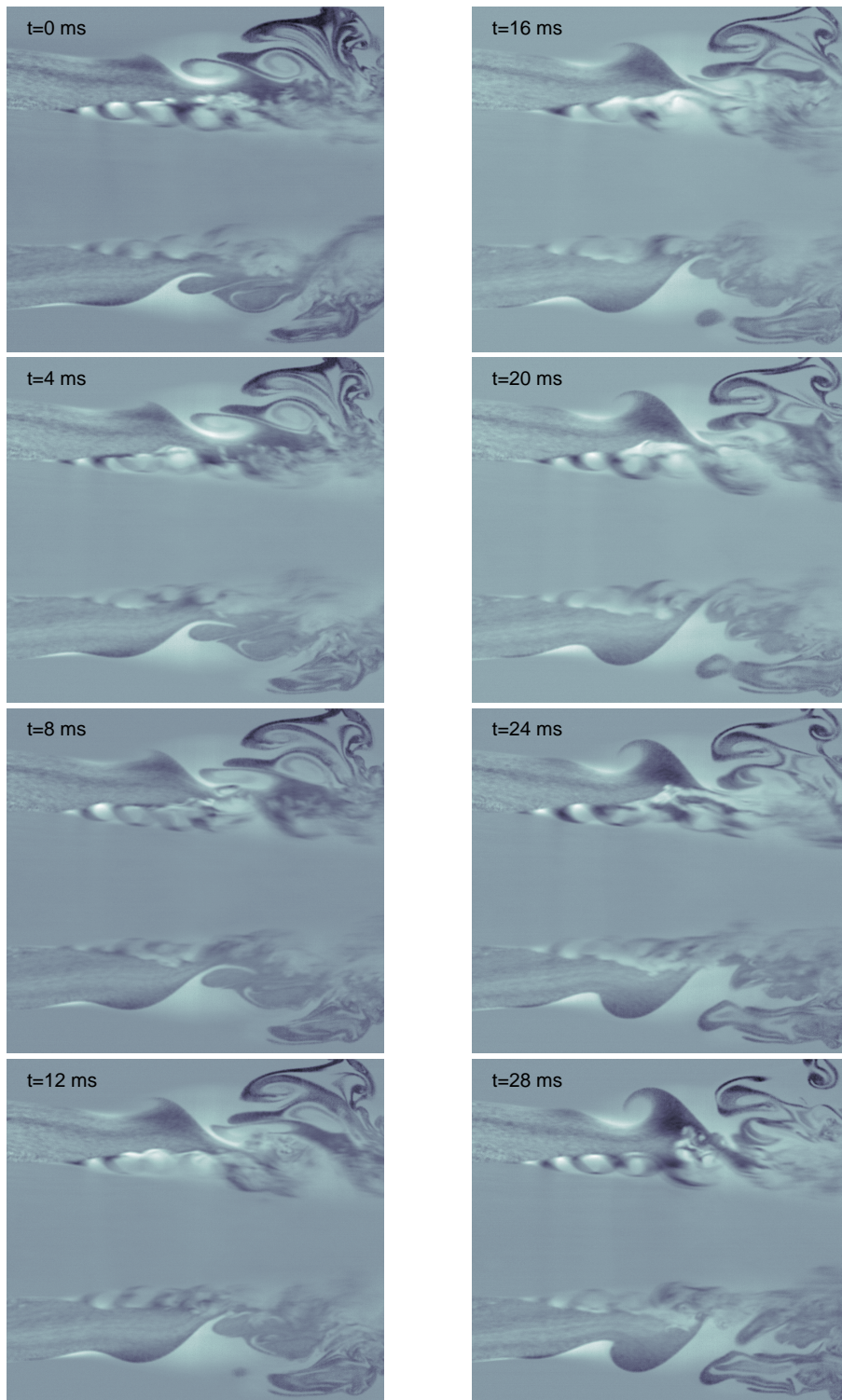


FIGURE 2.8. Instantaneous flow visualizations for $r_u = 0.2$ with the thick wall.

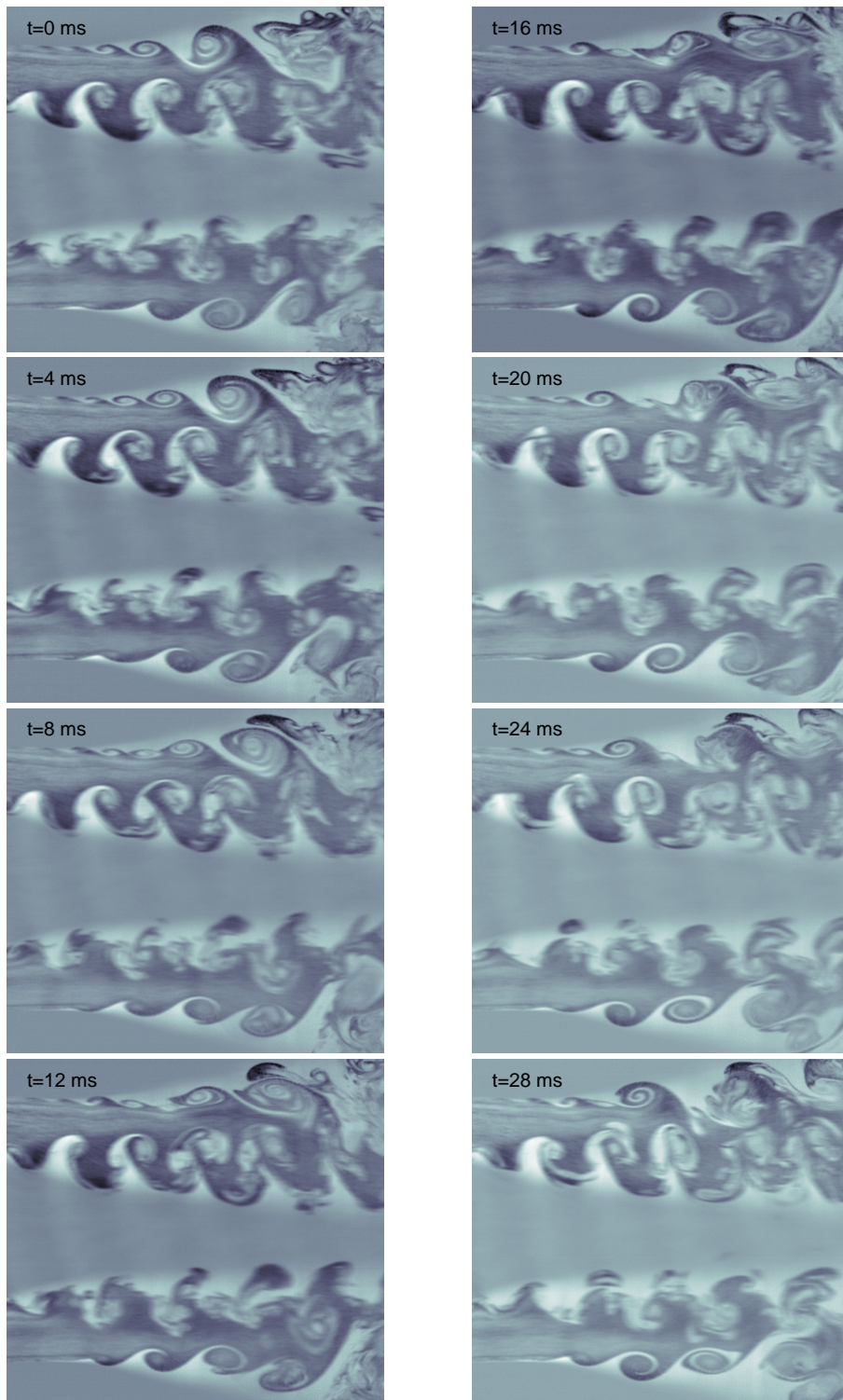


FIGURE 2.9. Instantaneous flow visualizations for $r_u = 1$ with the thick wall.

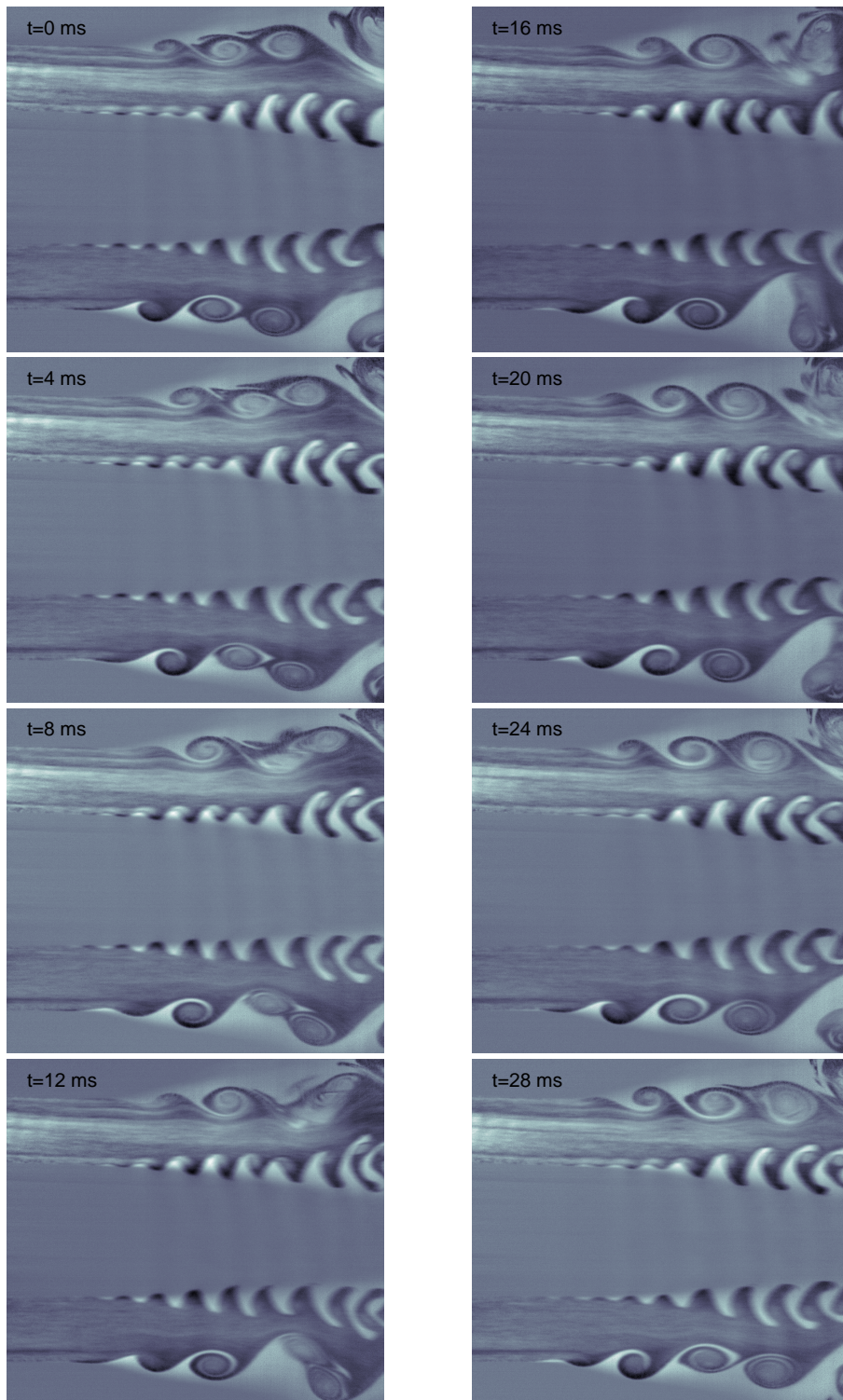


FIGURE 2.10. Instantaneous flow visualizations for $r_u = 1$ with the sharp wall.

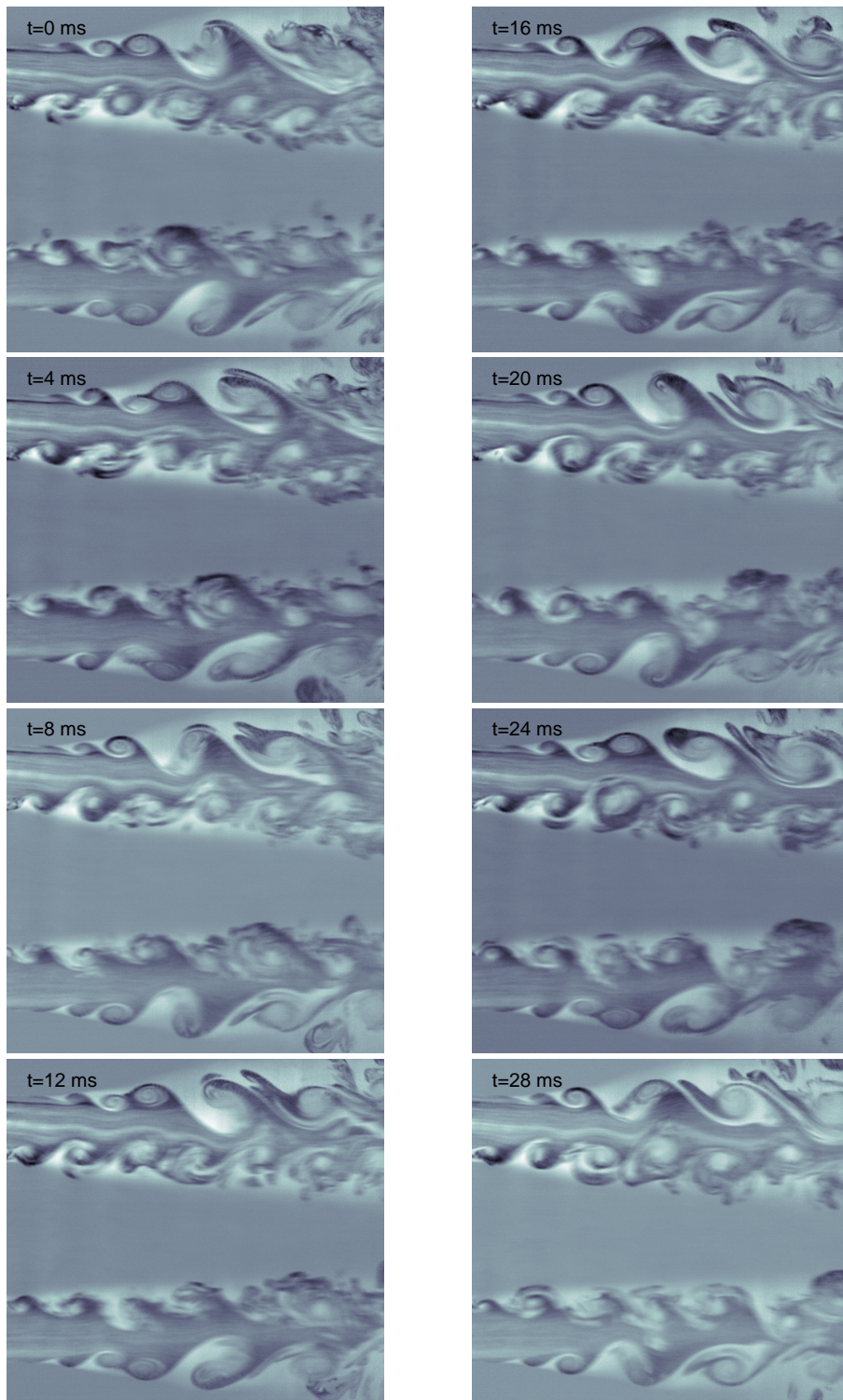


FIGURE 2.11. Instantaneous flow visualizations for $r_u = 1.5$ with the thick wall.

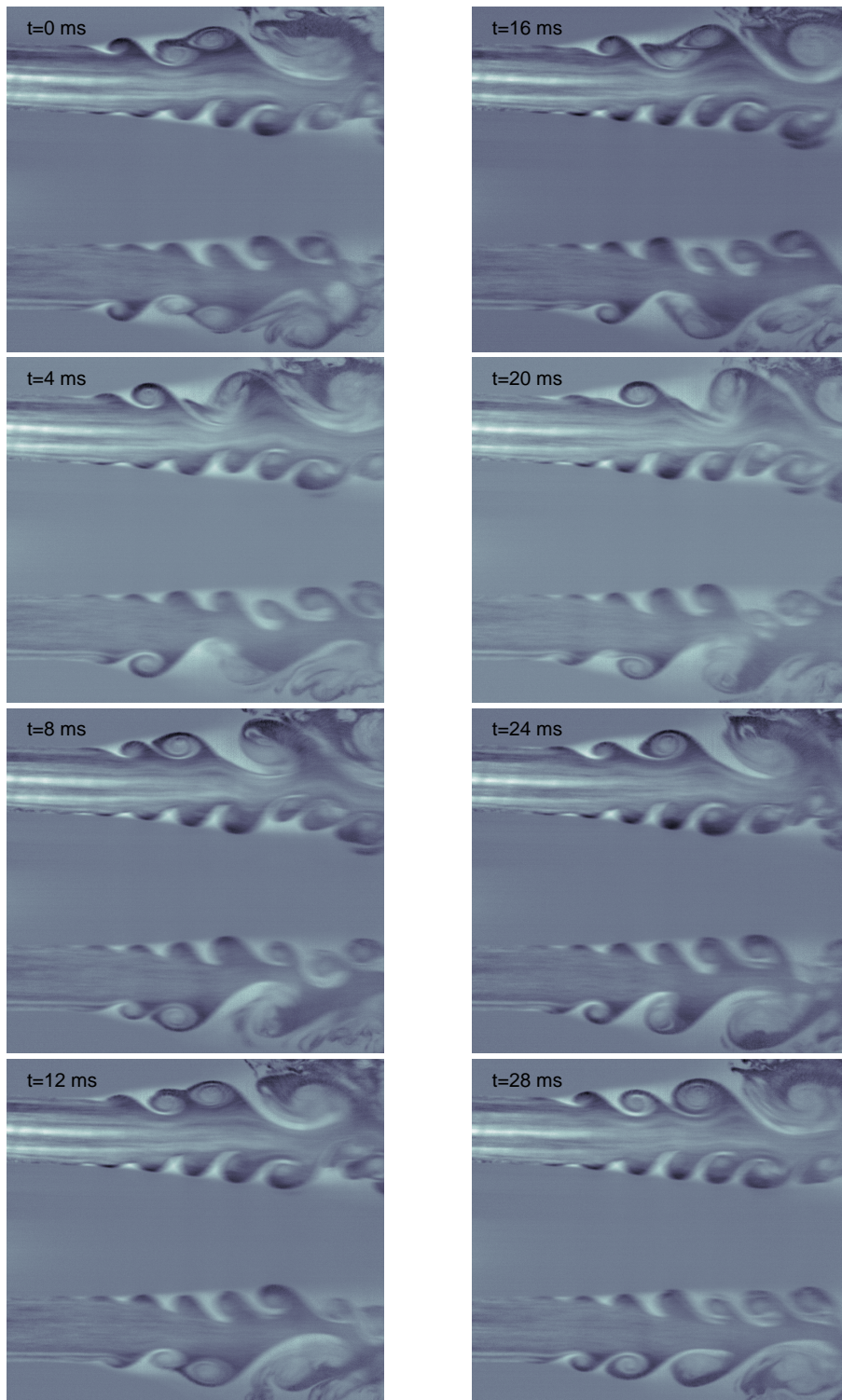


FIGURE 2.12. Instantaneous flow visualizations for $r_u = 1.5$ with the sharp wall.

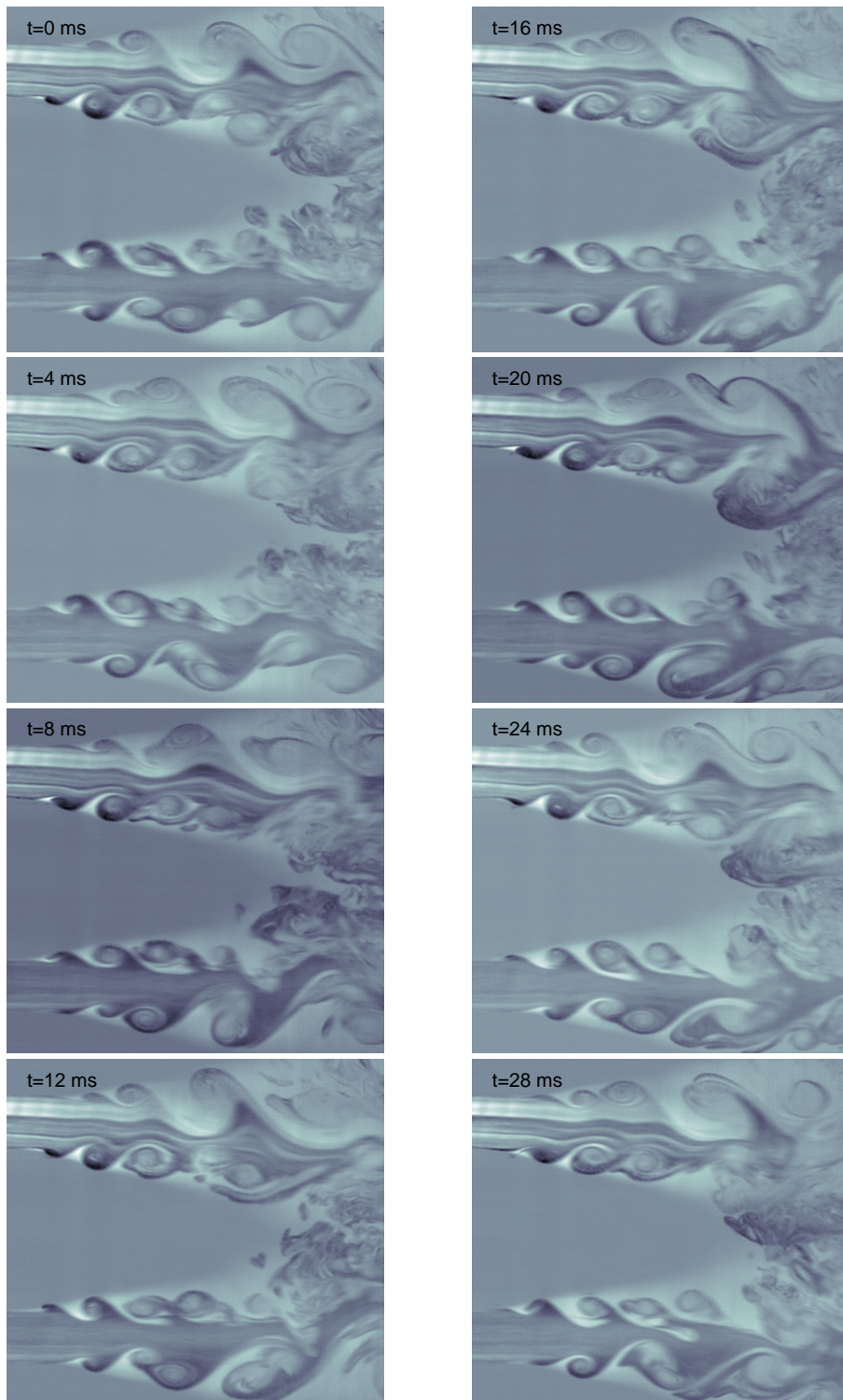


FIGURE 2.13. Instantaneous flow visualizations for $r_u = 3$ with the thick wall.

flow behavior considerably and therefore it has recently received a lot of attention. Flow control in transitional and turbulent flows has become more practical since the recognition of organized motions attributed to coherent structures embedded in the incoherent turbulent background (Hussain 1986; Roshko 1976). Through these coherent structures, which comprise a considerable fraction of the total turbulent energy, ways have been opened to manipulate the dynamics of the flow (Fiedler 1987).

In order to highlight the mechanism governing coherent structures and to enhance our understanding of how these can be utilized to control the transport and mixing characteristics, a variety of passive and active flow control mechanisms have been tested and applied within the last decades, principally in single jets (Bradbury & Khadem 1975; Zaman & Hussain 1981; Tong & Warhaft 1994) and other canonical flows (Gad-el-Hak *et al.* 1998).

In the case of coaxial jets, however, flow control studies have been primarily investigated regarding their receptivity to active flow control strategies (Kiwata *et al.* 2006; Angele *et al.* 2006). Passive strategies, on the other hand, have mainly been disregarded, despite their promising results in other flow cases (Bradbury & Khadem 1975; Zaman & Hussain 1981; Tong & Warhaft 1994; Gad-el-Hak *et al.* 1998). One reason for this imbalance might be the fact that a full characterisation of the apparently simple geometry of coaxial jets, depicted in figure 2.7, is governed by a multitude of parameters (Buresti *et al.* 1994). However, as stated by Burattini (2002) and Talamelli & Gavarini (2006), for some values of the operating parameters there exists a region where the flow is absolutely unstable and this property could be therefore used to control, in a passive way, the flow in the initial and intermediate region.

CHAPTER 3

Experimental setup

3.1. The facility

The experiments have been carried out in the *Coaxial Aerodynamic Tunnel* (CAT) facility in the laboratory of the *Second Faculty of Engineering* in Forlì. The facility, schematically represented in figure 3.1, is composed of two independent centrifugal blowers equipped with three-phase motors (**A** & **B**) whose speed can be controlled independently by means of two frequency inverters. Two pre-settling chambers (**C** & **D**) are placed downstream the blowers to reduce the disturbances from the fans. Four plastic hoses (**L**) connect the outer jet pre-chamber to the corresponding settling chamber (**G**) to increase the symmetry of the flow, while a simple diverging pipe (**E**) connects (**D**) to the settling chamber (**F**). Flow conditioning is performed by means of three screens and a honeycomb in the inner pipe as well as five screens and a honeycomb in the outer circuit (**H**). The inner and outer contraction ratios are 11:1 and 16.5:1, respectively. The inner and outer coaxial nozzles, of exit diameter $D_i = 50$ mm and $D_o = 100$ mm, end with two straight pipes of 100 mm length.

The facility has been designed by Buresti (2000) at the department of aerospace engineering of the University of Pisa (DIA). The setup has been further developed by Burattini (2002) and finally sent to the University of Bologna as part of a cooperation between the two departments.

The experimental facility is placed in a large laboratory and the exit of the coaxial jets is far enough from surrounding walls and the floor, ensuring that the experiments reported here resemble a jet in an infinite environment.

Both, the inner and outer jet velocities have been continuously monitored by means of the pre-settling chambers total pressure, measured with two pressure sensors *SETRA 239*, and corrected by means of a look-up table to include the pressure losses due to the remaining circuit. The total uncertainty of this estimation was of $\pm 1\%$ mainly due to bias error. The estimated inner and outer jet velocities have been used as a feedback information to the inverter in order to maintain constant exit velocities.

In the present experiment, two types of separation wall between the two streams have been used. The first one has a thickness of $t = 5$ mm and ends abruptly in a rectangular geometry. The second one (schematically reported in

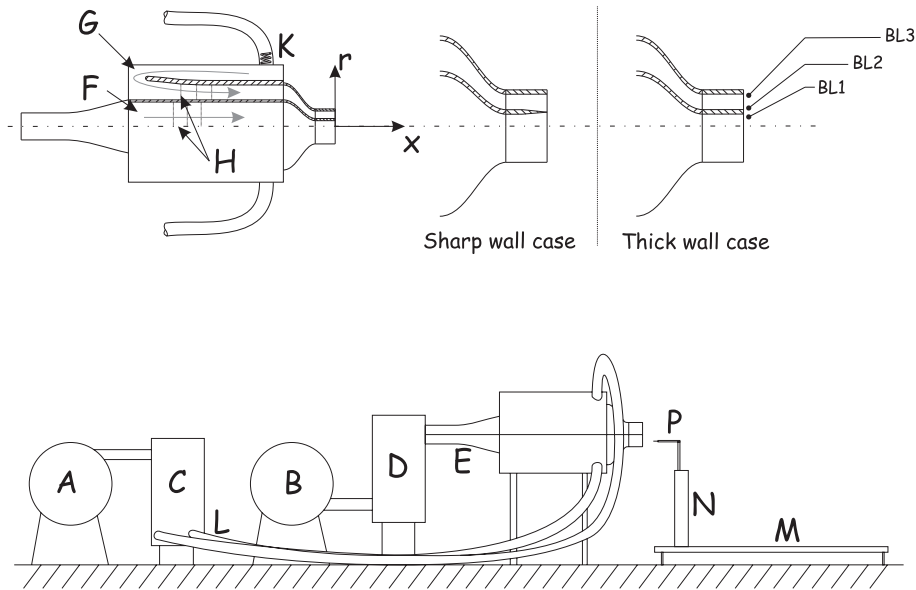


FIGURE 3.1. Schematic view of the facility: (A), outer jet blower; (B), inner jet blower; (C), outer jet pre-settling chamber; (D), inner jet pre-settling chamber; (E), inner jet diffuser; (F), inner jet settling chamber; (G), outer jet settling chamber; (K), electrical resistors; (H), screen and honeycombs; (L), outer jet hoses; (M), axial traversing; (N), radial traversing; (P), probe. The two different separation wall geometries as well as the nomenclature of the boundary layers and the used reference frame are reported on the top of the figure.

figure 3.2) ends with a sharp trailing edge, making the wake thickness negligible ($t \approx 0$ mm) with respect to the sum of the side boundary layers thickness (Dziomba & Fiedler 1985). In the following, the aforementioned separating walls will be referred as *thick* and *sharp*, respectively. For both geometries, the nomenclature of the boundary layers will be the same as reported in figure 3.1.

A strip of sandpaper P280 (with nominal particle diameter of $52 \mu\text{m}$) has been placed 100 mm upstream of the jet exit in the innermost boundary layer in order to suppress an acoustic tone observed when the sharp wall was mounted for high velocities. As will be shown later, the boundary layer BL1 remains still laminar in the thick wall case while it becomes turbulent with the other one.

To characterize the mixing field, the outer jet has been heated by means of four electrical resistors placed at the inlets of the outer settling chamber (K). The amount of temperature increase has been kept small enough to consider the

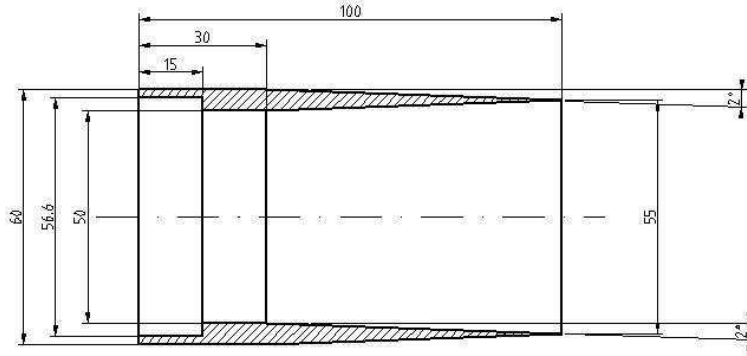


FIGURE 3.2. Detailed shape of the sharp wall geometry.

temperature as a passive scalar and it has been kept still large enough to ensure a high temperature resolution. In accordance with conventional notation, the temperature has been reported in the dimensionless form:

$$\theta = \frac{T - T_{amb}}{T_{max} - T_{amb}},$$

where T is the instantaneous temperature measured by the cold-wire, T_{max} and T_{amb} are the maximum exit and ambient temperature, respectively. The advantage of the above non-dimensionalization is that θ , being a passive scalar, will remain bounded between 0 and 1 (Pope 2000).

In the followings, all capital letters will indicate mean quantities, primes will indicate standard deviation and overbars $\overline{(\cdot)}$ the time average operator. Due to the axial symmetry of this geometry, a cylindrical coordinate system (x, r, ϕ) has been adopted with the corresponding velocity vector components (u, v, w) to indicate the streamwise, radial and azimuthal velocity, respectively. The azimuthal velocity component of this facility was characterized by Burattini (2002) and was found to be negligible at the jet exit.

The cold- and hot-wire probes are finally positioned in the flow by means of a motorized traversing system capable to move the measuring point in the axial (**M**) and radial (**N**) direction. The traversing system and the inverters are controlled by means of a single PC using a *National Instruments* 16 bit PCI-6040E acquisition board. Data acquisition has been performed on a different

computer, in order to avoid electrical noise from the inverters, by means of a *National Instruments* 16 bit PCI-6221 acquisition board.

3.2. Measurement techniques

For the present investigation a variety of hot- and cold-wire probes have been used. The characterization of the exit boundary layers have been done by means of a *DANTEC* 55P11 single wire probe, while all other measurements have been performed by means of a *DANTEC* 55P61 X-wire probe in combination with a self-made cold-wire probe with an 2.5 micron Platinum wire with a length-to-diameter ratio of 200. The cold-wire has been placed around 0.5 mm upstream and apart from the X-wire with an angle of 35° to the X-wire, to reduce the blockage downstream the X-wire.

The hot-wires have been operated in constant temperature (CT) mode with a resistance overheat ratio of 80 %, whereas the cold-wire in constant current (CC) mode at a constant current of 0.5 mA, by means of an *DANTEC Stream-Line* and an *AA-lab AN-1003* hot-wire anemometry system, respectively. The signals from the CTA and CCA channels have been shifted with an offset and amplified through the anemometric circuits to match the fluctuating signal components to the voltage range of the 16-bit A/D converter used, and then digitized on a PC at a sampling frequency of 10 kHz and a sampling duration between 20 and 50 seconds, depending on the experimental set and on the downstream position of the probe. The axial and radial velocity as well as the temperature have been acquired simultaneously enabling, therefore, the instantaneous compensation of the velocity readings (Bruun 1995) as well as the calculation of the instantaneous heat fluxes.

The cold- and hot-wires have been initially calibrated slightly upstream the inner nozzle against a thermocouple and Prandtl-tube, respectively. Due to the small diameter and the low current through the cold-wire (i.e. 0.5 mA), the anemometer output becomes a linear function of the fluid temperature and insensitive to velocity. During the measurements, an automatic calibration system has been implemented to re-calibrate the hot-wire periodically by measuring the stagnation pressure in the inner jet pre-settling chamber minus the ambient pressure $p_0 - p_\infty$, and by using a pre-determined function to relate it with the dynamic pressure at the jet exit $p_{0exit} - p_\infty$. The used relationship has been:

$$(p_{0exit} - p_\infty) = (p_0 - p_\infty) - f(p_0 - p_\infty)$$

where $f(p_0 - p_\infty)$ is a second order polynomial obtained by a previous calibration of the facility. An example of $f(p_0 - p_\infty)$ is reported in figure 3.3. For each change in geometry this calibration has always been re-performed.

Since most of the measurements have been performed during night time, a special Labview VI has been developed to automatically measure the local velocity and temperature of pre-defined points in some parameter space (for

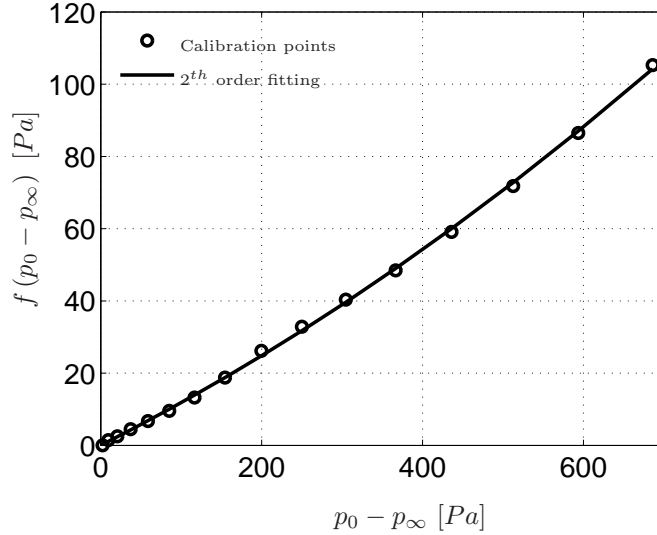


FIGURE 3.3. Pressure losses in the inner circuit with the thick separating wall plotted with a 2th order polynomial fitting function.

instance, the span of (x, r, U_i, U_o, Θ)). A special device has been designed to turn on and off the heating of the outer jet by means of Labview in such a way that the VI was able to control the jets velocity, correct them, and proceed independently from any human action. Through the program LogMeIn it has been possible anyway to control the VI from a remote desktop and, eventually, to update some input. Special care has been devoted in the arrangement of the inverters and heating control in a computer segregated by the computer dedicated to the measurements. The communications between the two computers have been performed through Ethernet. No electrical noise augmentation has been observed due to this connection.

The calibration has been performed automatically every 3/4 hours, depending on the test to be performed. A fourth order polynomial calibration law has been used to convert the sampled tension value to the effective velocity felt by the hot-wire. Even if this method does not take into account any thermal correlation like the King's Law (Bruun 1995), the advantage of the polynomial fitting is the easy and automatic implementation with a very good regression curve. On the other hand, the use of a polynomial fitting is far from the physics of the cooling law of the wire and, indeed, does not allow the extrapolation of the calibration curve outside the calibration range. An example of the calibration curve and its fitting is reported in figure 3.4 where the excellent agreement is clearly visible.

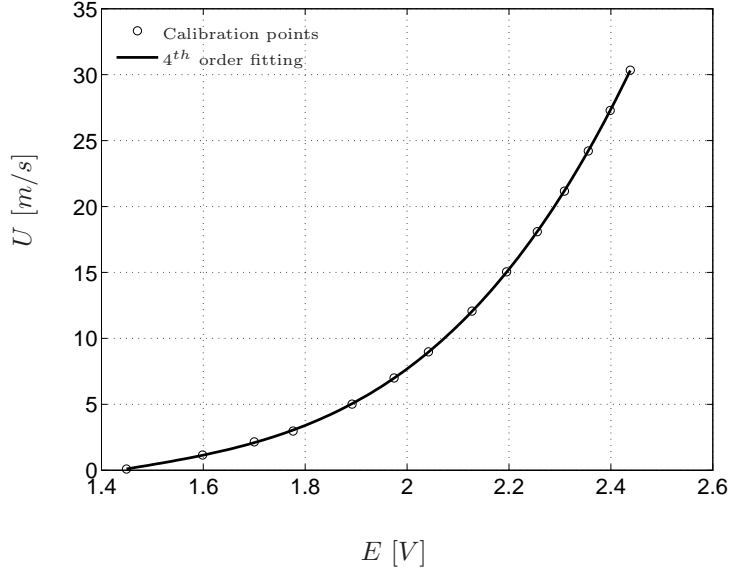


FIGURE 3.4. Example of an hot-wire calibration fitted with a 4th order polynomial function.

The directional calibration has been performed separately by changing the flow direction with respect to the probe and applying linear square fitting methods to estimate the directional coefficient β in such a way that, given the measured effective velocities U_{e1} and U_{e2} , the streamwise and radial velocity components are estimated as:

$$U = \frac{U_{e1} + U_{e2}}{2} \quad (3.1)$$

$$V = \beta \frac{U_{e1} - U_{e2}}{2} \quad (3.2)$$

It is possible to verify that these relationships follow directly from the Jorgensen law (Bruun 1995), provided that the angle between the local flow direction and the probe axis is small and that $U_{e1} = U_{e2} = U$ if $V = 0$. Figure 3.5 reports the comparison between the real velocity components value and the linear behavior expressed by equations 3.1 and 3.2 where a good agreement is observable. Once the β coefficient is found, it is assumed implicitly that this coefficient does not change with the environmental parameters, and it is just function only of the wire geometry independently on the various velocity calibrations performed during the experimental campaign.

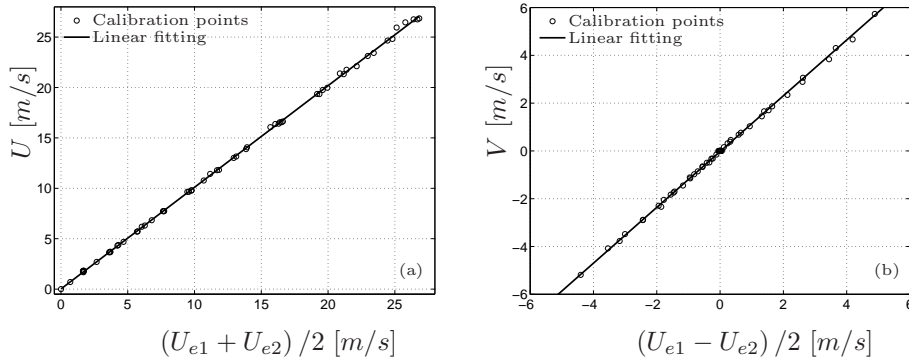


FIGURE 3.5. Directional calibration curves. (a) Streamwise velocity calibration. (b) Radial velocity calibration

3.2.1. Conditional sampling technique

For all the studied cases, a conditional sampling technique has been applied to the data by means of a fourth wire to acquire a reference signal. This procedure has allowed the detection of events used as triggers in the eduction approach, as discussed by Zaman & Hussain (1984), with the goal to highlight the vortex evolution in a cross plane. By placing a SW probe as schematically reported in figure 3.6, a triggering signal has been obtained and conditional sampling methods applied to the signal from the main probe. The triggering event has been defined as the instant where the instantaneous triggering signal exceeded its average by a certain percentage of its rms value (namely $u_{trig} > U_{trig} + \alpha u'_{trig}$ for $\alpha = 1$), similar to the procedure applied by Zaman & Hussain (1984).

This technique, applied to both velocity components and temperature, has allowed a statistical description of structures with a strong azimuthal correlation (the azimuthal distance of the two probes was $\Delta\phi = \pi/2$) in terms of passage frequency and eddy size and position. For each trigger event, more than five periods of the original signals have been stored and averaged with the previous frames. This allowed the characterization of the structures as well as to verify their effective periodicity.

3.2.2. Flow visualizations

Flow visualizations have been performed by means of smoke injected in the outer jet settling chamber. A continuous Argon laser sheet has been used to illuminate the vertical plane where the inner jet axis belonged. A *DANTEC Nanosense MK1* camera has acquired instantaneous pictures with a rate of 1 kHz. Due to camera resolution issues, the Reynolds number of the flow visualizations has been kept smaller than hot-wire measurements and, therefore,

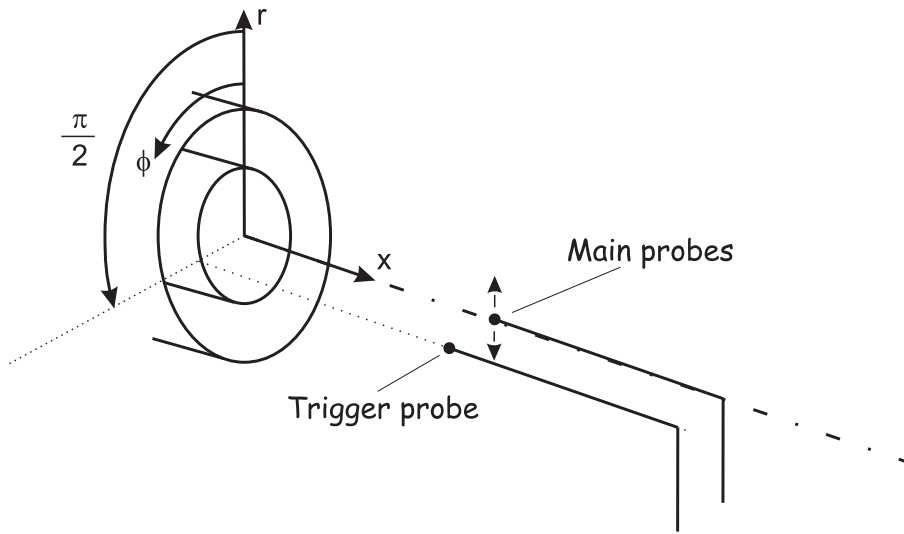


FIGURE 3.6. Sketch of the probe positions in the triggering experiments.

here the visualizations are used just to have a qualitative description of the investigated regimes.

Due to some reflected light on the pipe walls, all the images have been slightly disturbed by a systematic noise (as can be appreciated from figure 1.2 where no treatment has been used). To reduce this effect, the average of all the available images has been removed to each instantaneous realization. This operation does not change the detail of the vortex structures in each image, but increases the clarity of each picture.

3.3. Experiments with acoustic excitation

A *Dantec* X-wire 55P61 probe has been placed in the measuring control point ($x/D_i = 0.25$ $r/D_i = 0.5$) while a *Dantec* single wire 55P11 probe has been positioned at the inner jet exit ($x/D_i = 0$ $r/D_i = 0$) to measure the excitation level by means of the streamwise velocity power density spectra around the exciting frequency.

The excitation device has been composed by a 12-inches loudspeaker connected with a *Behringer* EP2500 amplifier driven by the audio board of a PC. The loudspeaker has been placed on the top of the pre-settling chamber of the inner jet (as schematically represented in figure 3.7 in **Q**) and forced the inner jet with a sine wave of chosen amplitude and frequency. In this experiment, the outer jet velocity has been kept fixed to two possible values (namely $U_o = 5$ m/s or $U_o = 20$ m/s), changing only the inner jet one and the forcing frequency and amplitude.

the effect of an increasing forcing amplitude in the flow at the control point. All the time histories have been acquired for 40 s with a sampling frequency of 10 kHz.

3.4. Initial conditions

The nomenclature of the three boundary layers is reported in figure 3.1. As a further notation, the momentum thickness of BL1 will be called θ_i , while the same thickness of BL3 will be called θ_o , namely they will be considered as respectively inner and outer length scales of the shear layers.

The details of the boundary layers at the jets exits have been reported in table 1 where some power law coefficients are given to calculate the momentum thickness and the maximum rms amplitude for a given Reynolds number $Re = U_\infty D_i \nu$ (U_∞ is the inner jet velocity for BL1 and outer jet velocity for BL2 and BL3). Also, it is reported the mean shape factor \bar{H} , δ_{99}/θ thickness ratio and the Pohlhausen Λ coefficient to re-construct the boundary layers as an approximate polynomial function (Schlichting 1968) to give a complete description of the initial conditions for future CFD comparisons.

Figures 3.8-3.12 report the mean and rms streamwise velocity profiles for all the characterized configurations. In particular, in figures 3.8 and 3.11 it is possible to evince the dramatic change of the boundary layer BL1 due to the different separating walls. It is evident that, while in the thick wall case BL1 is still laminar and almost self-similar, even at the lowest Reynolds number, this is not the case of the sharp separating wall where the boundary layer BL1 appears to be still transitional and reaches the self-similar turbulent state for $Re_\theta \geq 500$. The switch to a turbulent boundary layer state was principally due to the fact that the sharp wall presents a diverging section where the velocity decreases, reducing consequently the stability of the velocity profile to external perturbations. On the other hand, the boundary layer BL2 is laminar independently from the separating wall geometry as indicated in table 1 and from figures 3.9 and 3.12. The outermost boundary layer has been characterized only with the thick wall and no remarkable differences have been observed with the sharp wall mounted.

It is worth to mention the different behavior of the streamwise velocity rms profile in BL1 for the two different lip geometries: with the thick wall the rms increases as Re_θ increases, with a maximum at $y \approx \theta$ independent of Re_θ . The opposite trend is observed in the BL1 of the sharp wall case where the velocity rms maximum value decreases by increasing the Reynolds number, suggesting that a separation bubble is probably present inside the duct and that spatial resolution issues are present ($L^+ = 30$ already at $Re_\theta = 500$, see appendix B). In the sharp wall BL2 there is no hint of such behavior except for the lowest Reynolds number.

Thick wall case

	state	A	n	B	k	Λ	\bar{H}	$\frac{\delta_{99}}{\theta}$
BL1	laminar	0.4023	-0.4142	$3.565 \cdot 10^{-6}$	0.8425	3.126	2.393	7.046
BL2	laminar	0.354	-0.4208	$8.357 \cdot 10^{-5}$	0.5941	12.007	2.247	7.828
BL3	laminar	0.7849	-0.4564	$4.470 \cdot 10^{-11}$	1.7711	-3.399	2.745	7.548

Sharp wall case

	state	A	n	B	k	Λ	\bar{H}	$\frac{\delta_{99}}{\theta}$
BL1	turbulent	$4 \cdot 10^{-3}$	0.2785	7.036	-0.3745	N.D.	1.689	8.010
BL2	laminar	0.2187	-0.3387	$2.7 \cdot 10^{-3}$	0.1983	1.951	2.540	8.450

TABLE 1. Boundary layer properties for both separating wall geometries. Here are reported the coefficients related to the relations $\theta/D = A \cdot Re^n$ and $u'_{max}/U_\infty = B \cdot Re^k$, the Pohlhausen Λ coefficient, the mean shape factor \bar{H} and the ratio $\frac{\delta_{99}}{\theta}$.

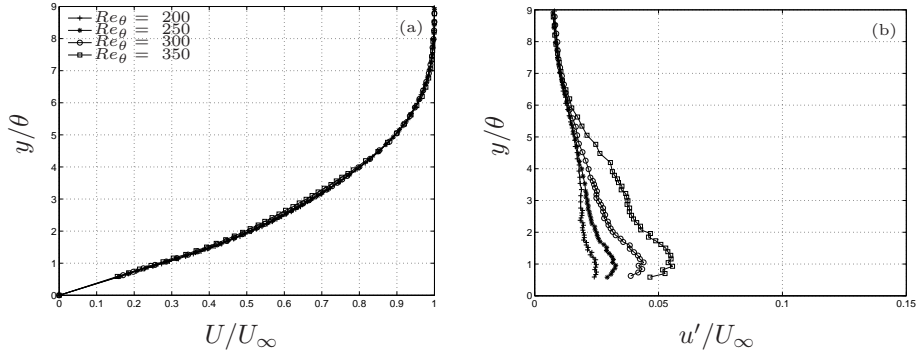


FIGURE 3.8. Boundary layer BL1 for different Re_θ in the thick separating wall case. (a) Mean velocity profiles, (b) Velocity rms profiles

3.5. Accuracy Tests

To evaluate the precision of the measurements, a set of 50 velocity profiles of a single jet with $U_0 = 15 \text{ m/s}$ has been acquired. The 95% confidence interval of the most important statistics, scaled with the jet velocity, is reported in table 2. On the other hand, figure 3.13 reports the mean and rms streamwise and radial velocity profiles with error bars provided by the standard deviations.

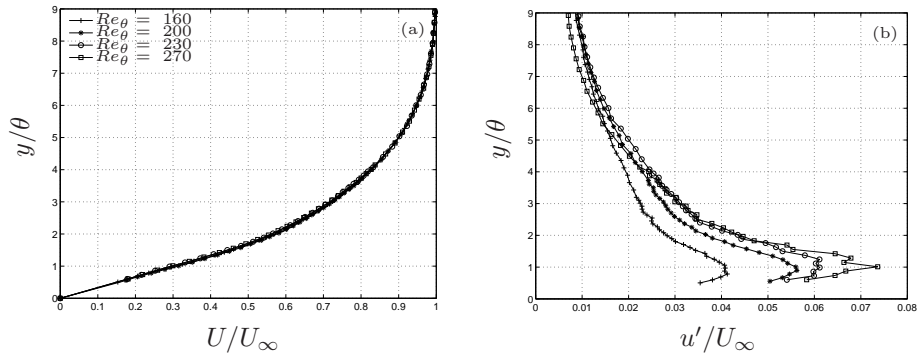


FIGURE 3.9. Boundary layer BL2 for different Re_θ in the thick separating wall case. (a) Mean velocity profiles, (b) Velocity rms profiles

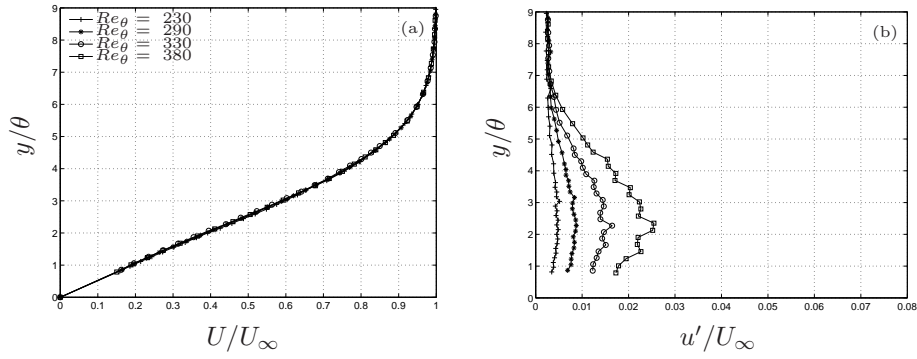


FIGURE 3.10. Boundary layer BL3 for different Re_θ in the thick separating wall case. (a) Mean velocity profiles, (b) Velocity rms profiles

Since the hot-wire has been calibrated with a corrected Prandtl tube, the accuracy has been affected by an uncertainty error of 0.6%, which comprises a 1% error of the calibration of the two total pressures (at the stagnation chamber and at the jet exit), and the error sources from the uncertainties of the pressure sensor, of the temperature sensor and of the absolute pressure value.

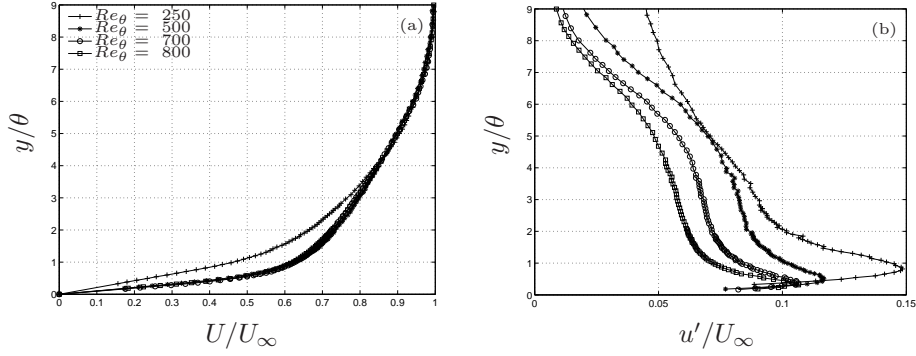


FIGURE 3.11. Boundary layer BL1 for different Re_θ in the sharp separating wall case. (a) Mean velocity profiles, (b) Velocity rms profiles

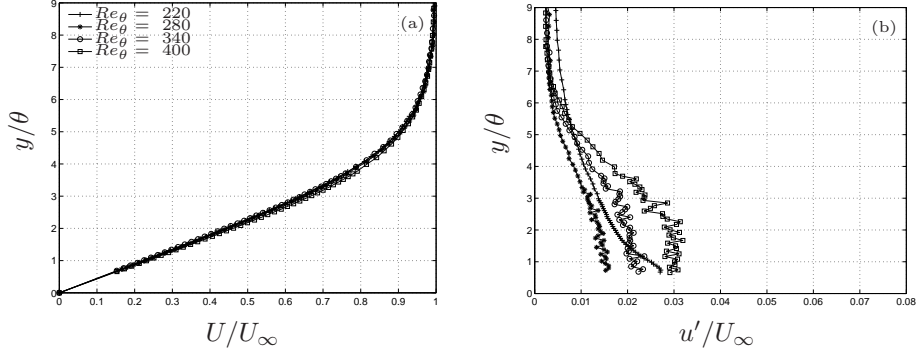


FIGURE 3.12. Boundary layer BL2 for different Re_θ in the sharp separating wall case. (a) Mean velocity profiles, (b) Velocity rms profiles

TABLE 2. Standard deviation of statistical quantities.

variable	Precision (P=0.95)
U/U_0	0.0045
V/U_0	0.0027
u'/U_0	0.0027
v'/U_0	0.0027
\overline{uv}/U_0^2	0.00024

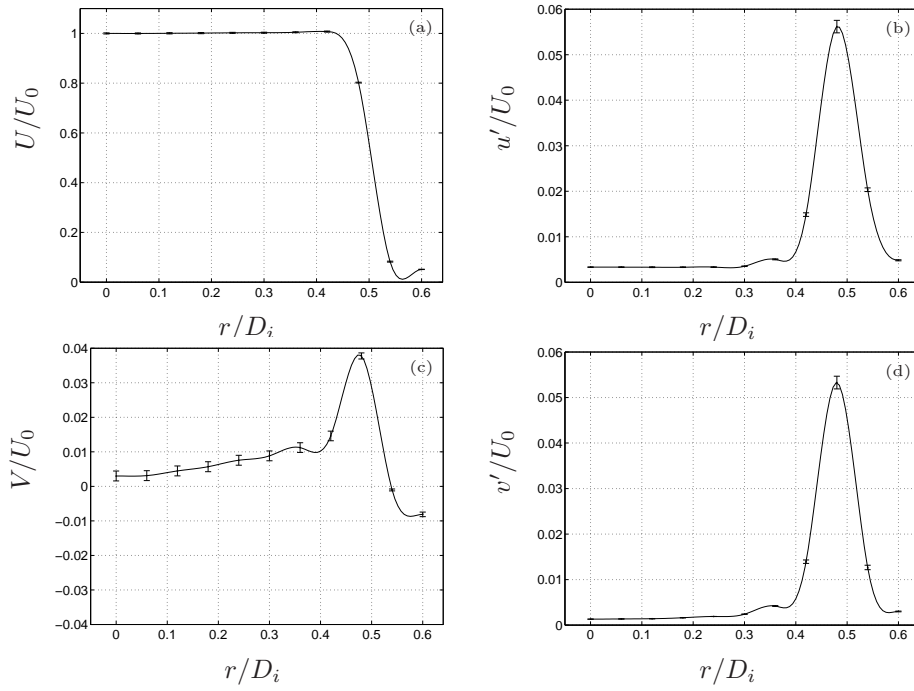


FIGURE 3.13. Velocity profile of a single jet with the error bars at $x/D_i = 0.5$. (a) U/U_0 , (b) u'/U_0 , (c) V/U_0 , (d) v'/U_0

CHAPTER 4

Effects of vortex shedding in the near field

The material reported in this chapter has been presented by Örlü, Segalini, Alfredsson & Talamelli (2008a) in the International Conference on Jets, Wakes and Separated Flows (ICJWSF-2008) during September 16–19, 2008, at the Technical University of Berlin (Germany).

4.1. Generalities

As discussed in the backgrounds, the prevailing model for more than a decade, put forward by Ko & Kwan (1976), was that coaxial jets could be considered as a simple combination of single jets, where the two shear layers originating from the nozzles develop independently from each other. This view was modified when Dahm *et al.* (1992) in their flow visualisation study evinced the existence of different topological flow regimes for different velocity ratios, $r_u = U_o/U_i$ (here U_i and U_o denote the maximum absolute velocity of the inner and outer streams at the nozzle exits, respectively), as well as absolute velocities. Furthermore the same authors, as well as Wicker & Eaton (1994), found that the vortical motion for $r_u > 1$ is dominated by the vortices emerging in the outer shear layer. They showed that the evolution of the inner shear layers vortices is dictated by the outer vortices motion and hence trapped in the spaces left free between two consecutive outer shear layers vortices; this scenario became known as the so-called ‘locking phenomenon’. Consequently, the vortex passage frequency of the inner shear layer will differ from the one predicted by stability analysis for a single axisymmetric shear layer, as shown by Dahm *et al.* (1992) and da Silva *et al.* (2003) by means of flow visualisations and direct numerical simulations, respectively. This finding has led to an increased focus on the control of the outer shear layers’ vortices (Balarac & Métais 2005; Angele *et al.* 2006).

One of the parameters, emphasised by Buresti *et al.* (1994), playing an important role in the evolution of transitional coaxial jets, is the thickness of the (duct) wall, t , separating the two streams from each other. It was shown by the same authors that two trains of alternating vortices are shed from both sides of the inner wall with a well-defined frequency, which scales with the wall thickness and the average velocity of the two streams. In fact both the geometry of the inner wall thickness and the velocity ratio were found to be

crucial in determining whether the behaviour in the near-field of coaxial jets could be considered as wake-like or shear-layer-like (Dahm *et al.* 1992; Braud *et al.* 2004).

In a recent study Talamelli & Gavarini (2006) formulated a theoretical background for this experimental finding. They showed, by means of linear stability analysis, that the alternate vortex shedding behind the inner wall can be related to the presence of an absolute instability, which exists for a specific range of velocity ratios and for a finite thickness of the wall separating the two streams. The authors proposed that this absolute instability may provide a continuous forcing mechanism for the destabilisation of the whole flow field even if the instability is of limited spatial extent. It is important to point out that this mechanism does not require any external energy input, being considered passive, and therefore is attractive for practical applications.

In the following three sections, results from the sharp and thick wall cases are presented to highlight the effect of the presence of the vortex shedding mechanism on interacting shear layers (section 4.2), its utilisation to control the flow dynamics (section 4.3) as well as its effect on the turbulence activity (section 4.4).

The results shown here are all for the case of equal maximum velocities in the inner and annular jet, i.e. $r_u = 1$. The Reynolds numbers investigated range from around 12000 to 100000, based on the inner nozzle diameter, corresponding to absolute velocities of 4 and 32 m/s, respectively. The velocity ratio of unity was selected, because it lies within the range for which an absolute instability behind a thick wall has theoretically been shown to exist (Talamelli & Gavarini 2006).

4.2. Vortex shedding effect on interacting shear layers

In the case of the sharp wall, the power-spectral density of the fluctuating streamwise velocity component in the inner and outer shear layer as well as a snapshot of a smoke visualisation are shown in figure 4.1 and 4.2, respectively. The Kelvin-Helmholtz instability emerging between the annular stream and the ambient is clearly highlighted in the visualisation as well as in the spectral content of the flow (~ 240 Hz corresponding to a Strouhal number of 0.012 based on the momentum thickness of the external boundary layer, which is related to the ‘shear layer mode’; cf. Zaman & Hussain (1980)). As the snapshot suggests, the flow behind the outer separating wall resembles a picture of a classical Kelvin-Helmholtz instability, whereas the sharp inner separating wall produces a smooth interface between the coflowing jets, being free of any apparent trace of a wake.

For the thick wall, on the other hand, both the smoke visualisation as well as spectral content of the flow, have strong imprints of the vortex shedding behind the inner wall. This changes the flow scenario drastically, as evident

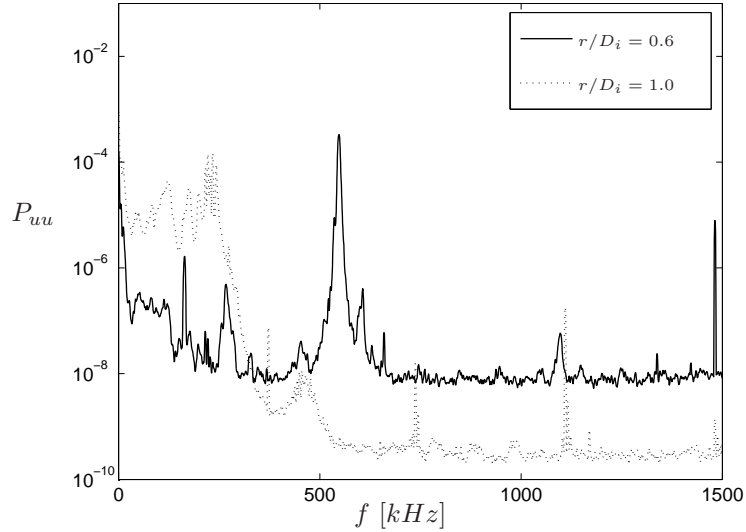


FIGURE 4.1. Power-spectral density function of the stream-wise velocity component measured behind the inner ($r/D_i = 0.6$) and outer ($r/D_i = 1.0$) wall at $U_o = 8$ m/s and $x/D_i = 0.5$ for the sharp wall.

from figures 4.3 and 4.4. In contrast to the sharp wall results, the spectral energy is highly concentrated in its fundamental peak and harmonics as well as in the incoherent background fluctuations, anticipating an increased turbulence activity as well as the presence of organised structures.

The vortex shedding, starting right behind the inner wall and hence upstream the first emergence of the Kelvin-Helmholtz instability of the outer shear layer in the sharp wall case, traps the outer shear layers vortices into the free spaces left between the ones of the inner shear layer. This increases the coherency between the two shear layers and can further be evinced through figure 4.5, where a pseudo-flow visualisation has been plotted through a conditional sampling technique. The vortices in the outer shear layer resemble the famous Kelvin's 'cat's eye' pattern predicted by stability analysis (Drazin 2002), whose organisation is strongly coupled to the vortex shedding in the inner shear layer. This again underlines the strong organisation and mutual interaction of the two shear layers in the whole near-field region as could be anticipated from the flow visualisation. An X-wire probe was thereby triggered by the vortex shedding behind the inner separating wall detected by a single hot-wire probe which was placed at the same downstream location, $x/D_i = 0.26$. Figure 4.6 depicts the conditionally sampled fluctuating axial and radial velocities above their mean

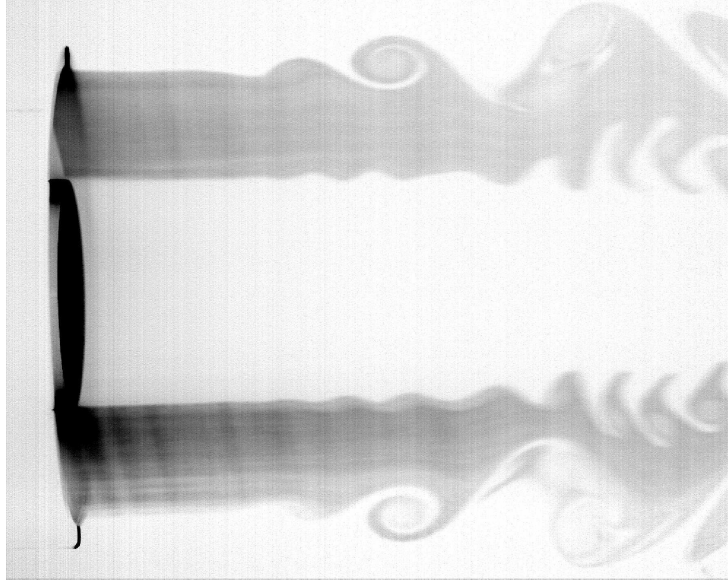


FIGURE 4.2. Smoke flow visualisation at $U_o = 4$ m/s and $r_u = 1$ for the sharp wall.

in the outer shear layer, $r/D_i = 1$, at $x/D_i = 0.26$ from an X-wire probe triggered by a single hot-wire probe placed at the same downstream location, but within the wake of the inner wall, $r/D_i = 0.6$. The clear cyclical path in the (u, v) -space is a strong indication for the presence of a dominant peak in the outer region, and may also anticipate a formation of larger vortices (Fiedler 1987).

The clear spectral peak of the vortex shedding phenomenon, the pronounced fundamental and its harmonics in the outer shear layer in figure 4.3, anticipate a clear cyclical path of the streamwise and radial velocity component as found in the conditionally sampled pseudo-flow visualisation. Although the instantaneous smoke visualisation image has been taken at a lower velocity (due to the difficulty to obtain expressive images at higher velocities), compared to the presented spectral measurements and pseudo-flow visualisation, its spatial character complements the quantitative time evolution of the two point hot-wire measurements.

The above mentioned demonstrates that the recent finding of Balarac & Métais (2005), who showed that (below a critical velocity ratio) the vortices of the outer shear layer develop with a Strouhal number corresponding to the value predicted by linear stability analysis for the Kelvin-Helmholtz instability, is therefore not generally true. In particular for the presence of an absolute

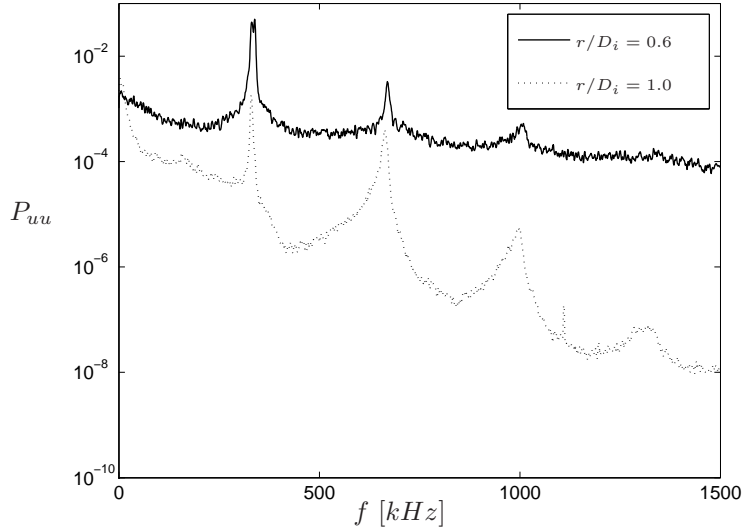


FIGURE 4.3. Power-spectral density function of the stream-wise velocity component measured behind the inner ($r/D_i = 0.6$) and outer ($r/D_i = 1.0$) wall at $U_o = 8$ m/s and $x/D_i = 0.5$ for the thick wall.

instability, which—as shown in figures 4.3 and 4.4—dominates the motion of the organised structures.

4.3. Vortex shedding as a passive flow control mechanism

So far we have shown the effect of the vortex shedding on the near-field dynamics of a coaxial jet. The next paragraphs are devoted to the question whether or not the vortex shedding can be used as a viable flow control mechanism and how it effects the turbulence activity. Figure 4.7 shows the fundamental peak frequency as a function of the absolute velocity for both wall cases. No trend or relationship is observable for the sharp wall case (a) between the vortices in the inner and outer shear layer, whereas the strong controllability of the evolution of the vortices' fundamental frequency in both shear layers is evident from the linear relationship with the absolute velocity in the thick wall (b) case. Hence the absolute instability, by means of the induced vortex shedding behind the inner wall, dictates the evolution of the vortices in both shear layers and hence the whole flow field.

The overlapping at 16 and 20 m/s for the sharp wall in figure 4.7 could be explained by a whistler tone, which was observed around these absolute velocities (Örlü *et al.* 2008*b*). However, there is no controllability of the fundamental peak, in the sharp wall case, whereas the thick wall presents a means



FIGURE 4.4. Smoke flow visualisation at $U_o = 4$ m/s and $r_u = 1$ for the thick wall.

to predetermine the evolution of the vortices in the inner and thereby outer shear layer, just by knowing the separating wall thickness, t , and the absolute velocity, U_o , or the average velocity for the case of unequal velocities within the range of the presence of an absolute instability.

4.4. Vortex shedding effect on the turbulence activity

In the presence of active excitation, where the amplitude and phase of the excitation signal can arbitrarily be set, an increase in the organisation and formation of larger vortices can result either in a turbulence suppression (Zaman & Hussain 1981; Dahm *et al.* 1992) or an turbulence enhancement (Zaman & Hussain 1980; Crow & Champagne 1971). The already shown power-spectral density functions anticipated that the energy content of the flow, for the presence of the vortex shedding, is not only brought about by means of the emergence of larger organised structures, but also by a drastic increase in the incoherent background turbulence. Finally the normalised root mean square values of the radial velocity fluctuations along $r/D_i = 1$ for 4, 8 and 12 m/s are shown in figure 4.8 for the sharp (a) and thick (b) wall to complete the picture. A clear increase in the root mean square value of the radial velocity fluctuations can be observed for all shown downstream positions as well as absolute velocities. Consequently the thick wall can be used not only to trigger and hence control

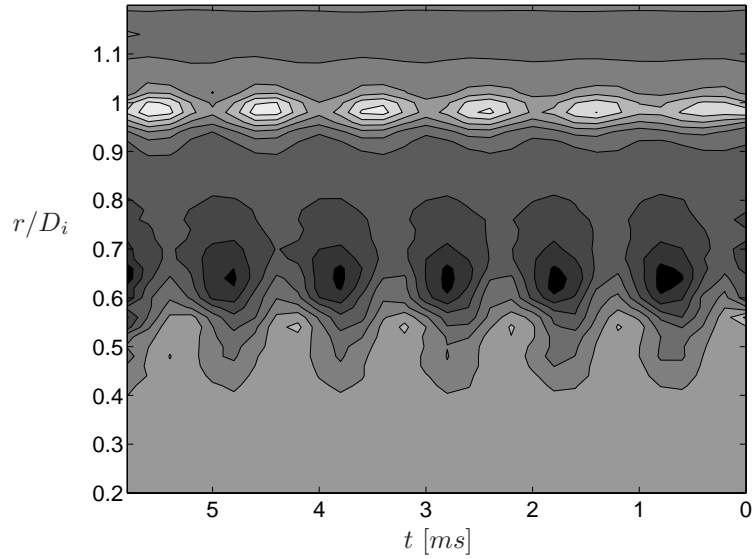


FIGURE 4.5. Pseudo-flow visualisation by means of conditional sampling technique of the radial velocity component at $U_o = 20$ m/s and $r_u = 1$ for the thick wall. Colormap from white to black corresponding to inflow and outflow conditions, respectively.

the evolution of the organised structures, but also—and this is of more practical importance—to increase the turbulence activity within the inner and outer shear layers and thereby the mixing between the two coaxial jets streams as well as the annular jet with the ambient fluid.

A probably larger turbulence enhancement can be obtained if both fluid mechanical and geometrical parameters of the coaxial jet, like momentum thicknesses or the thickness of the separating wall, could be more easily varied.

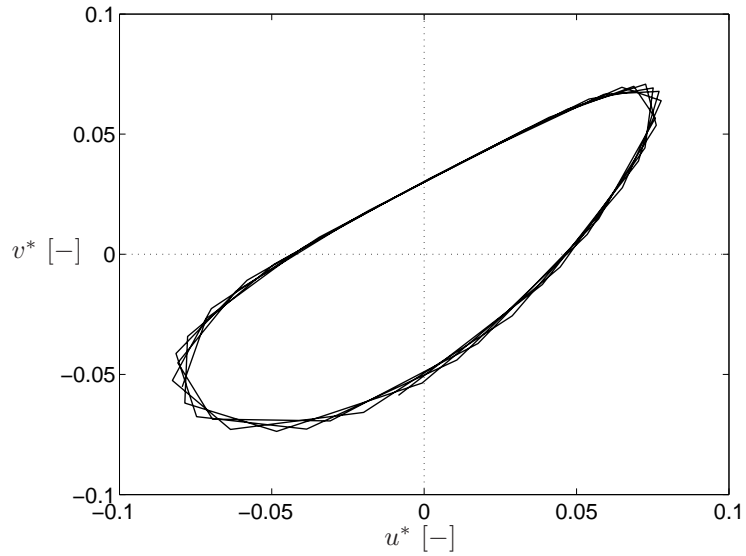


FIGURE 4.6. Conditionally sampled velocities plotted in the (u, v) -space above their mean for the clean wall case for $U_o = 20$ m/s at $x/D_i = 0.26$ in the outer shear layer, $r/D_i = 1$.

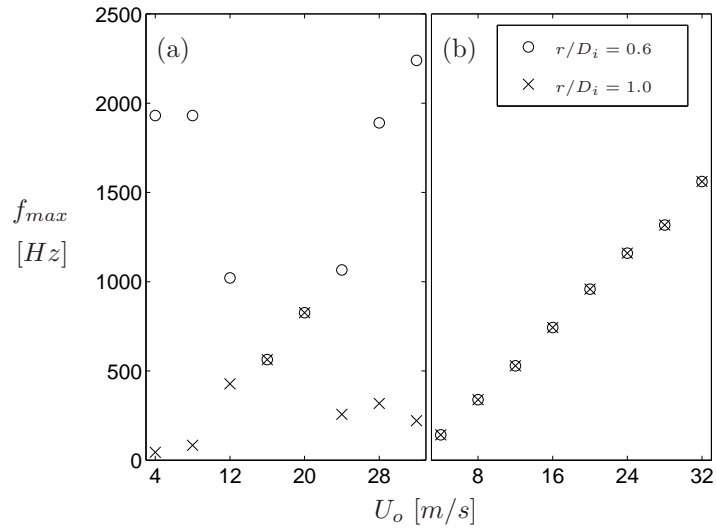


FIGURE 4.7. Fundamental frequency as function of the outer jet velocity behind the inner and outer wall at $r_u = 1$ and $x/D_i = 0.26$ for the sharp (a) and thick (b) wall.

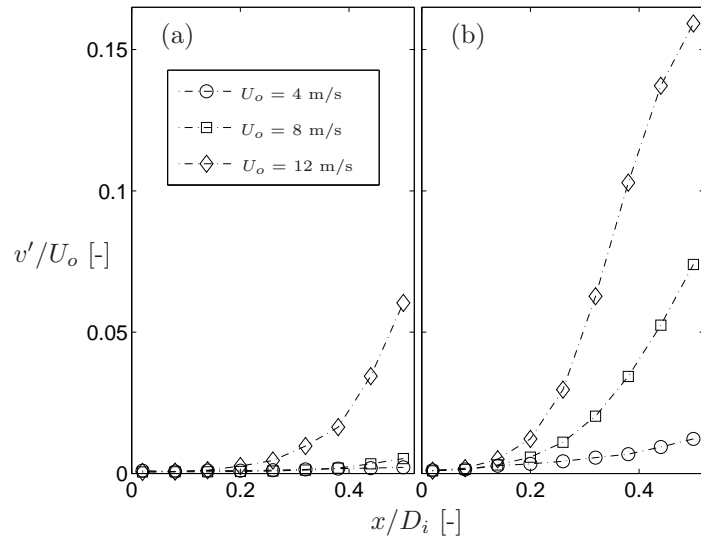


FIGURE 4.8. Root mean square value of the radial velocity fluctuations along $r/D_i = 1$ at 4, 8 and 12 m/s for the sharp (a) and thick (b) wall.

Dominant instabilities in the near field

5.1. Generalities

As reviewed in the past chapters, several experiments (Ko & Kwan 1976)-(Dahm, Frieler & Tryggvason 1992) and numerical simulations (da Silva, Balarac & Métais 2003) were able to highlight many important aspects which are related to the dependence of the flow field on the various parameters. Dahm *et al.* (1992), by means of flow visualizations, pointed out that in the near field region the vortex pattern is a strong function of the velocity ratio r_u and the Reynolds number of both streams. An interesting outcome of this research was that the dynamics of both shear layers was somehow different from that of the single jet case, and underlines the presence of a complex interaction between the vortices of ISL and OSL which affects the vortex formation in the near field region.

Dahm *et al.* (1992) and da Silva *et al.* (2003) investigated the behavior of coaxial jets at high velocity ratios, showing that, if the velocity ratio is high enough, there is a dominance of the OSL which dictates the vortex formation frequency in both shear layers (so called lock-in phenomenon).

Investigating a coaxial jet geometry with a thick separating wall, Buresti, Talamelli & Petagna (1994) showed that, for moderate velocity ratios, an alternate vortex shedding from the separating wall can be observed. This phenomenon, due to the non-negligible separating wall wake, excites the flow at a frequency f_{vs} that the authors scaled with the thickness of the wall t and with the average velocity of both streams $U_m = (U_i + U_o)/2$, suggesting a characteristic Strouhal number $St_t = f_{vs}t/U_m$ of about 0.24. In his PhD thesis, Burattini (2002) showed further evidences of the clear effect of the separating wall; particularly, he focused on the different operating regimes of coaxial jets. He observed that the shedding frequency did not scale perfectly with the average velocity and with thickness of the separating wall and, therefore, he conjectured that the collapsing of the dimensionless frequencies could be improved by taking into account the presence of the boundary layers.

A theoretical analysis was performed by Talamelli & Gavarini (2006), who exploited the linear spatial stability theory in order to both determine the instability modes present in this geometry and find the range of operating parameters where a region of absolute instability was present. They found that three unstable modes are present: one corresponding to external shear layer and two associated with the presence of the inner duct wall wake. For sufficiently high velocity defect and for a limited range of velocity ratios around 1, one of these last two modes may locally become absolutely unstable. Örlü *et al.* (2008a) performed several measurements at unitary velocity ratio with two separating walls with different thickness in order to verify the theoretical paper previously cited. The results showed a clear enhancement in the fluctuation level and a synchronization of the whole near field to a frequency which was related to the vortex shedding behind the thickest separating wall, completely absent with the sharp one.

The aim of the present chapter is to investigate the main instabilities which are observable in coaxial jets for different velocity ratios in order to obtain a good knowledge of the main involved dynamics and of the operating parameters which most affect the flow. Hot wire measurements and flow visualization are presented to get a qualitative and quantitative understanding of the flow evolution. The investigation is mainly focused on the dynamics of the inner shear layer which is the responsible of the mixing between the two streams.

More than 1700 pairs (U_i, U_o) have been characterized with the X-wire probe downstream the inner pipe wall at $x/D_i = 0.5$ and $r/D_i = 0.5$ in order to study the observable instabilities. The radial velocity spectra has been calculated for each time history, and the maximum of the spectra has been determined. The frequency of this maximum has been then considered as the one related to the dominant instability at that particular operating condition. Isocontours of all the dominant frequencies have been reported in figure 5.1 where it seems clear that three different regions exist in which these frequencies behave in different ways. At low velocity ratios (namely $r_u < 0.75$) the isocontours are nearly vertical with a small dependence on the outer jet velocity. Between $0.75 \leq r_u \leq 1.6$ the frequencies clearly scale with the average velocity of both jets U_m . For higher velocity ratios the isocontours are almost horizontal which entails a small dependence on the inner jet velocity.

5.2. Low velocity ratio region

The frequency shows a dependence on the inner jet velocity which proves stronger than that on the outer jet velocity, as it was stated above. For $r_u \ll 1$, the inner jet is likely to develop independently as a single jet discharging in a co-flowing stream and, indeed, the main instability frequency scales with the inner jet velocity and with the BL1 momentum thickness θ_i , as stated by Becker & Massaro (1968).

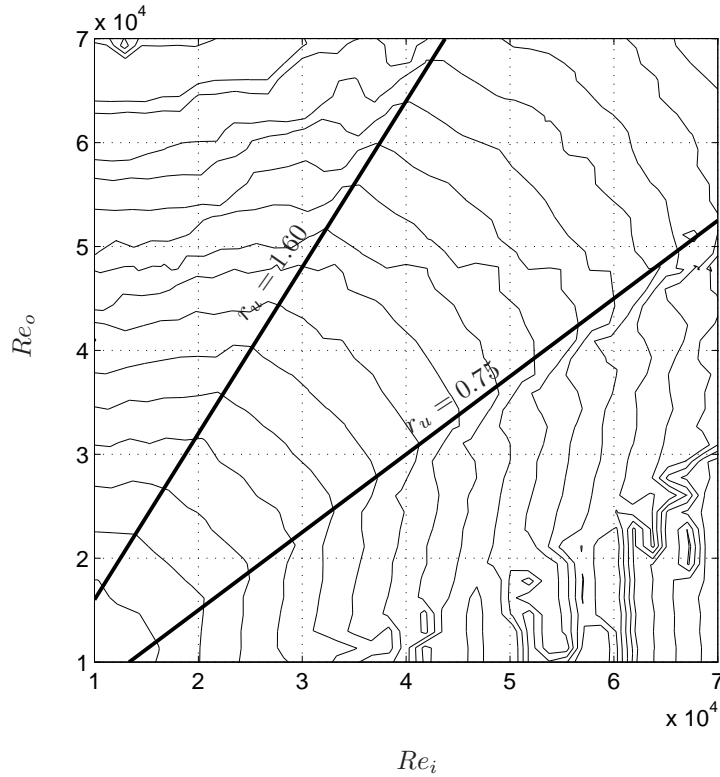


FIGURE 5.1. Isocontours of the maximum peak frequency in the v spectrum.

Figure 5.2 reports the Strouhal number $St_{\theta_i} = f\theta_i/U_i$ for different velocity ratios r_u . In the low velocity ratio region, the dimensionless frequencies tend to collapse towards a constant value St_{θ_i} of about 0.012 which is equal to the one found by Zaman & Hussain (1980) related to the shear layer mode of single jets.

Figure 5.3 reports an instantaneous flow visualization, for a velocity ratio $r_u = 0.2$, in which it is possible to see that both shear layers are developing Kelvin-Helmholtz vortices at two different frequencies, with the inner one higher than the outer one. These two different dynamics can be further appreciated in figure 5.4 where the radial velocity spectra at different radial position have been collected for $r_u = 0.31$. It is evident that both shear layers present broad-band spectral peaks at different frequencies. It is also worth noting that, while the ISL peak scales well in inner variables, on the other hand the OSL peak scales in outer variables (namely the outer jet velocity U_o and BL3 momentum thickness θ_o): a dimensionless frequency $St_{\theta_o} = f\theta_o/U_o$ of approximately

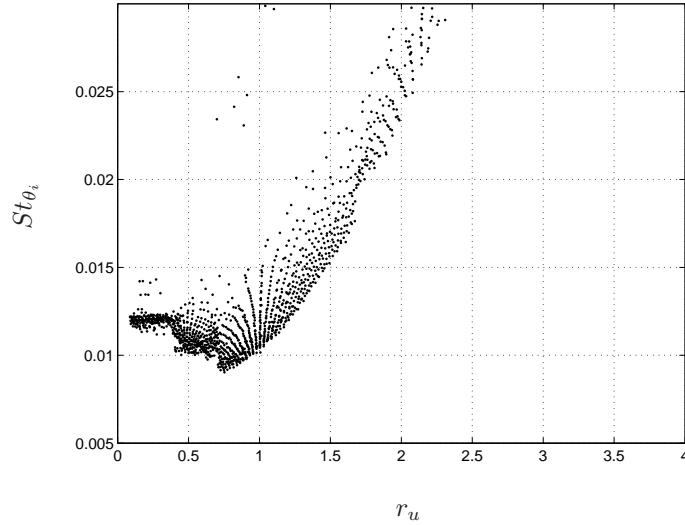


FIGURE 5.2. Strouhal number St_{θ_i} distribution for different r_u .

0.012 is obtained. It is therefore possible to state that, in this low velocity ratio regime, both the inner and outer shear layers develop independently by the presence of each other, with an initial dynamic which proves similar to the single jet case, which is in agreement with the model of Ko & Kwan (1976).

5.3. High velocity ratio region

The main dependence of the dominant frequency on the outer jet velocity for high velocity ratios suggests that the model of Ko & Kwan (1976) is no longer valid and a new scaling is needed. Outer variables will then be chosen for such task, namely U_o and θ_o . Figure 5.5 reports the Strouhal number $St_{\theta_o} = f\theta_o/U_o$ for all the velocity ratios characterized. It is possible to see that, by increasing r_u , there is a convergence of the dimensionless frequency toward St_{θ_o} of about 0.013 which is again close to the shear layer mode described by Zaman & Hussain (1980). It has to be noted that the measurement point was in the middle of the ISL, while the frequency scaled in OSL characteristic variables, which entails a clear coupling between both layers. This property (called lock-in phenomenon) was already found experimentally (Dahm *et al.* 1992) and numerically (da Silva *et al.* 2003) and the same behavior is recovered here.

This fact is stressed again in the flow visualization 5.6 and in the spectral collection 5.7, where a clear synchronization between both layers with a vortex pattern which is typical of shear layers subjected to the Kelvin-Helmholtz instability.

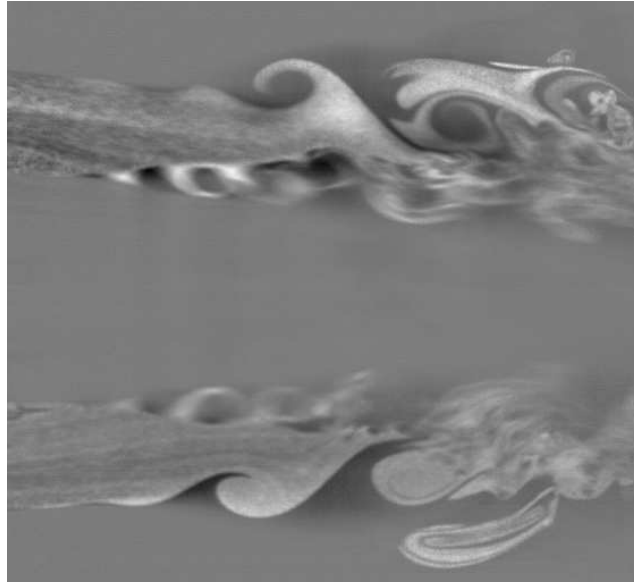


FIGURE 5.3. Instantaneous flow visualization for $r_u = 0.2$ and $Re_i = 34500$.

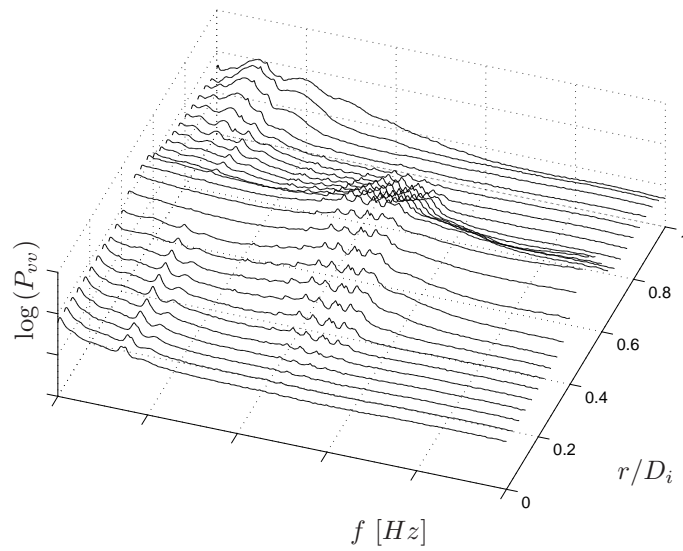


FIGURE 5.4. Radial velocity power density spectra at different radial positions with $x/D_i = 0.5$, $r_u = 0.31$ and $Re_i = 82800$.

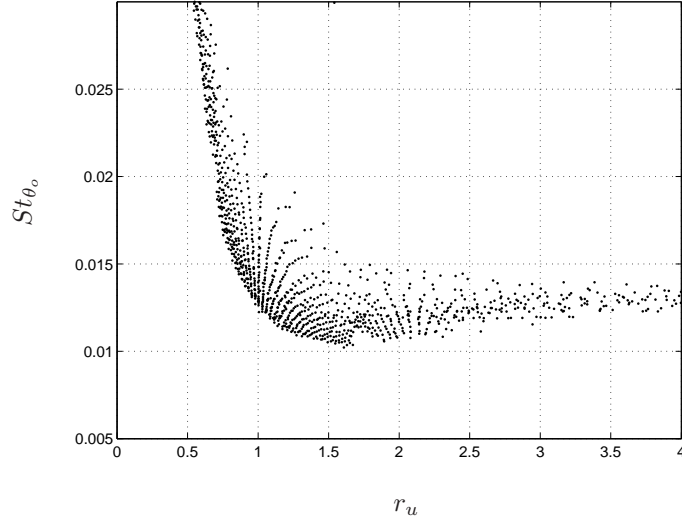


FIGURE 5.5. Strouhal number St_{θ_o} distribution for different r_u .

Heuristically, the velocity shear is almost $|U_o - U_i|/\delta_i$ and U_o/δ_o for the inner and outer shear layer, which are characterized by a typical thickness δ_i and δ_o , respectively. It is likely that $\delta_i \geq \delta_o$, since δ_i is affected by two boundary layers and a wake component. The shear in the OSL is therefore larger than the one in the ISL when $r_u > 0.5$ or even less (depending on the value of δ_i/δ_o). Since the turbulence production term is proportional to the square of the shear (using a constant turbulent viscosity model (Pope 2000)), the ISL fluctuations are higher only in the very near field but later they will be overtaken by the OSL fluctuations which has a higher mean velocity shear. This picture justifies most of the theories which focus in the outer layer as the only efficient way to control the near field dynamics of coaxial jets (da Silva *et al.* 2003)(Angele *et al.* 2006).

5.4. Intermediate velocity ratio region

For velocity ratios near one, the separating wall wake starts playing an important role. As it is evident from the flow visualizations in figure 5.8 at $r_u = 1$, the inner layer Kelvin-Helmholtz vortices are replaced by a more regular Kármán vortex street with a spatial wavelength which proves constant up to the end of the outer jet potential core. According to Buresti *et al.* (1994), the frequency of this shedding phenomenon should scale with the average velocity U_m and with the thickness of the separation edge. A functional form of the vortex shedding frequency f_{vs} can be expressed as:

$$f_{vs} = F(U_i, U_o, D_i, D_o, t, \mu, \rho) \quad (5.1)$$

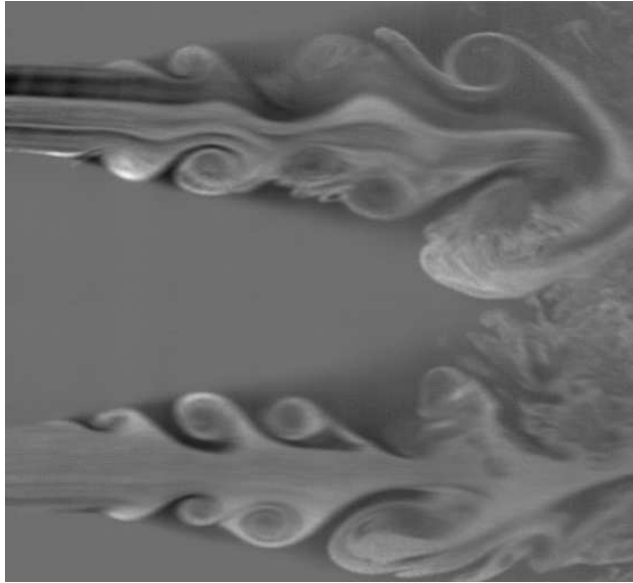


FIGURE 5.6. Instantaneous flow visualization for $r_u = 3.0$ and $Re_i = 6900$.

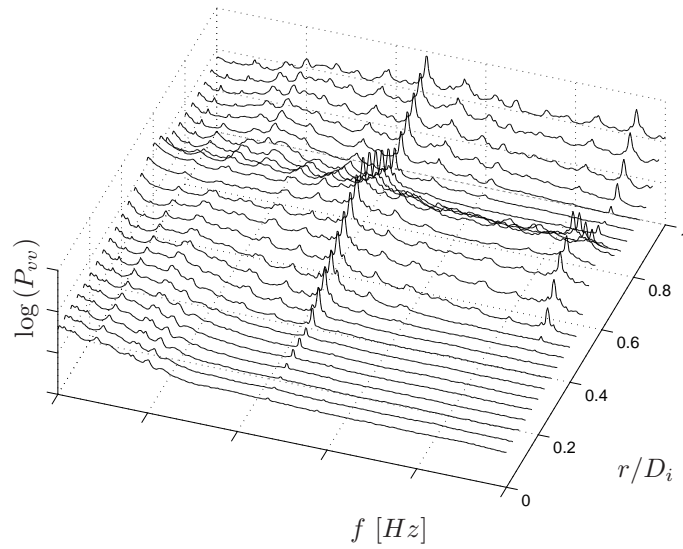


FIGURE 5.7. Radial velocity power density spectra at different radial positions with $x/D_i = 0.5$, $r_u = 4.5$ and $Re_i = 17000$.

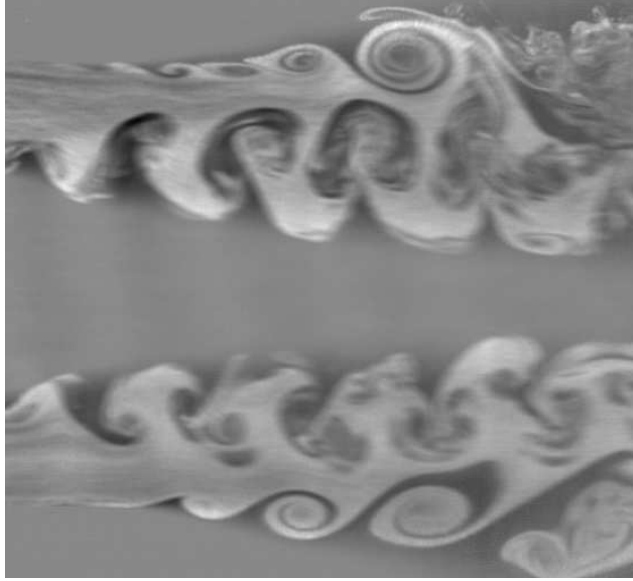


FIGURE 5.8. Instantaneous flow visualization for $r_u = 1.0$ and $Re_i = 13800$.

with a change of variables and the use of Buckingham theorem, equation 5.1 becomes:

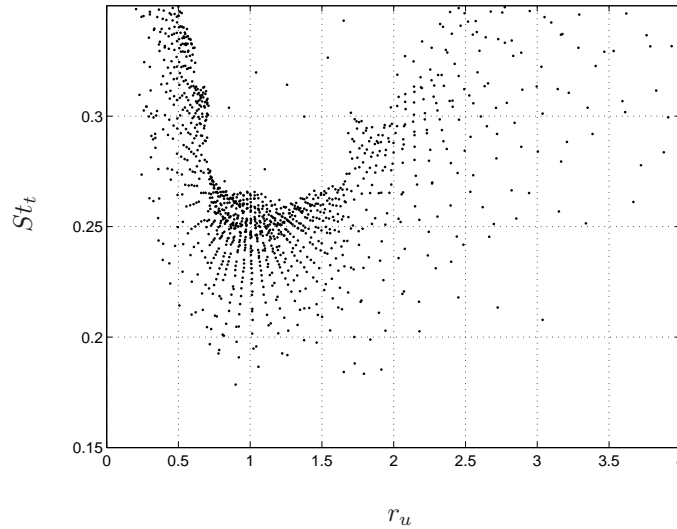
$$f_{vs} = G(r_u, U_m, D_i, D_o, t, \mu, \rho) = \frac{U_m}{t} G' \left(r_u, \frac{D_i}{t}, \frac{D_o}{t}, \frac{U_m t}{\nu} \right) \quad (5.2)$$

since the geometry of this experiment is constant, the geometrical ratios will be removed. This leads to an expression for the Strouhal number St_t :

$$St_t = \frac{f_{vs} t}{U_m} = G'(r_u, Re_m) \quad (5.3)$$

where $Re_m = U_m t / \nu$ is the average Reynolds number which accounts for the viscous effects due to the effects of the separating wall wake.

The collection of all the calculated St_t is reported in figure 5.9. In the intermediate velocity ratio region, the Strouhal numbers are acknowledged to be quite scattered: this shows their clear dependence on the Reynolds number and the velocity ratio as well. Nevertheless, the values of Strouhal number lie in a region near $St_t \approx 0.24$, which is close to the value found by Buresti *et al.* (1994) and Talamelli & Gavarini (2006). The scatter of the present St_t distribution could be mainly due to a wrong choice of the characteristic length scale that should be more closely related to the effective wake width (as Talamelli & Gavarini (2006) and Koch (1985) did).

FIGURE 5.9. Strouhal number St_t distribution for different r_u .

The Reynolds number dependence is highlighted in figure 5.10 where the Strouhal number St_t is reported for several Re_m at nearly unitary velocity ratios. An increasing behavior of the form $St_t \propto Re_m^{1/2}$ of the dimensionless frequency is observed. By looking at figure 5.1, the average velocity U_m is likely to be the correct velocity scale in the intermediate velocity ratio region and, therefore, it is possible to argue that the proper characteristic length scale should be something like $t_x \propto Re^{-1/2}$. Similar arguments follow from Dziomba & Fiedler (1985) where the authors found that the shedding frequency f_{vs} scaled as $U^{3/2}$, suggesting a power relationship similar to the one proposed here. Since the boundary layers BL1 and BL2 are both laminar, their thicknesses scale as $Re^{-1/2}$: this justifies the expression for the proper characteristic length scale:

$$t_x = t + \delta_{1,99} + \delta_{2,99} \quad (5.4)$$

involving the δ_{99} thickness of both boundary layers. This length scale is here chosen because it gives the better collapse of the data as can be appreciated from figures 5.11 and 5.12 where the newly defined Strouhal number $St_{t_x} = f_{vs}t_x/U_m$ is reported as a function of the velocity ratio r_u and of the Reynolds number Re_m , respectively. It is evident that much of the scatter due to Reynolds number effect has been drastically reduced in the intermediate velocity ratio region, while a spurious velocity ratio effect is still present. The concurrence of both wake and mixing layer components suggests such effect to

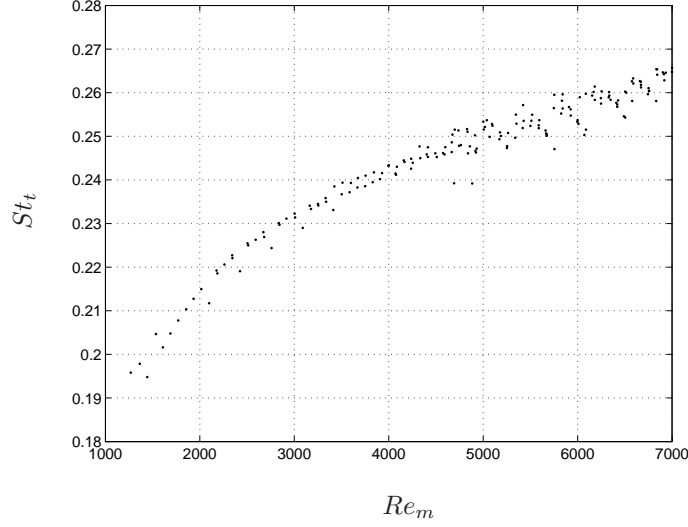


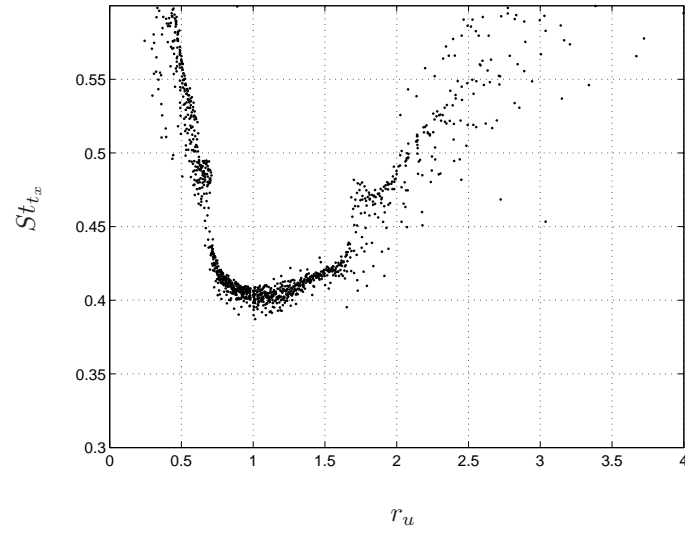
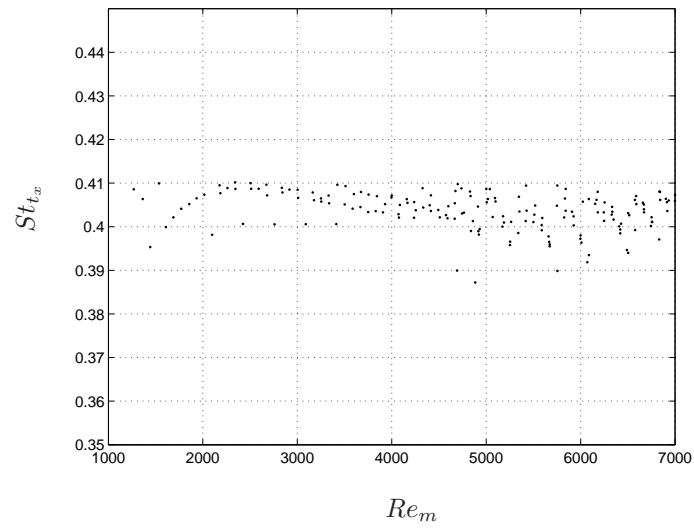
FIGURE 5.10. Strouhal number St_t distribution for different Re_m for $r_u \approx 1$.

be corrected with an empirical quadratic function:

$$H(r_u) = 1 + 0.35 \left(\frac{1}{r_u} - 1 \right)^2 \quad (5.5)$$

Figure 5.13 reports the values of the proper Strouhal number St_{t_x} divided by the function defined in equation 5.5. It can be appreciated that the scaled dimensionless frequency assumes now a constant value of the order of 0.403 over the range $0.75 \leq r_u \leq 1.6$, namely the whole intermediate velocity ratio region. This result clear outlines the link between the frequency of the vortex shedding phenomenon and most of the operating parameters which are involved in the coaxial jets flow.

The of radial velocity spectra collection is reported in figure 5.14 for unitary velocity ratio. In agreement with the flow visualization of figure 5.8, a clear peak in the ISL is present which is due to the wake instability. On the other side, the OSL has a strong peak at the same frequency of the ISL together with several spectral harmonics due to non-linear interactions inside the layer itself. Opposite to the picture described by da Silva *et al.* (2003) for high velocity ratios, in the intermediate r_u region the outer shear layer is forced to follow the dynamics of the inner one, despite the higher shear of the OSL. The presence of the wake of the separating wall creates the conditions for the existence of a wake instability which is self-sustained as demonstrated by Koch (1985).

FIGURE 5.11. Strouhal number St_{t_x} distribution for different r_u .FIGURE 5.12. Strouhal number St_{t_x} distribution for different Re_m for $r_u \approx 1$.

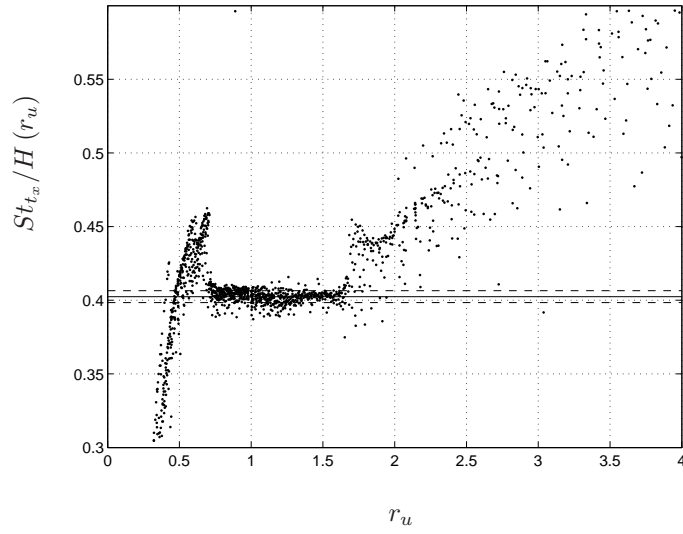


FIGURE 5.13. Scaled Strouhal number $St_{t_x}/H(r_u)$ distribution for different r_u . The solid line is the average value in the range $0.75 \leq r_u \leq 1.6$, while the dashed lines are $\pm 1\%$ variation of the mean value.

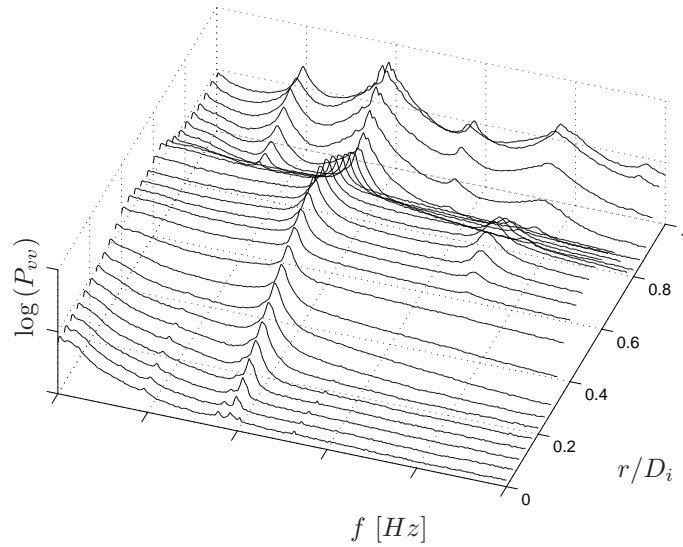


FIGURE 5.14. Radial velocity power density spectra at different radial positions with $x/D_i = 0.5$, $r_u = 1.0$ and $Re_i = 69000$.

CHAPTER 6

Flow and mixing in coaxial jets with different initial conditions

6.1. Generalities

Coaxial jets are a simple way by which two fluid streams can be mixed and this configuration is found for instance in several flows of practical relevance like industrial burners, or wakes of aircrafts turbofan engines. Despite the large amount of practical applications, a lot of research has still to be performed in order to get a clear understanding of this complex flow field.

This chapter will propose the results of some experiments where two different separating wall geometries have been tested in order to investigate the effect of different initial boundary conditions on the flow field, in terms of geometrical boundaries and fluid parameters, as well on the velocity and mixing characteristics. Several velocity ratios have been characterized with this purpose and velocity statistics with the different separating wall geometries will be presented and discussed.

During the experimental campaign, many velocity ratios have been characterized for both separating wall geometries. The full list is reported in table 1 where the Reynolds numbers ($Re = U_\infty D_i / \nu$ where U_∞ is the velocity of the considered jet stream) of both jets are reported. In the followings, only cases (1), (4) and (8) will be analyzed in detail, and the results of all the velocity ratio cases will be used to extrapolate trends of the integral quantities.

In chapter 3 the experimental setup and measurement technique used has been already described. Due to the large amount of data available, the results have been presented in separate sections: the first one focuses on the centerline analysis (section 6.2), followed by the analysis of the velocity and concentration statistics (section 6.3 and 6.4, respectively). More sophisticated analysis are performed through spectral analysis (section 6.5) and conditional sampling technique (section 6.6), while consideration on Reynolds stress and heat fluxes will be reported in section 6.7 together with section 6.8 where the joint probability density functions at some important points will be presented.

Case	r_u	$Re_i \cdot 10^{-3}$	$Re_o \cdot 10^{-3}$
(1)	0.33	79.6	22.8
(2)	0.52	71.8	33.6
(3)	0.96	33.0	28.6
(4)	0.96	66.4	60.0
(5)	1.60	35.3	52.2
(6)	1.96	34.0	62.0
(7)	2.65	27.6	69.0
(8)	3.14	17.1	49.9
(9)	4.30	17.3	70.1

TABLE 1. Operating conditions of all the experiments.

6.2. Centerline analysis

Figures 6.1 and 6.2 report the evolution of the mean and rms of the streamwise velocity and concentration along the inner centerline. For visual aid, the latter quantity has been reported as $1 - \Theta$ to facilitate the direct comparison with the centerline velocity decay. Looking at the mean velocity and concentration component, it is possible to evince that the inner stream mixes with the outer one faster in the thick wall case for all velocity ratios considered as evinced by the faster decay of the mean quantities. Also, as discussed by Buresti *et al.* (1994), the presence of the wake creates a velocity drop in the centerline velocity, clearly visible in the two highest r_u presented, which is felt up to $2 D_i$.

The momentum and concentration length of the potential core (here defined as the region in which mean quantities remain within $\pm 5\%$ of their exit value) is shorter with the thick wall than with the sharp one, underlying the faster mixing of the former geometry. The measured momentum and concentration potential core lengths (x_{pU}/D_i and $x_{p\Theta}/D_i$, respectively) for both geometries and all the studied velocity ratios are reported in figure 6.3 together with the experimental result of Rehab *et al.* (1997), where the authors, investigating flow regimes of coaxial jets at high velocity ratios, proposed on a semi-empirical basis that the potential core length should vary as $x_{pU} \approx ar_u^{-1}$ where a was approximately 8. The collapse of all the points onto a single curve is poor, mainly because the definition of potential core length by means of a common threshold value is arbitrary. However, it is possible to evince the r_u^{-1} trend for high velocity ratios, in agreement with the result of Rehab *et al.* (1997), and a constant potential core length for velocity ratios lower than one.

Downstream the potential core, the mean velocity behaves in two different ways depending on the velocity ratio. For $r_u < 1$ there is the typical decay of the centerline velocity, while for $r_u > 1$ a region where a growth of the inner jet centerline velocity is present due to entrainment of outer jet air with

higher momentum. For all the reported cases, downstream 10 inner diameters the decay toward the fully developed region starts.

The rms profile for the velocity and concentration grows independently of the wall geometry up to $2 D_i$ after which some discrepancies are observed. For $r_u = 0.33$ and $r_u = 0.96$ there is a quick growth of the concentration fluctuation intensity for the thick wall case followed, after 2 inner diameters, by the growth of the fluctuations in the sharp wall case. The $r_u = 3.14$ case does not present the same definite faster growth mainly because the points where u' and θ' start to increase differ just than half an inner diameter from each other.

6.3. Velocity profiles

Figures 6.4 and 6.5 report the mean streamwise velocity profiles U/U_i for both geometries with the three velocity ratios considered here. The first noticeable difference between the two geometries is due to the presence of a large wake component in the velocity profiles measured with the thick separating wall mounted. Besides the velocity defect, a consequence of the thick wake is a bump in the velocity profile close to the boundary layers edge (BL1 and BL2) at the jet exit. When both inner and outer jet velocities get close to each other, the wake becomes significant and the above mentioned aspect become more noticeable. The overshoot in the velocity profile is probably accentuated by the thick trailing edge which generates a clear separating region and, consequently, a local acceleration of the flow close to the side boundary layers. This phenomenon is connected to the drop in velocity observed in the inner jet centerline (figure 6.1) and is almost absent in the sharp wall case.

In agreement with the flow description given in the introduction, all the velocity profiles show the presence of two potential cores, of the inner and outer shear layer, separating the inner from the outer stream and the outer stream from the external field at rest, respectively. The outer momentum potential core length is between 2 and 3 inner diameters with a weak dependence on the operating parameters.

The dynamics of the inner and outer shear layers are of great interest in this analysis. The ISL changes dramatically due to the wake of the separating wall, while the OSL seems to be only slightly affected by the different initial conditions. The presence of a wake embedded in a shear layer is a critical point which complicates further the flow dynamics. The complex interactions of wake-mixing layer was discussed by several authors, e.g. Boldman *et al.* (1976), Wallace & Redekopp (1992), Mehta (1991*b*) and Braud *et al.* (2004), where they all point out that a competition between the wake-like and the mixing layer-like behavior have place. The velocity defect in the U/U_i profile is a parameter that discerns whether or not the wake is still present. All investigated velocity ratios show wake traces immediately at the exit but,

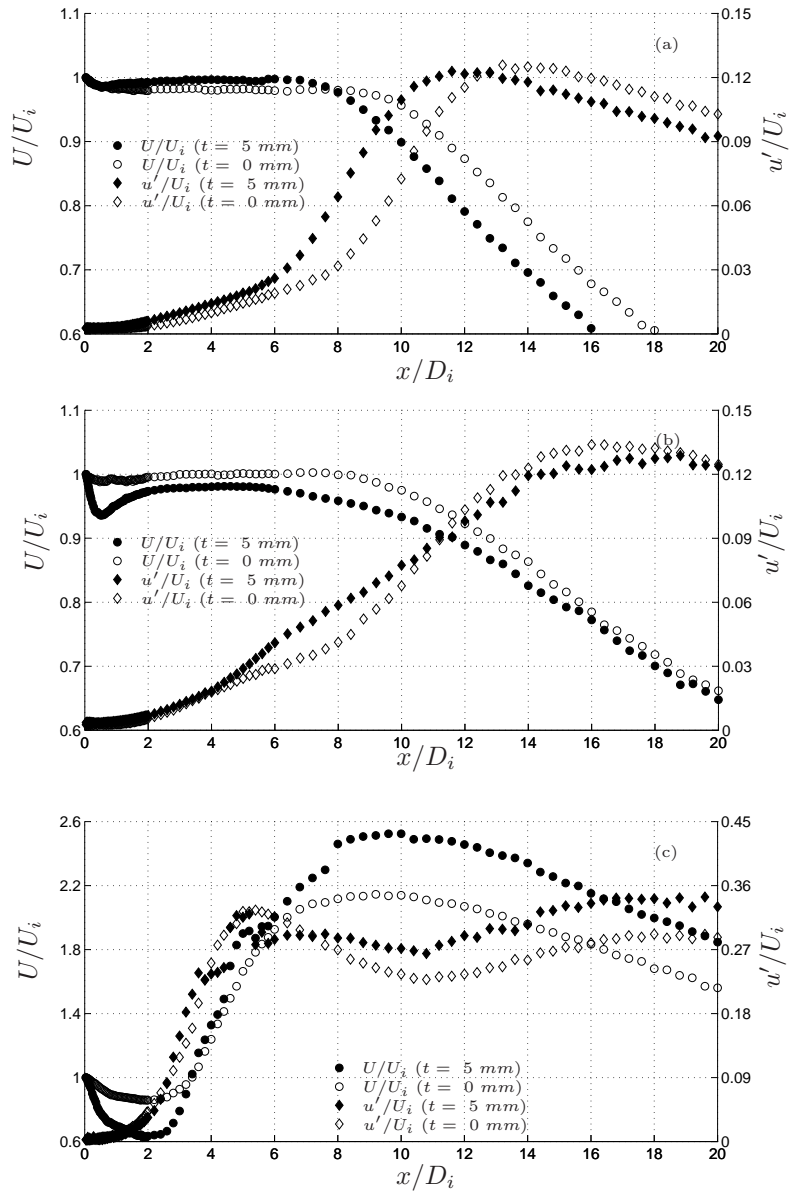


FIGURE 6.1. Mean and rms velocity along the inner jet centerline for (a) $r_u = 0.33$, (b) $r_u = 0.96$, (c) $r_u = 3.14$.

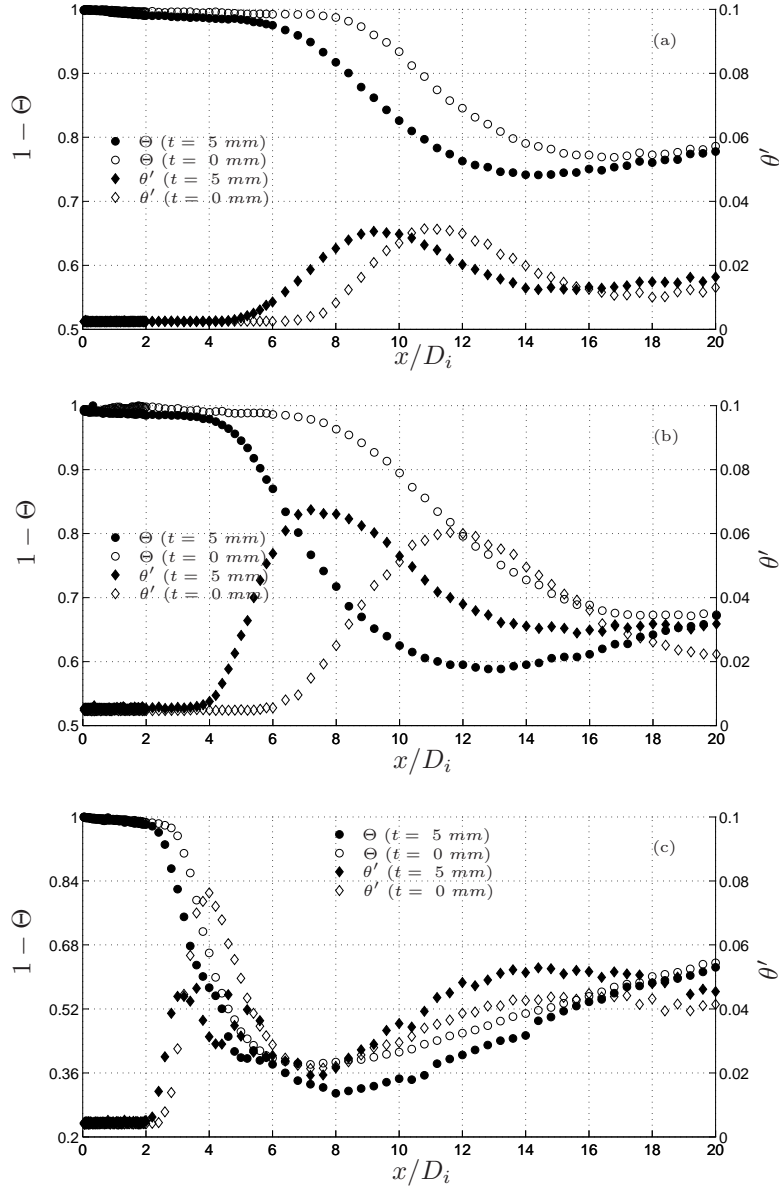


FIGURE 6.2. Mean and rms concentration along the inner jet centerline for (a) $r_u = 0.33$, (b) $r_u = 0.96$, (c) $r_u = 3.14$.

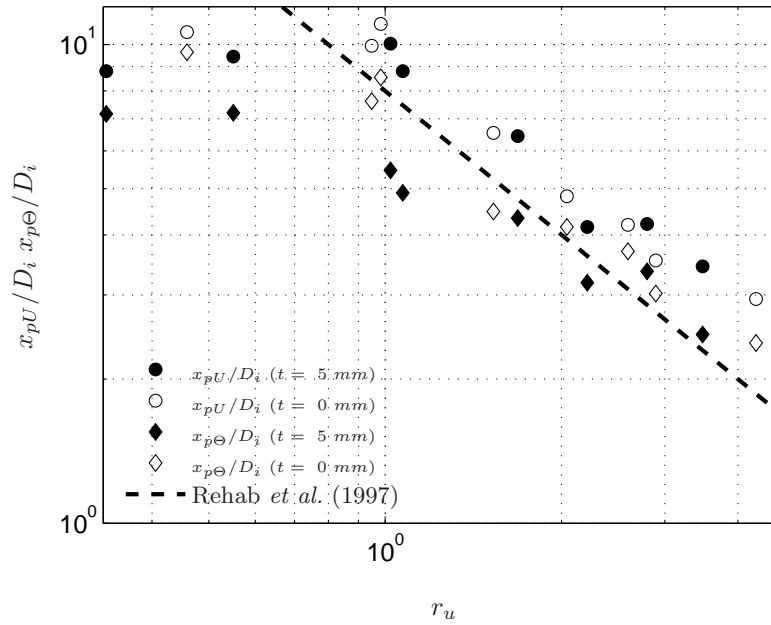


FIGURE 6.3. Inner jet potential core lengths x_{pU}/D_i and x_{pT}/D_i for all velocity ratios and geometries considered here.

Case	Thick wall			Sharp wall	
	r_u	x_{0U}/D_i	$\frac{dL_U}{dx}$	x_{0U}/D_i	$\frac{dL_U}{dx}$
(1)	0.33	0.39	0.243	0.37	0.200
(2)	0.52	0.54	0.231	0.41	0.215
(3)	0.96	0.24	0.202	0.61	0.220
(4)	0.96	0.18	0.177	0.42	0.182
(5)	1.60	0.36	0.210	0.46	0.189
(6)	1.96	0.18	0.175	0.42	0.174
(7)	2.65	0.21	0.176	0.25	0.170
(8)	3.14	0.31	0.180	0.60	0.194
(9)	4.30	0.27	0.192	0.28	0.174

TABLE 2. Streamwise velocity spreading rate parameters of the outer shear layer.

after a certain while, they vanish due to transport mechanisms. The length of the region where the wake is observable is clearly a function of the initial conditions and finds its maximum for unitary velocity ratio and a thick wall geometry. However, for $r_u \gg 1$, the wake seems to disappear after the first inner diameter, and is replaced by a shear layer, independently of the geometry of the separation wall.

It is possible to evince from the mean velocity profiles that the tails of the thick wall ISL and OSL are smoother with moderate velocity ratios suggesting a higher mixing velocity than the corresponding sharp wall shear layers. Table 2 reports the virtual origins and spreading rates of the outer shear layer for all the investigated cases. Both quantities are estimated by means of linear fitting of the distribution $L_U(x) = |r_{0.2} - r_{0.8}|$ where r_p is the radial location where $U(r_p) = p * U_o$. The main outcome of this table is that the presence of the thick wall accelerates the evolution of the outer mixing layer, increasing the spreading rate or decreasing the virtual origin (often both effects), making the x-momentum spreading between the outer stream and the ambient air faster.

To add some insight in the coaxial jets dynamics, streamwise velocity rms profiles, at various downstream stations, are reported in figures 6.6 and 6.7. It is immediately apparent that the two shear layers are characterized by a higher fluctuation level than the surroundings. They are clearly segregated until around $3 D_i$ where the outer potential core ends, and then the merging of both layers initiates. Between the jets exit and this x-position, the outer shear layer fluctuations continuously grows, reaching their maximum at around $3 D_i$. The ISL is initially affected by the separating plate for all geometries and, indeed, its transition towards a fully turbulent state is triggered by the

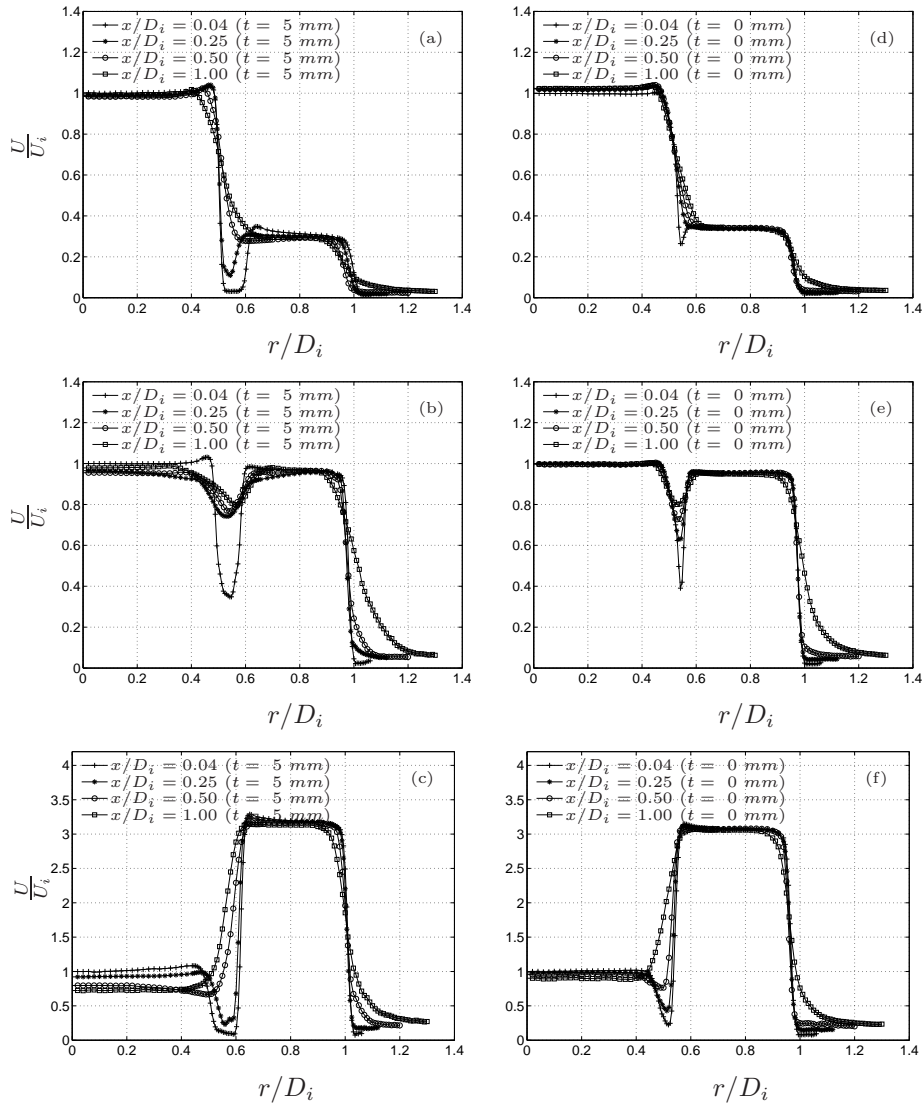


FIGURE 6.4. Mean streamwise velocity profiles for (a,d) $r_u = 0.33$, (b,e) $r_u = 0.96$, (c,f) $r_u = 3.14$ with the (a,b,c) thick and (d,e,f) sharp wall for $x/D_i = 0.04, 0.25, 0.50, 1.0$.

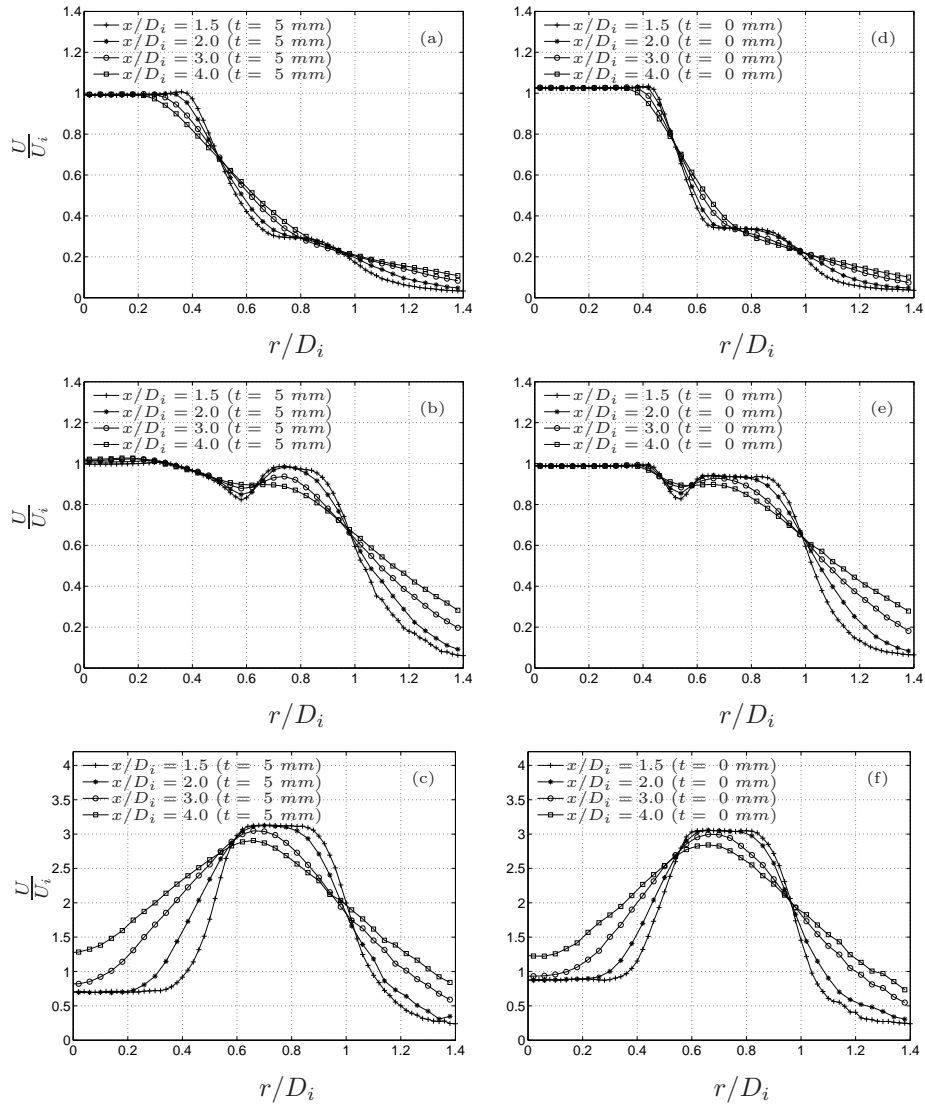


FIGURE 6.5. Mean streamwise velocity profiles for (a,d) $r_u = 0.33$, (b,e) $r_u = 0.96$, (c,f) $r_u = 3.14$ with the (a,b,c) thick and (d,e,f) sharp wall for $x/D_i = 1.5, 2.0, 3.0, 4.0$.

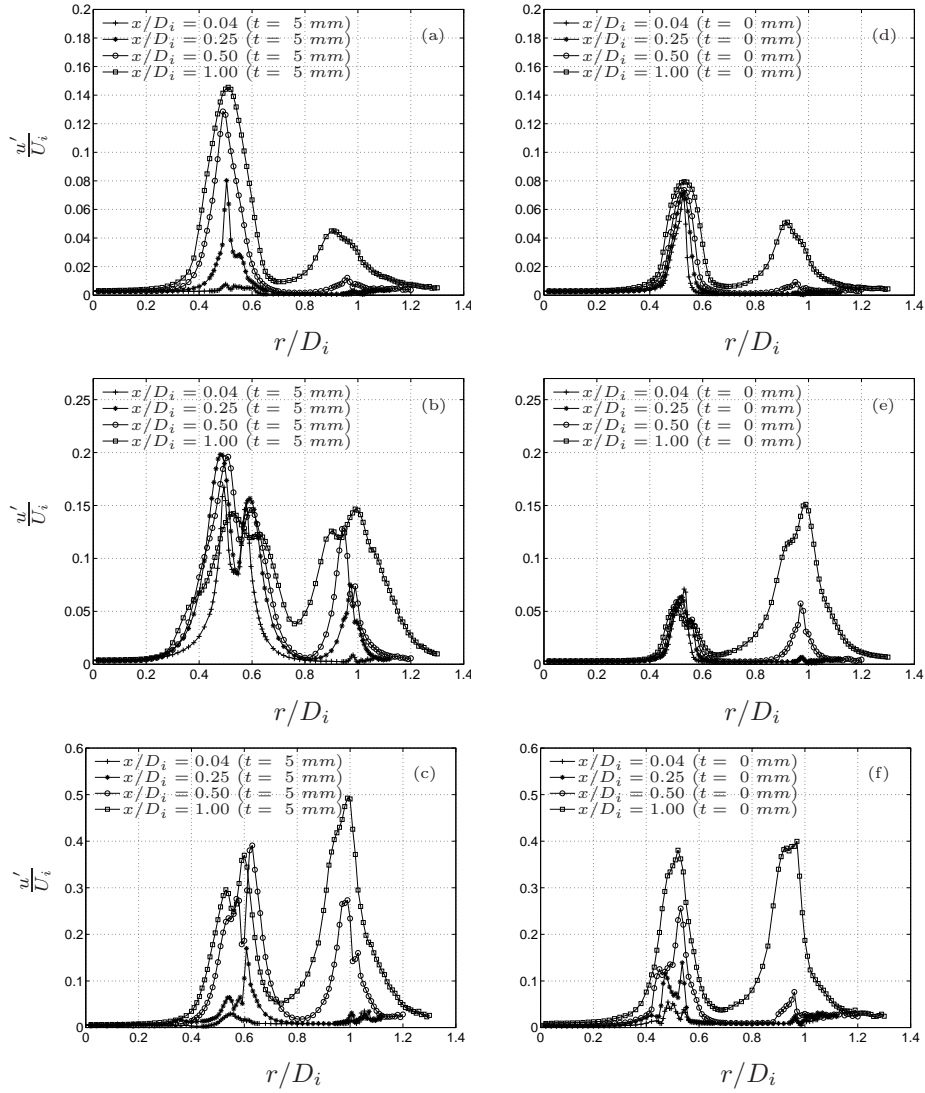


FIGURE 6.6. Streamwise velocity rms profiles for (a,d) $r_u = 0.33$, (b,e) $r_u = 0.96$, (c,f) $r_u = 3.14$ with the (a,b,c) thick and (d,e,f) sharp wall for $x/D_i = 0.04, 0.25, 0.50, 1.0$.

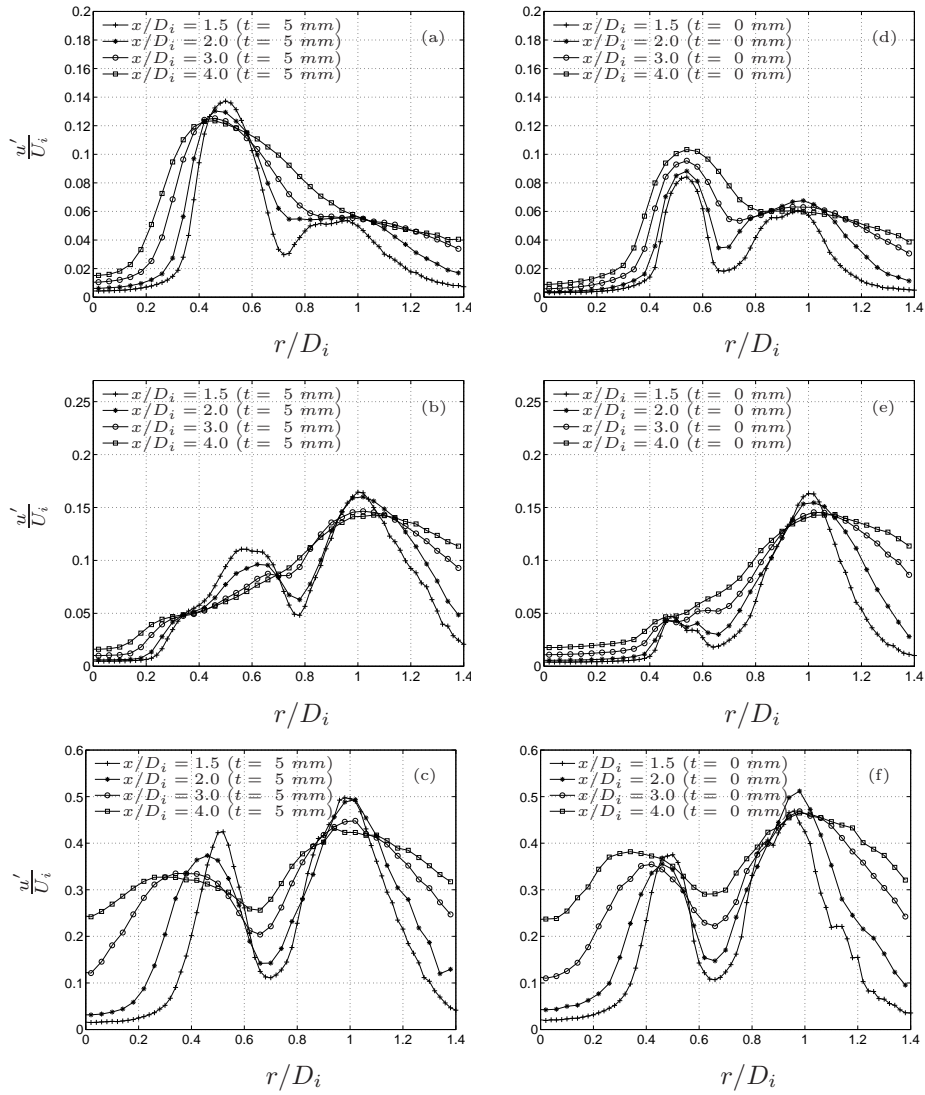


FIGURE 6.7. Streamwise velocity rms profiles for (a,d) $r_u = 0.33$, (b,e) $r_u = 0.96$, (c,f) $r_u = 3.14$ with the (a,b,c) thick and (d,e,f) sharp wall for $x/D_i = 1.5, 2.0, 3.0, 4.0$.

wake. Further downstream, due to the mean velocity shear, the turbulence production term increases and, consequently, the velocity fluctuations. Heuristically, the production term is proportional to the square of the velocity shear (using a constant turbulent viscosity model (Pope 2000)) which is of the order of $|U_o - U_i|/\delta_i$ and U_o/δ_o for the inner and outer shear layer, characterized by a typical thickness δ_i and δ_o , respectively, where it is likely that $\delta_i \geq \delta_o$ since δ_i is affected by two boundary layers and a wake component. The above arguments imply that the shear in the OSL is larger than the one in the ISL when $r_u > 0.5$ or even less (depending on the value of δ_i/δ_o). Since the production term is proportional to the square of the shear, the ISL fluctuations are higher only in the very near field but later they will be overtaken by the OSL fluctuations which has a higher mean velocity shear. This picture justifies most of the theories which focus in the outer layer as the only efficient way to control the near field dynamics of coaxial jets (da Silva *et al.* 2003)(Angele *et al.* 2006).

Here the inner shear layer is by far the most fluctuating in the near field for nearly unitary velocity ratios and with a thick wall mounted. Further downstream the differences due to different geometries decrease even if a clear footprint of the increased initial level is still recognizable. The OSL, being a convectively unstable mixing layer, acts as a noise amplifier and shows therefore higher fluctuation intensities in the thick wall case. It has to be considered that with a higher fluctuation level, there is a higher turbulent diffusion, the thickness of the layer will increase too, decreasing consequently the shear rate and, indeed, the production term. From the measurements it seems that the OSL is mostly unaffected by the separating wall for low r_u , while for intermediate and high velocity ratios there is an increase in the initial rms level but then the differences will smooth out within the first inner diameter.

6.4. Concentration profiles

The mean concentration evolution at different downstream stations is reported in figures 6.8-6.9. Although the initial concentration profile is not very close to a top hat distribution, due to heat conduction across the settling chamber of both jets, the conclusions regarding the mixing evolution will be only partially affected by this and, anyway, the comparison between the different separating wall geometries, in order to determine which one improves the mixing, can still be performed.

The issue of the length of the inner potential core has been introduced in section 6.2 and several aspects will be furthermore discussed here. The inner concentration core is shortened by the thick wall for low and intermediate r_u , but becomes less discernible by increasing the velocity ratio. The outer potential core length is almost constant and equal to 1.5 inner diameters regardless of the initial conditions and velocity ratios.

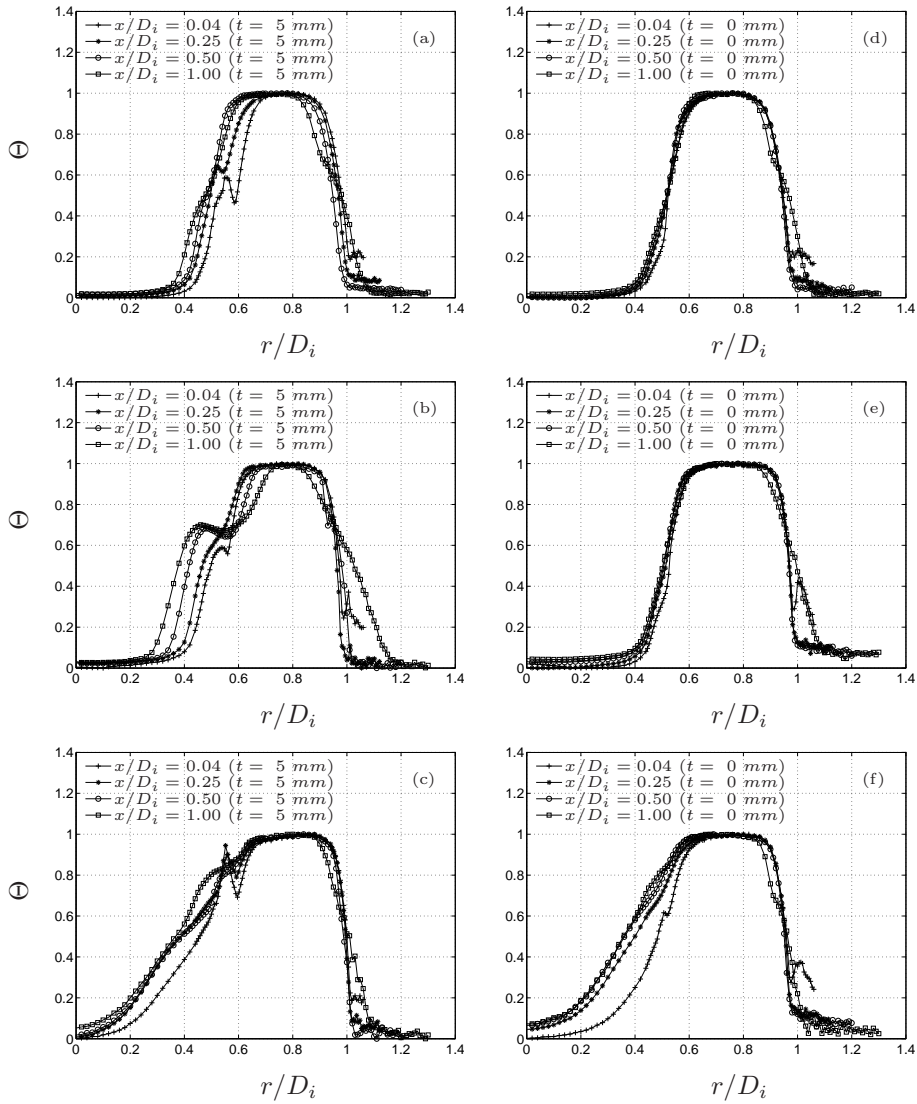


FIGURE 6.8. Mean concentration profiles for (a,d) $r_u = 0.33$, (b,e) $r_u = 0.96$, (c,f) $r_u = 3.14$ with the (a,b,c) thick and (d,e,f) sharp wall for $x/D_i = 0.04, 0.25, 0.50, 1.0$.

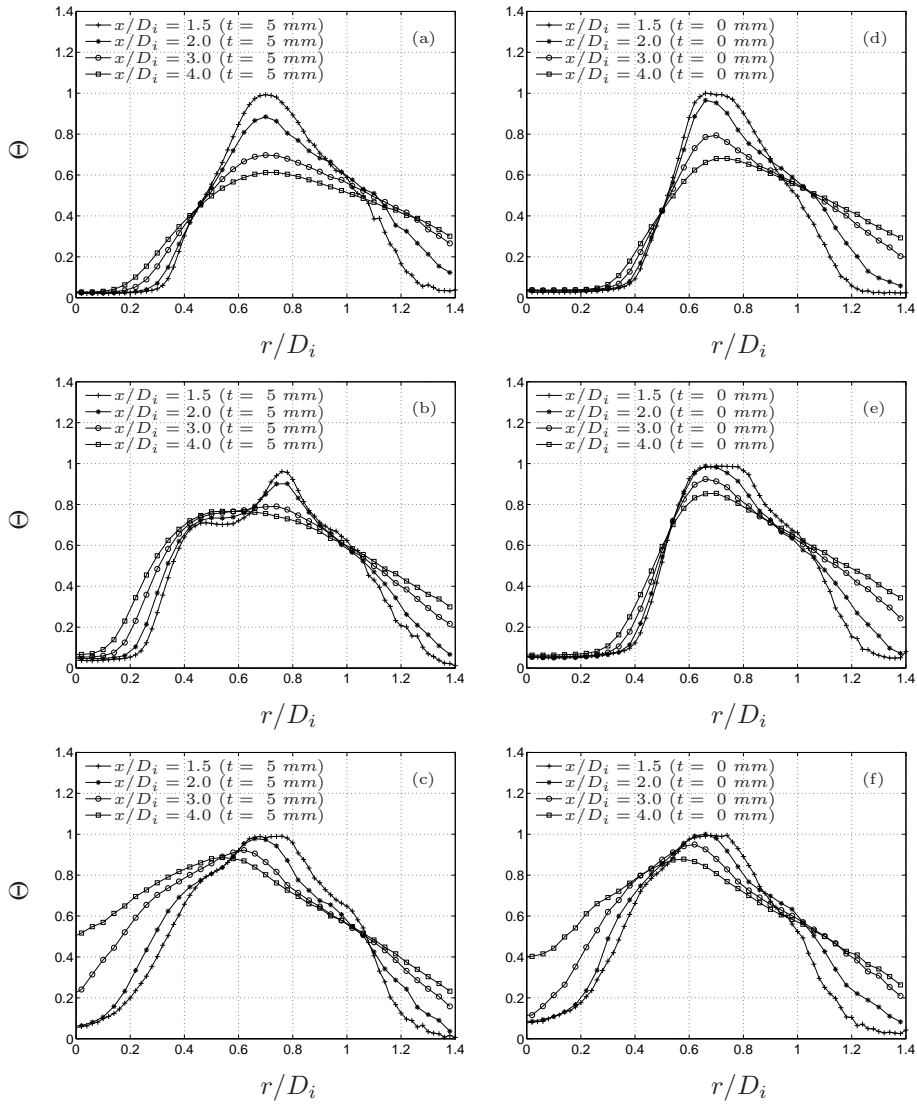


FIGURE 6.9. Mean concentration profiles for (a,d) $r_u = 0.33$, (b,e) $r_u = 0.96$, (c,f) $r_u = 3.14$ with the (a,b,c) thick and (d,e,f) sharp wall for $x/D_i = 1.5, 2.0, 3.0, 4.0$.

Tables 3 and 4 report the spreading rate of both shear layers evaluated by means of the concentration profiles. Here the spreading rate is estimated by means of linear fitting of the distribution $L_{\Theta}(x) = |r_{0.2} - r_{0.8}|$ where r_p is the radial location where $\Theta(r_p) = p$. It is again evident that the thick wall geometry is associated with a faster mixing for both layers in their early stages of evolution. In the OSL the origin is always positive due to the slow development of the layer while in the ISL the virtual origin is most of the time negative with a low spreading rate, meaning that the layer is thick from the very beginning, being strongly affected by the wake of the lip together with boundary layers BL1 and BL2.

The concentration rms profiles in figures 6.10 and 6.11 underline again some aspects mentioned in section 6.3. The fluctuation level is a strong function of the velocity ratio r_u and of the initial conditions. In the ISL region, in particular, the fluctuations are enhanced when the thick separating wall is on. This is the case immediately at the jet exit and in the very near field region, while the differences due to the initial conditions decrease going downstream for velocity ratios which depart from the unitary value. The $r_u = 0.96$ case exhibits a higher θ' in the inner layer with the thick wall even at $x/D_i = 4$. A conjecture which explains this high level of fluctuation is that strong vortices are shed from the separating wall, each one containing a large amount of hot/cold unmixed fluid. Going downstream, these vortices start to be stretched and deformed by turbulent motions, becoming more and more suitable to mix with the neighboring fluid (Meunier & Villermaux 2003). This picture agrees well with the observations at unitary velocity ratio of Buresti *et al.* (1994) and Örlü *et al.* (2008a). No considerations can be formulated for the early stages of the outer region because of the low local velocity value which affects the accuracy of the cold-wire. However, it seems that the thick wall θ' behaves as u' with an high level at the beginning followed by a convergence with the sharp wall θ' distribution downstream the end of the outer potential core. The increased growth rate is observed mostly in the low and intermediate velocity ratio, while for the highest one reported here, the high shear in OSL soon overwhelm the process due to perturbations coming from inner layer, starting to be the strong enough to dominate the flow dynamics (Dahm *et al.* 1992).

6.5. Spectral analysis

Figure 6.12 reports the radial velocity power density spectra at $x/D_i = 0.5$ downstream the nozzles exit at $r/D_i = 0.5$ and $r/D_i = 1.0$ in order to be inside the inner and outer shear layer, respectively. It is possible to observe that there is a clear effect of both velocity ratio and initial conditions, especially in the ISL which is the most affected by the change in geometry. For $r_u = 0.33$ with the sharp wall the maximum of the spectra is near a frequency of 1500 Hz and a strong peak at the same frequency is found for the thick wall as well.

Case	Thick wall			Sharp wall	
	r_u	$x_{0\Theta}/D_i$	$\frac{dL_\Theta}{dx}$	$x_{0\Theta}/D_i$	$\frac{dL_\Theta}{dx}$
(1)	0.33	-1.28	0.074	0.07	0.180
(2)	0.52	-3.12	0.041	-4.32	0.023
(3)	0.96	-1.35	0.147	-4.27	0.031
(4)	0.96	-1.97	0.097	-1.00	0.063
(5)	1.60	-1.30	0.087	-3.45	0.033
(6)	1.96	-0.57	0.162	-1.27	0.067
(7)	2.65	-0.85	0.088	-1.74	0.055
(8)	3.14	23.2	-0.014	-10.2	0.025
(9)	4.30	-10.1	0.031	-19.3	0.011

TABLE 3. Concentration spreading rate parameters of the inner shear layer.

Case	Thick wall			Sharp wall	
	r_u	$x_{0\Theta}/D_i$	$\frac{dL_\Theta}{dx}$	$x_{0\Theta}/D_i$	$\frac{dL_\Theta}{dx}$
(1)	0.33	0.22	0.281	0.16	0.210
(2)	0.52	0.21	0.232	0.21	0.230
(3)	0.96	0.21	0.257	0.21	0.209
(4)	0.96	0.11	0.239	0.26	0.238
(5)	1.60	0.24	0.251	0.23	0.226
(6)	1.96	0.17	0.288	0.24	0.230
(7)	2.65	0.30	0.275	0.47	0.363
(8)	3.14	0.14	0.216	0.21	0.229
(9)	4.30	0.13	0.297	0.24	0.220

TABLE 4. Concentration spreading rate parameters of the outer shear layer.

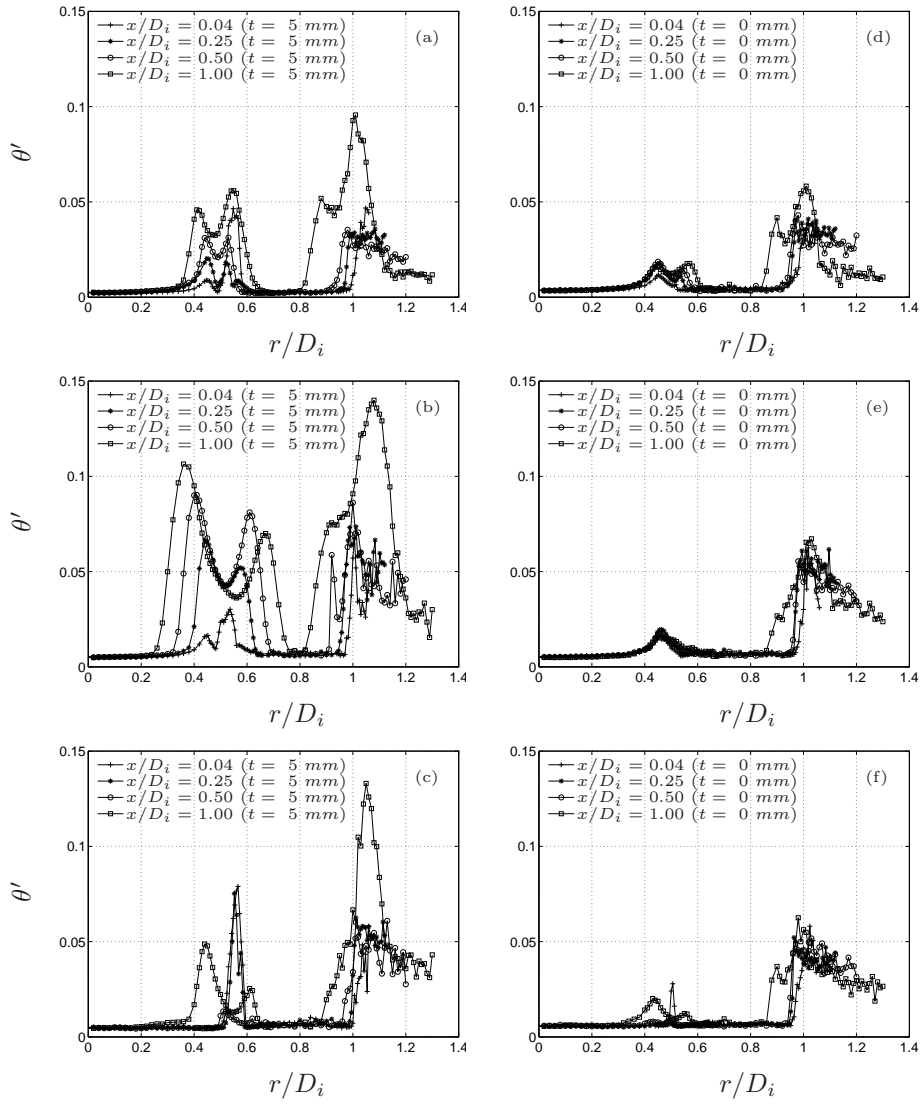


FIGURE 6.10. Concentration rms profiles for (a,d) $r_u = 0.33$, (b,e) $r_u = 0.96$, (c,f) $r_u = 3.14$ with the (a,b,c) thick and (d,e,f) sharp wall for $x/D_i = 0.04, 0.25, 0.50, 1.0$.

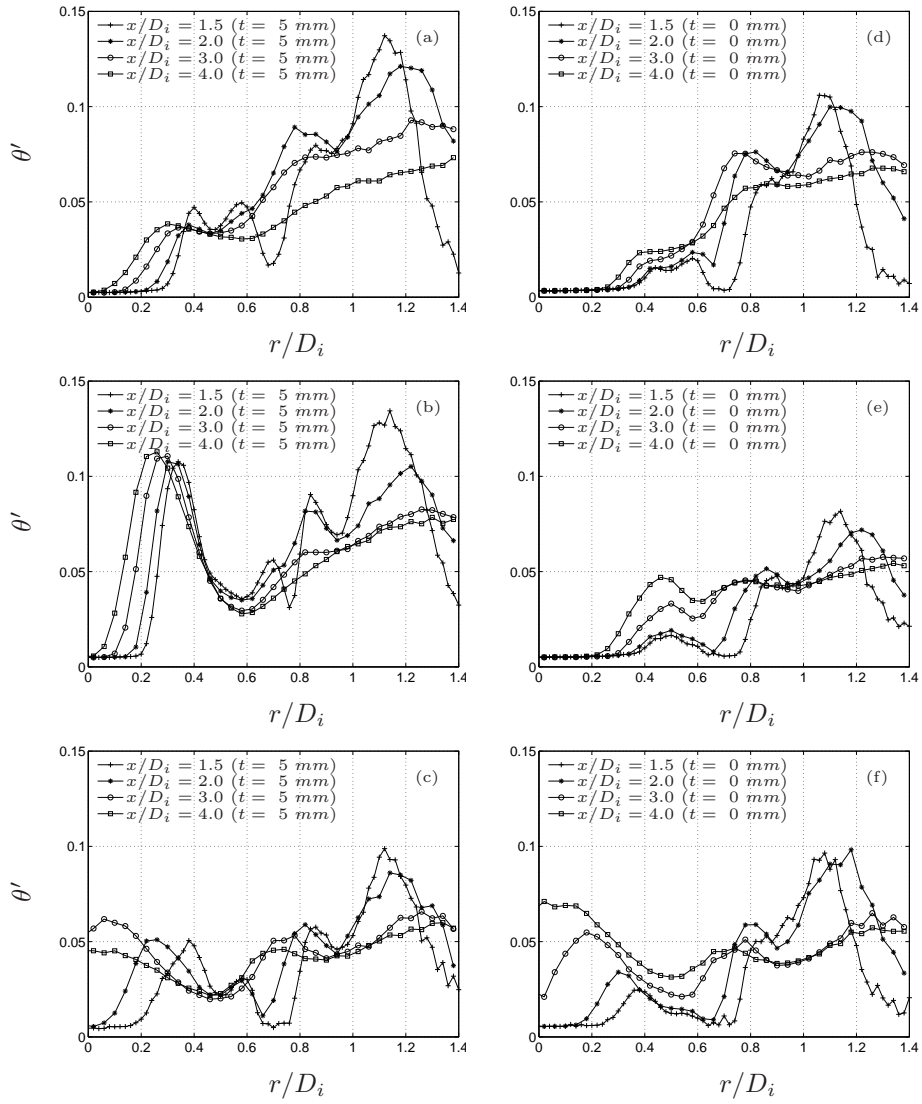


FIGURE 6.11. Concentration rms profiles for (a,d) $r_u = 0.33$, (b,e) $r_u = 0.96$, (c,f) $r_u = 3.14$ with the (a,b,c) thick and (d,e,f) sharp wall for $x/D_i = 1.5, 2.0, 3.0, 4.0$.

This frequency, if scaled with the inner jet velocity and the innermost boundary layer momentum thickness θ_1 , gives a Strouhal number, $St_{\theta_1} = f\theta_1/U_i$, or around 0.012 which is in agreement with the results of Zaman & Hussain (1980) on the shear layer mode of single jets. Indeed, the observed peak is only due to the Kelvin-Helmholtz instability of the ISL as will be discussed in paper 2. Despite the presence of a stronger peak, the OSL spectra does not qualitatively change, even if more energy is distributed at low frequencies in the thick wall case due to the excitation mechanisms explained in section 6.3.

For $r_u = 0.96$ a very strong peak, with several harmonics, appears on the ISL spectra with the thick wall. This particular velocity pair $(U_i, U_o) = (20, 20)$ has been chosen because of the matching of vortex shedding frequency f_{vs} , estimated with the relationship proposed by Buresti *et al.* (1994), with OSL Kelvin-Helmholtz instability to identify the strongest mechanism and whether a competition is present or not. The OSL presents for both geometries the same 1 *kHz* peak that, at the control point, is not yet strong enough to influence the ISL with the sharp wall. With the thick wall, instead, both layers are clearly excited by the shedding frequency which now drives the whole near field dynamics. This is a clear evidence of the reversed lock-in phenomenon discussed by Örlü *et al.* (2008*a*), namely a situation in which the inner layer dominates the dynamics of the outer one, opposite to the common locking phenomenon, where the OSL dominates the ISL dynamics (da Silva *et al.* 2003).

For high velocity ratios, both the inner and outer shear layer are still more fluctuating with the thick wall presenting a clear peak at the same frequency which scales only in outer variables, suggesting the dominance of the outer shear layer in the near field. Even if the wake instability is not anymore the dominant source of velocity fluctuations, its presence increases slightly the initial turbulence and, consequently, the power spectral density at the control point.

Figures 6.13 and 6.14 show the evolution for different downstream stations at $r/D_i = 0.5$ and $r/D_i = 1$ of the radial velocity spectra. Again the presence of the thick wall creates the conditions for the presence of spectral peaks which are observed up to three inner diameters downstream. For $r_u = 0.96$ the inner layer peak remains locked to the vortex shedding frequency while the outer peaks are strongly affected by the shedding effects at the beginning and then at $x/D_i = 0.5$ there is the development of the subharmonic frequency, which will dominate the outer dynamics further downstream. Some peaks are recognizable with the sharp wall too, but they are broad-band, not so clear to recognize and, over all, they change their associated frequency going downstream due to the combined effect of the Kelvin-Helmholtz instability and of the thickening of the outer layer where pairing mechanisms between vortices take place.

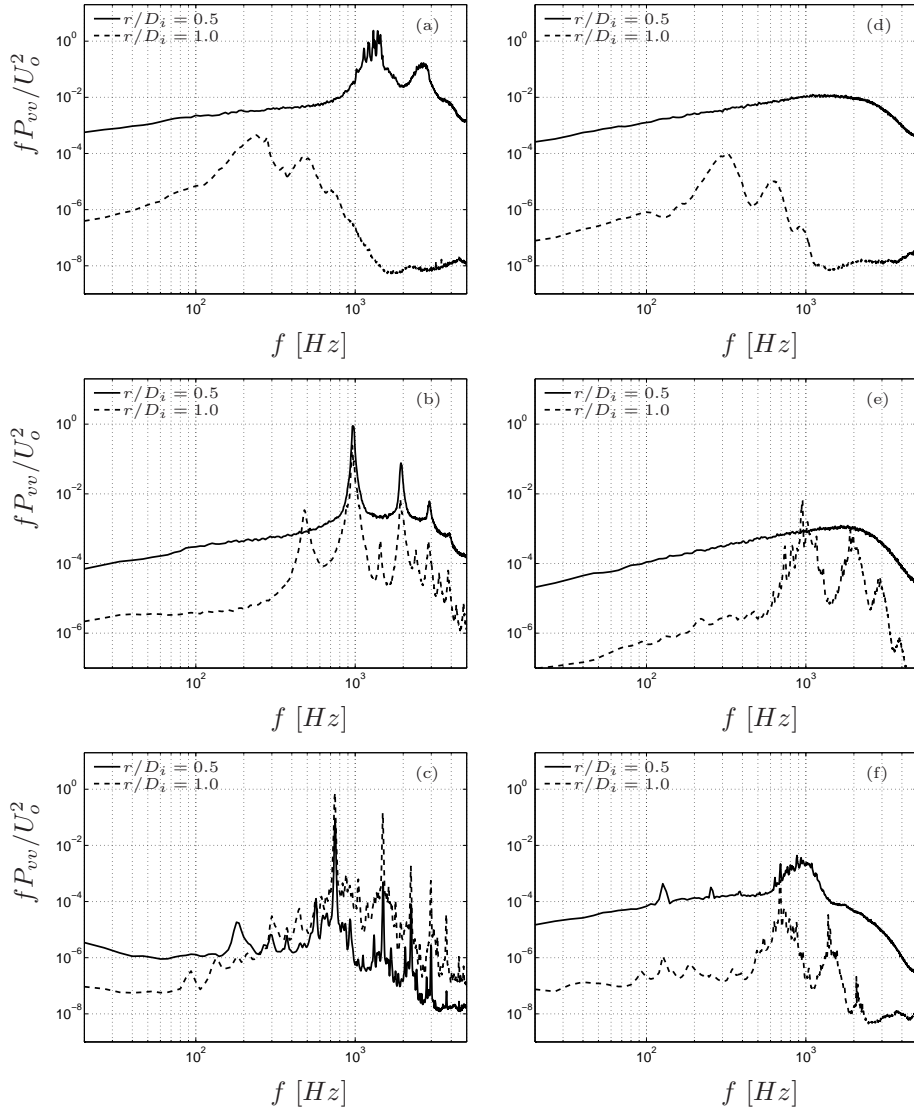


FIGURE 6.12. Dimensionless radial velocity spectra at $x/D_i = 0.5$ for (a,d) $r_u = 0.33$, (b,e) $r_u = 0.96$, (c,f) $r_u = 3.14$ with the (a,b,c) thick and (d,e,f) sharp wall.

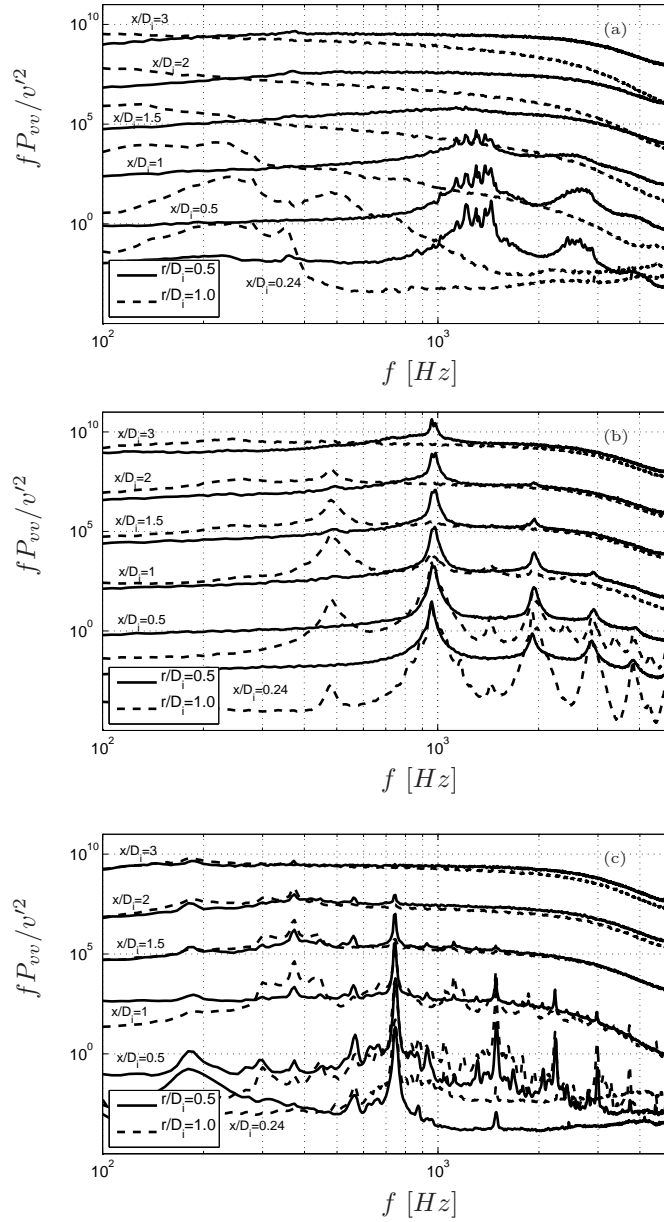


FIGURE 6.13. Dimensionless radial velocity spectra at various downstream stations for (a) $r_u = 0.33$, (b) $r_u = 0.96$, (c) $r_u = 3.14$ with the thick wall.

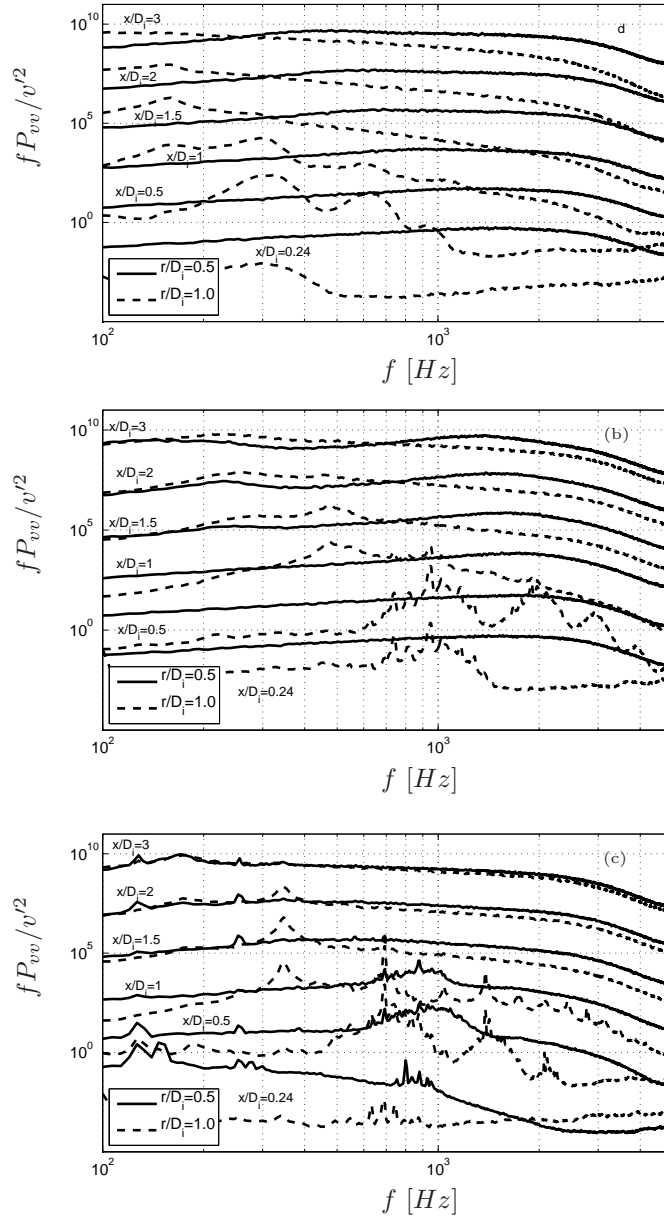


FIGURE 6.14. Dimensionless radial velocity spectra at various downstream stations for (a) $r_u = 0.33$, (b) $r_u = 0.96$, (c) $r_u = 3.14$ with the sharp wall.

6.6. Conditional sampling analysis

As underlined in the previous paragraph, when the separating wall is thick the velocity spectra changes its behavior and several spectral peaks appear. These peaks contains a large part of the whole fluctuating energy and so they need a much more detailed description. Physically, it is possible to evince that these spectral peaks are related to some organized vortex motions which are triggered by an instability present in the flow field. From different flow visualizations (Dahm *et al.* 1992) and numerical simulations (Balarac & Métais 2005), it appeared that these structures are initially rings or helices, with an high azimuthal coherence. By placing a SW probe in a proper radial position a triggering signal was obtained and conditional sampling methods applied to the signal from the main probe. The triggering event has been defined in section 3.2 according to the procedure applied by Zaman & Hussain (1984). By assuming that these structures are rings or helices, it is possible to characterize the flow induced by these structures alone, obtaining a description of their size and of the induced flow dynamics, by means of the conditionally sampled measurements.

Figures 6.15 and 6.16 report the conditionally sampled radial velocity fields with the thick wall for $r_u = 0.96$ and $r_u = 3.14$, respectively, where the abscissa is time multiplied by the dominant frequency f_x estimated from the maximum of the velocity spectra. The lowest velocity ratio and the sharp wall related images are not presented because they are much more affected by the jittering effect and the structures are not so clearly detectable.

Figure 6.15 shows that the vortex dynamics are quite complex. Initially, the shear layers originating from BL1 and BL2 interact creating a sort of staggered structure sequence close to the typical vortex pattern in the wake of a bluff body (Van Dyke 1982). In this case, the thickness of the separating wall creates favorable conditions for the formation of these kind of structures related to the wake instability of the velocity profile (Talamelli & Gavarini 2006). Simultaneously, the outer shear layer, which usually should follow the well know dynamics of mixing layers, is forced at a frequency equal to the passage frequency of the inner vortices, as already observed in the velocity power spectral density.

Going further downstream, the inner regions has still the same periodicity while the outer one develops subharmonic structures, due to the pairing interactions. It is important to note that the outer structures are observable almost without any jitter, underlying how regularly these vortices have been triggered by the vortices regularly shed by the lip. Finally, at the last downstream position reported here, the inner vortices begin to fade, while the outer ones become too big and affected by jitter to be correctly characterized by means of the present technique.

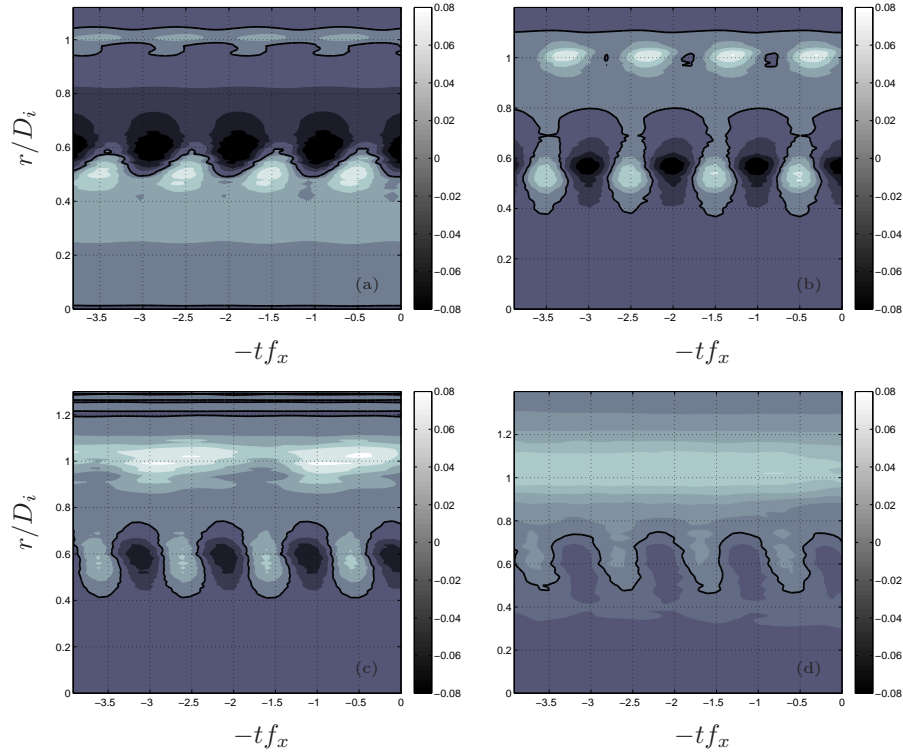


FIGURE 6.15. Conditionally sampled radial velocity for $r_u = 0.96$ at (a) $x/D_i = 0.24$, (b) $x/D_i = 0.5$, (c) $x/D_i = 1.0$, (d) $x/D_i = 2.0$.

Figure 6.16 shows that for $r_u = 3.14$ the dynamic is slightly similar to the one describe above with some remarkable differences, related to the slower vortex evolution. At $x/D_i = 0.24$ there is an hint of vortex organization in the ISL on the high speed side, which agrees with the numerical model of Boldman *et al.* (1976). Further downstream, the high shear of the OSL provides a faster growth of the Kelvin-Helmholtz instability, which soon overwhelms the inner layer dynamics. At $x/D_i = 0.5$ the outer vortices are clearly visible as well as the inner ones. The latter present periodical structures which are now forced by the outer layer as discussed in chapter 5 of the present thesis.

6.7. Reynolds and heat fluxes

The radial profiles in the near field of the shear stress \overline{uv}/U_i^2 are reported in figure 6.17 where it is discernible how the presence of the thick wall affects mostly the initial dynamics of all the cases reported here.

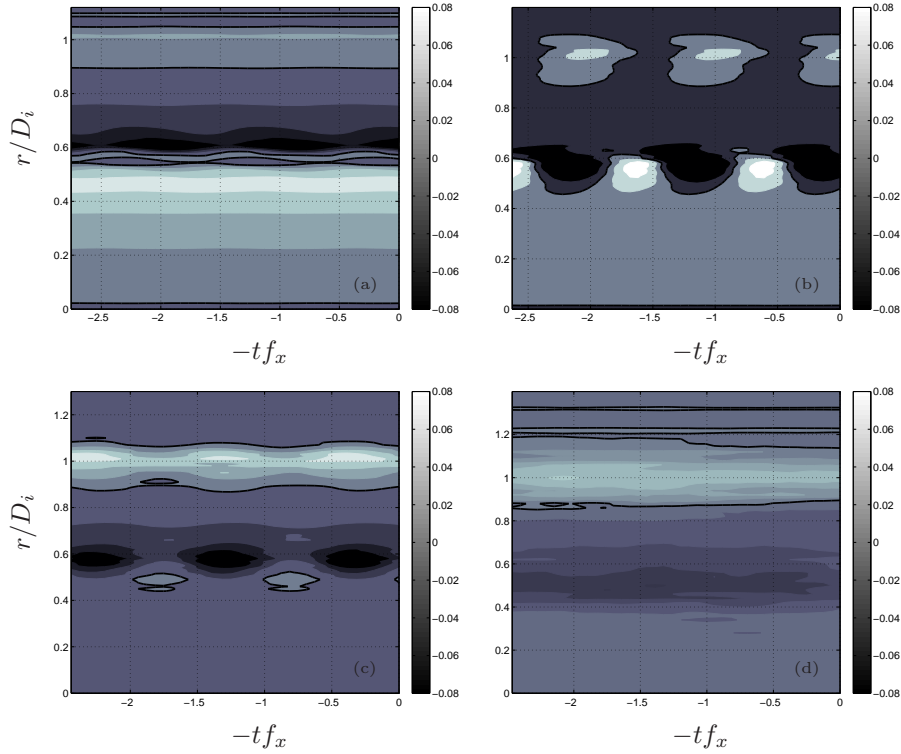


FIGURE 6.16. Conditionally sampled radial velocity for $r_u = 3.14$ at (a) $x/D_i = 0.24$, (b) $x/D_i = 0.5$, (c) $x/D_i = 1.0$, (d) $x/D_i = 2.0$.

The $r_u = 0.33$ case shows immediately at the exit a bell shape shear stress profile (typical of mixing layers) in the ISL, while the OSL appears to be independent from the change of the initial conditions. The higher shear stress in the ISL is again symptomatic of the higher initial perturbation level imposed by the wake to the shear layer. The unitary velocity ratio presents an ISL shear stress profile where two opposite peaks are discernible (typical of wakes) while the OSL, which has higher initial shear stress, is soon overtaken by the corresponding sharp wall related shear stress which had previously a slower evolution. For highest, the shear stress \overline{uv}/U_i^2 changes its sign in the inner layer by changing the separating wall, underlying again a strong initial effect of the wake on the initial turbulence.

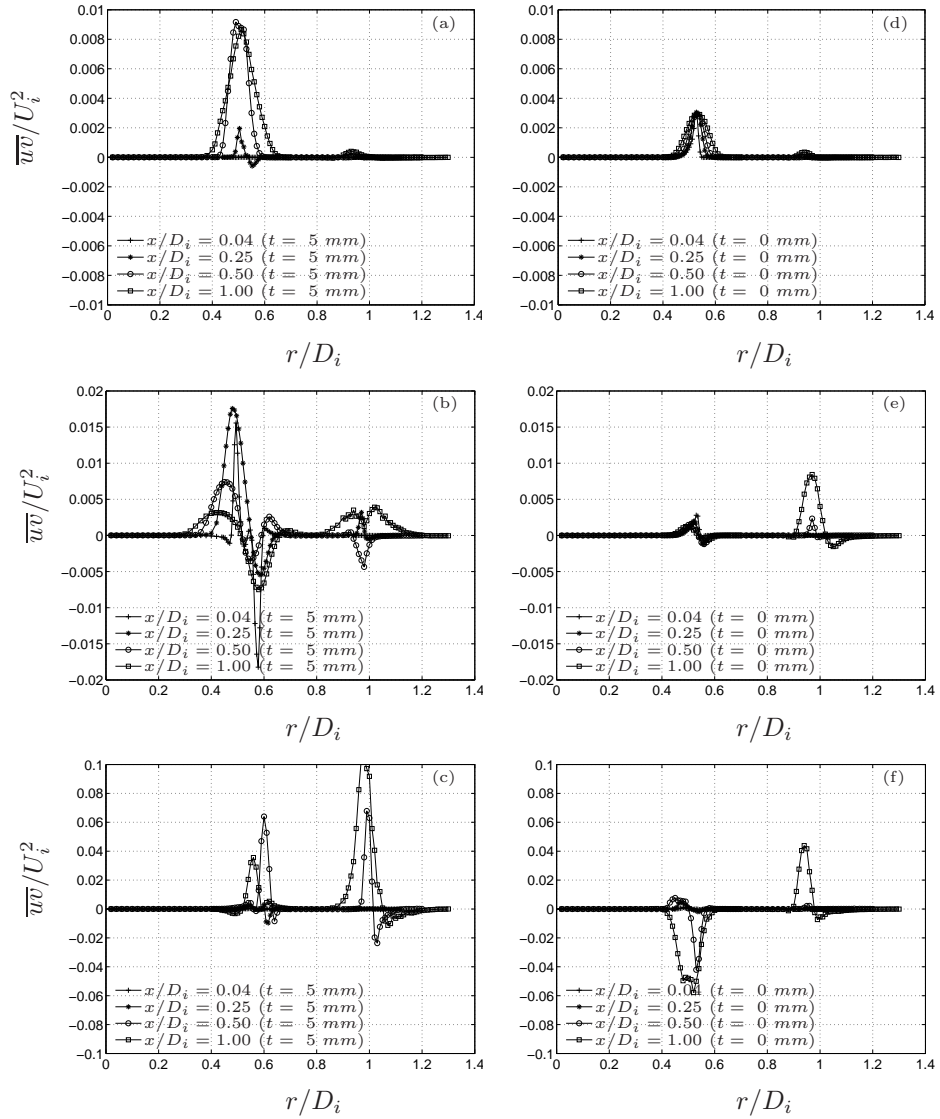


FIGURE 6.17. Reynolds stress \overline{uv}/U_i^2 profiles for (a,d) $r_u = 0.33$, (b,e) $r_u = 0.96$, (c,f) $r_u = 3.14$ with the (a,b,c) thick and (d,e,f) sharp wall for $x/D_i = 0.04, 0.25, 0.5, 1.0$.

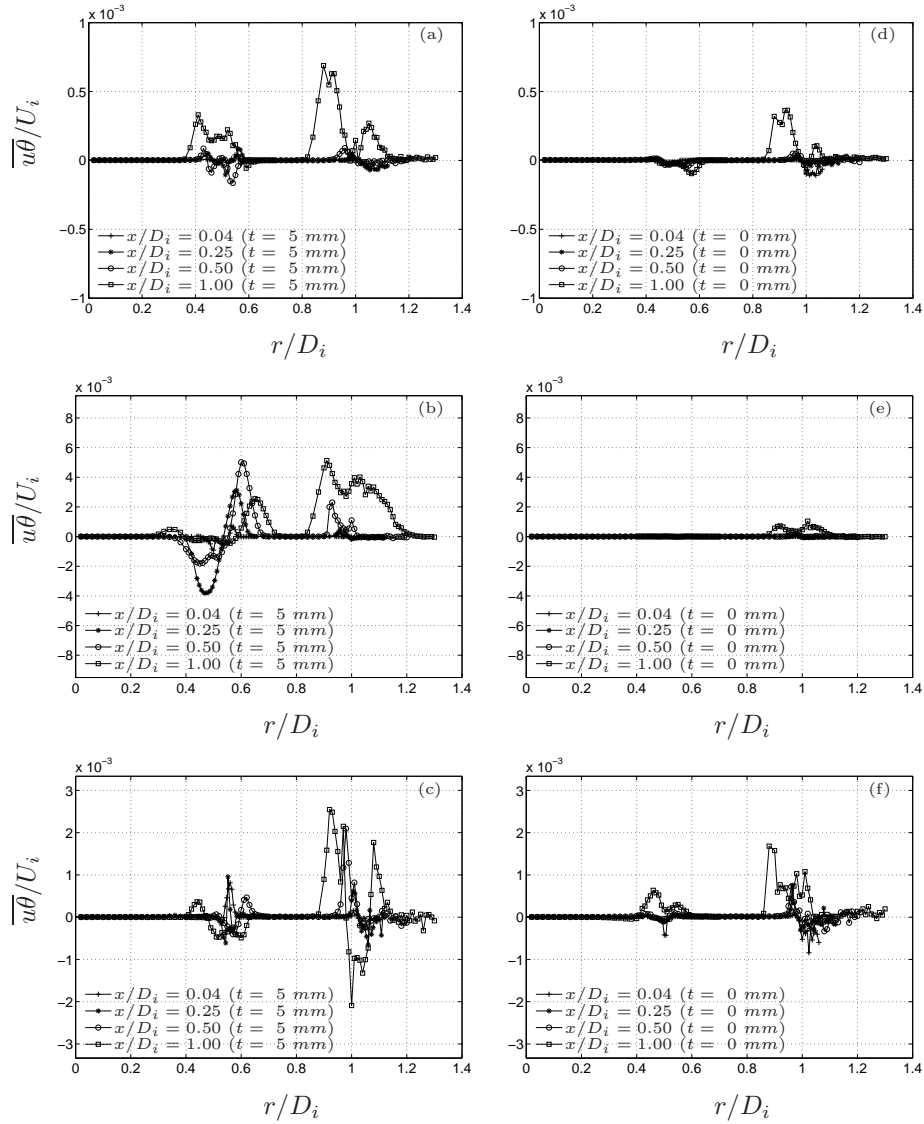


FIGURE 6.18. Streamwise heat flux $u\theta$ profiles for (a,d) $r_u = 0.33$, (b,e) $r_u = 0.96$, (c,f) $r_u = 3.14$ with the (a,b,c) thick and (d,e,f) sharp wall for $x/D_i = 0.04, 0.25, 0.5, 1.0$.

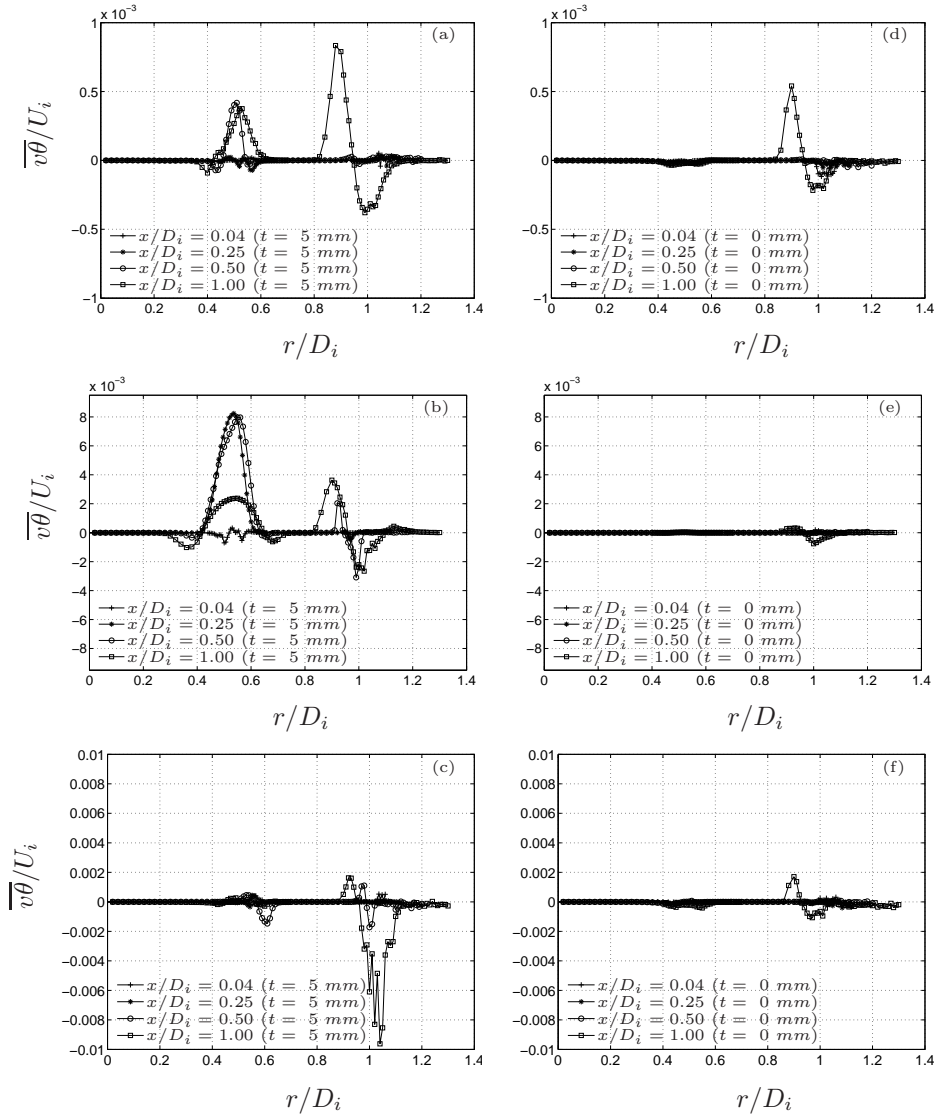


FIGURE 6.19. Radial heat flux $v\theta$ profiles for (a,d) $r_u = 0.33$, (b,e) $r_u = 0.96$, (c,f) $r_u = 3.14$ with the (a,b,c) thick and (d,e,f) sharp wall for $x/D_i = 0.04, 0.25, 0.5, 1.0$.

The streamwise and radial heat fluxes, $\overline{u\theta}/U_i$ and $\overline{v\theta}/U_i$, are reported in figures 6.18 and 6.19. As underlined before, the wake acts as a trigger to enhance the shear stress in the very near field. Both heat fluxes are indeed increased and a particular growth is observable in the radial heat flux. It is worth to say that, even in the lowest velocity ratio case, where the behavior is similar to the single jet case, the wake behind the splitter plate has still great influence in the reported shear stress and heat fluxes compared to the sharp wall case where the wake is almost negligible.

6.8. Joint probability density functions

The joint probability functions $p(u, v)$ and $p(v, \theta)$ at two points (one in the ISL at $x/D_i = 0.5$ and $r/D_i = 0.5$, the other in the OSL at $x/D_i = 0.5$ and $r/D_i = 1.0$) have been reported in figures 6.20-6.23 with both linear and logarithmic isocontour graphs. While the former is helpful to see the greatest contributions to the time history, the latter is able to enhance the pdf tails where much of the entrainment of external fluid takes place.

A common characteristics of all the figures is that the sharp wall related pdfs are quite regular with a single peak and a monotonic tail around it. In contrast, the thick wall related pdfs in ISL and OSL present often more than one single peak, behavior which is related to the presence of periodic components in the whole time history. This underlines, indeed, that the thick wall increases, in all the velocity ratios considered here, the coherency of the flow field due to the presence of vortex shedding (in the unitary velocity ratio) or to the presence of a trigger given by the wake component which increases the initial perturbation level with a faster emergence of the preferred instability. This explains why such behavior is not observed in the sharp wall case where only small external perturbations only excite the flow. The low velocity ratio pdfs, in particular, present some visible change only in the ISL where a greater organization is observed with the thick wall, while the outer layer appears unaffected by the change of the wall.

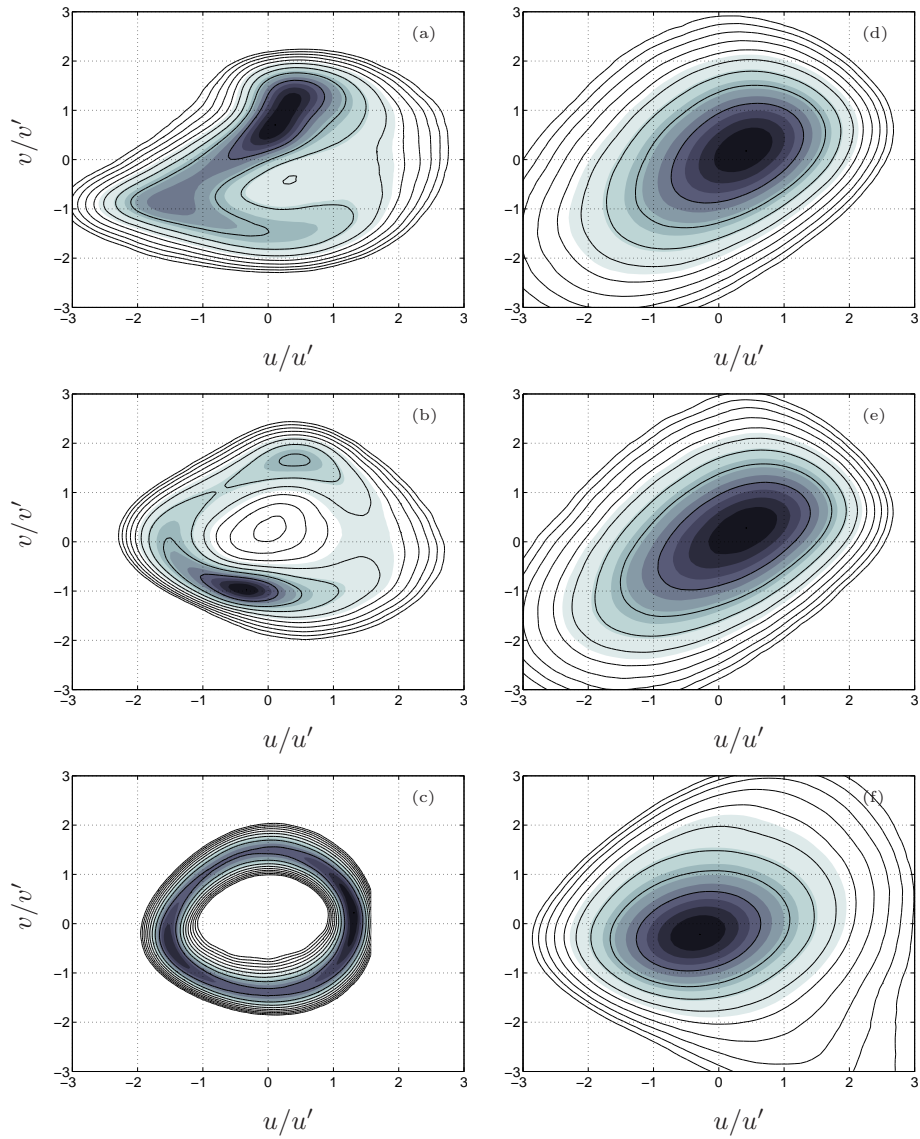


FIGURE 6.20. Joint uv pdf at at $x/D_i = 0.5$ and $r/D_i = 0.5$ for (a,d) $r_u = 0.33$, (b,e) $r_u = 0.96$, (c,f) $r_u = 3.14$ with the (a,b,c) thick and (d,e,f) sharp wall. Here the jpdfs are reported in linear (shadow area) and logarithmic form (isocontour lines).

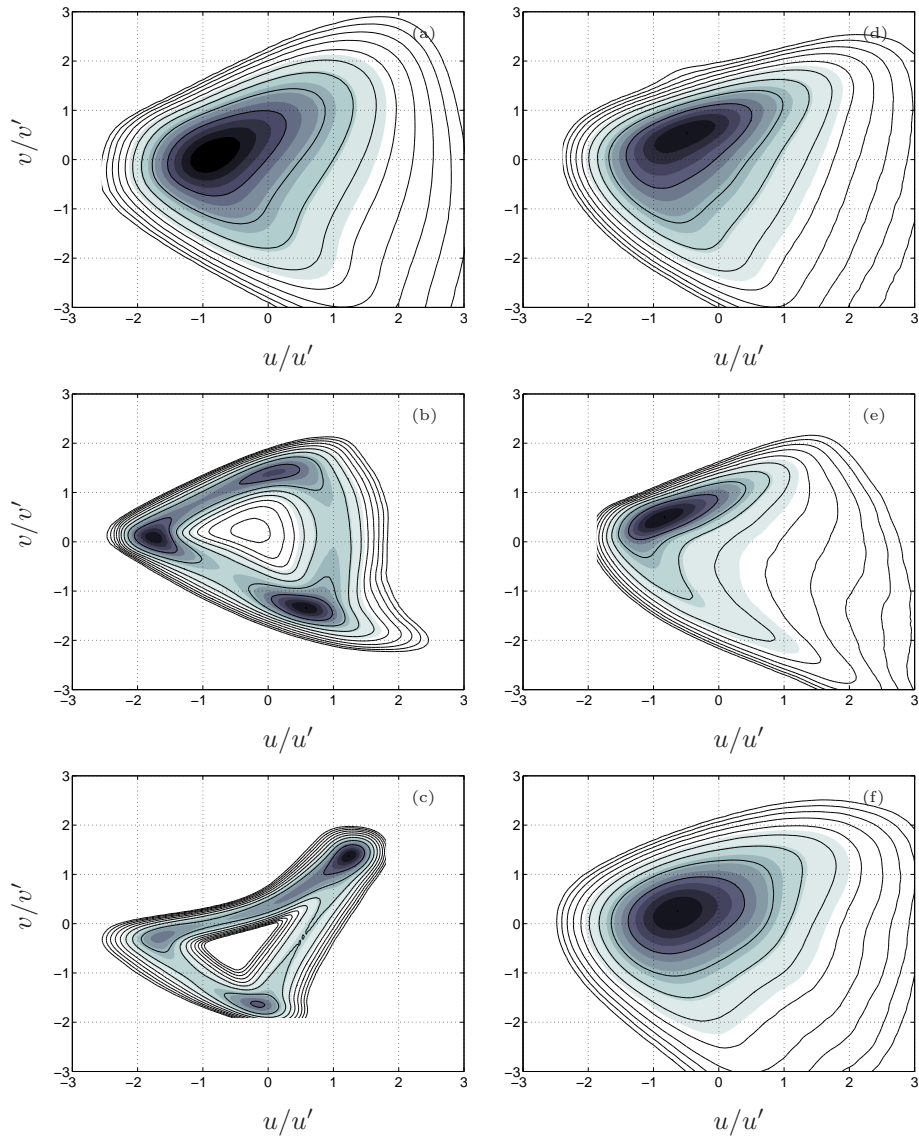


FIGURE 6.21. Joint uv pdf at $x/D_i = 0.5$ and $r/D_i = 1$ for (a,d) $r_u = 0.33$, (b,e) $r_u = 0.96$, (c,f) $r_u = 3.14$ with the (a,b,c) thick and (d,e,f) sharp wall. Here the jpdfs are reported in linear (shadow area) and logarithmic form (isocontour lines).

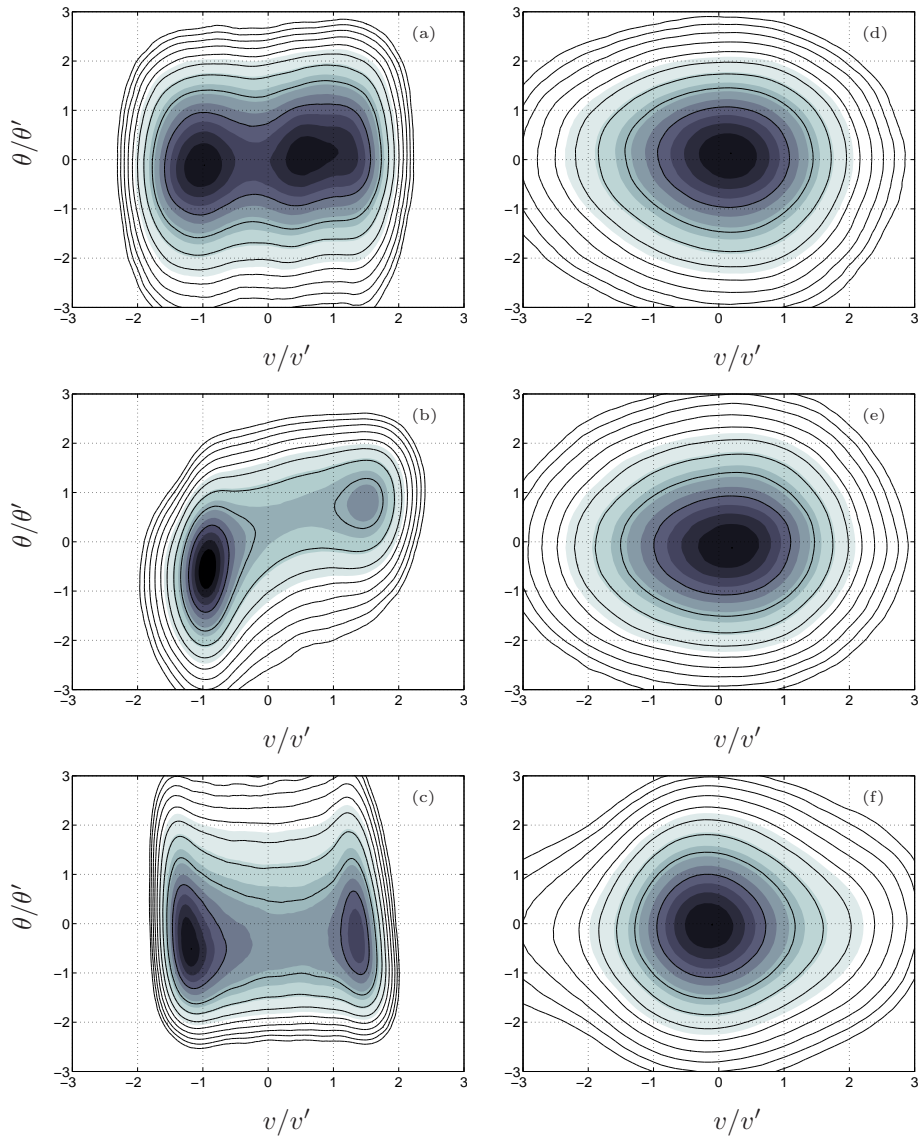


FIGURE 6.22. Joint $v\theta$ pdf at $x/D_i = 0.5$ and $r/D_i = 0.5$ for (a,d) $r_u = 0.33$, (b,e) $r_u = 0.96$, (c,f) $r_u = 3.14$ with the (a,b,c) thick and (d,e,f) sharp wall. Here the jpdfs are reported in linear (shadow area) and logarithmic form (isocontour lines).

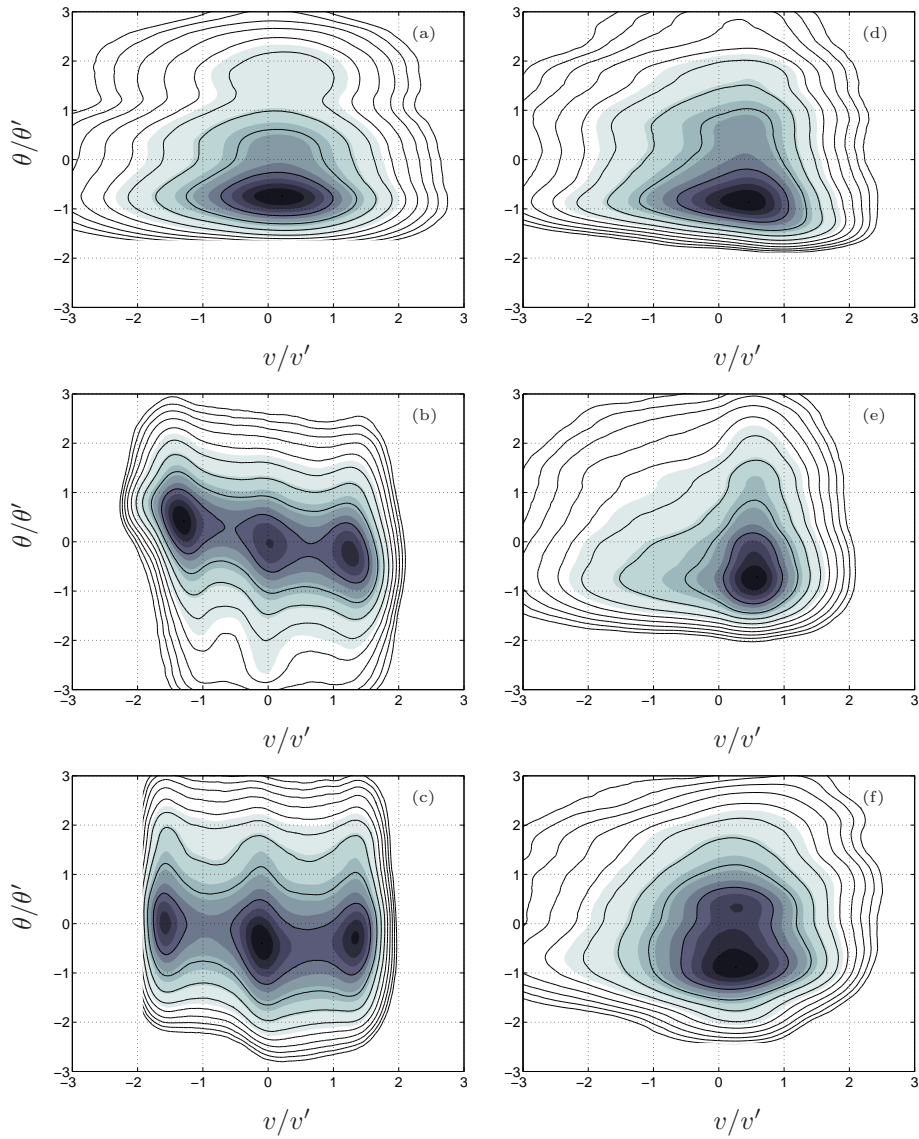


FIGURE 6.23. Joint $v\theta$ pdf at $x/D_i = 0.5$ and $r/D_i = 1$ for (a,d) $r_u = 0.33$, (b,e) $r_u = 0.96$, (c,f) $r_u = 3.14$ with the (a,b,c) thick and (d,e,f) sharp wall. Here the jpdfs are reported in linear (shadow area) and logarithmic form (isocontour lines).

Effect of acoustic forcing in the near field

7.1. Generalities

Theoretical and experimental studies on plane mixing layers and jet shear layers have underlined that mixing layers act as noise amplifiers, namely they tend to amplify external noise during the flow evolution. In particular, the stability analysis of Michalke (1965) showed that the amplification is selective, namely not all the frequencies are amplified the same. This implies that exists at least one frequency which is the most amplified. In absence of acoustic excitation, the perturbations contained in a low-turbulence freestream are similar to white noise and, indeed, only the preferred frequency emerges as the frequency with the greatest energy. In mixing layers this selection mechanism gives birth to the Kelvin-Helmholtz instability which is observable in the beginning stage of the shear layer instability of a jet before the vortex "roll-up". Becker & Massaro (1968) studied experimentally this instability Michalke (1965) and Zaman & Hussain (1980) where the authors suggested a scaling relationship $St_\theta = f_{KH}\theta/U_o \approx 0.012$ to find the preferred frequency f_{KH} from the jet velocity U_o and the momentum thickness θ of the boundary layer at the jet lip.

Flow control of coaxial jet have been performed by few experimenters and principally by means of active methods, like the MEMS devices used by Angele *et al.* (2006), or by the addition of swirl by Ribeiro & Whitelaw (1980). Today the main strategy to control the coaxial jets flow is still based on the experimental observations regarding the outer shear layer dominance, which has proven itself as a good way to control the flow initial evolution. Amongst the experiments where acoustic excitation have been used in coaxial jets, it is possible to cite Lepicovsky, Ahuja & Burrin (1985), Tang & Ko (1994), Kiwata *et al.* (2001) and Burattini & Talamelli (2007). Many of them tried to excite the flow at a single frequency (sometimes together with its subharmonic), but only few on them justified the chosen frequency by means of physical arguments, choosing it as the one with the maximum flow response.

The presence of the vortex shedding phenomenon was already assessed (Buresti *et al.* 1994) as well as the consequences in terms of flow control (Örlü *et al.* 2008a) and mixing (Segalini & Talamelli 2007). However, there are still some doubts about the instability character, because there is still no experimental proof of the presence of an absolute instability in the parameter space.

The confirmation of this has important consequences in terms of robustness and sensibility of this passive excitation mechanism and therefore it aims this chapter in which acoustic excitation has been used to evince the sensibility of the velocity field to acoustic waves.

7.2. Acoustic excitation effects

The effect of forcing at different velocity ratios is reported in figure 7.1 where some preliminary measurements of the radial velocity spectra at several excitation frequencies are shown. It is evident that for $r_u = 1$ there is almost no dependence on the acoustic forcing, while the opposite happens for the lowest and highest velocity ratio.

Figure 7.2 reports the $v'_{f_x,A}/(v'_{f_x,A})_{max}$ distribution for different excitation frequencies f_x at two different velocity ratios with the same outer jet velocity. Despite the fact that the dominant frequencies are the same, the physical motivations are different: for the $r_u = 1$ case the frequency is related to the vortex shedding behind the separating wall, while in the $r_u = 3.1$ case it is due to the Kelvin-Helmholtz instability of the outer layer. This statement is confirmed by calculating the Strouhal numbers St_t and St_{θ_o} which are $St_t = 0.235$ and $St_{\theta_o} = 0.0114$ in the $r_u = 1$ case and $St_t = 0.348$ and $St_{\theta_o} = 0.0111$ in the other one. This clearly underlines that at high velocity ratios only the Kelvin-Helmholtz instability is dominant while, at intermediate velocity ratios, both phenomena could even be present, but the dynamic is dominated by the vortex shedding, as observed by Örlü *et al.* (2008a). It is also interesting to note that at the highest velocity ratio the amplitudes scatter around the preferred frequency is greater than the one at $r_u = 1$, suggesting a higher dependence on the flow perturbations and, consequently, a convective-type instability in the former case and a different behavior at intermediate velocity ratios.

The preferred frequency must be related to some length and velocity scale of the jet itself. It is important to point out now that, in the near field, the characteristic length scales underlined in previous analyses are the momentum thicknesses of the boundary layers θ_1 , θ_2 and θ_3 as well as the separating wall thickness t which, according to Buresti *et al.* (1994), is the proper scale for intermediate velocity ratios.

Figure 7.3 reports the preferred excitation frequencies scaled with different characteristic velocity and length scales. As clear from 7.3(a) the Strouhal number in inner variables $St_{\theta_i} = \bar{f}\theta_i/U_i$ collapse, for low velocity ratios, on the single jet value of 0.012 (Zaman & Hussain 1980) and this can be physically explained by considering that, for low velocity ratios, the outer jet becomes negligible when compared to the inner one which becomes like a single axisymmetric jet. At intermediate velocity ratios the scaled Strouhal number $St_{t_x}/H(r_u) = \bar{f}t_x/(U_m H(r_u))$ is very close to the previously found value of 0.403 (figure 7.3(b)) while, at high velocity ratios there is a convergence of

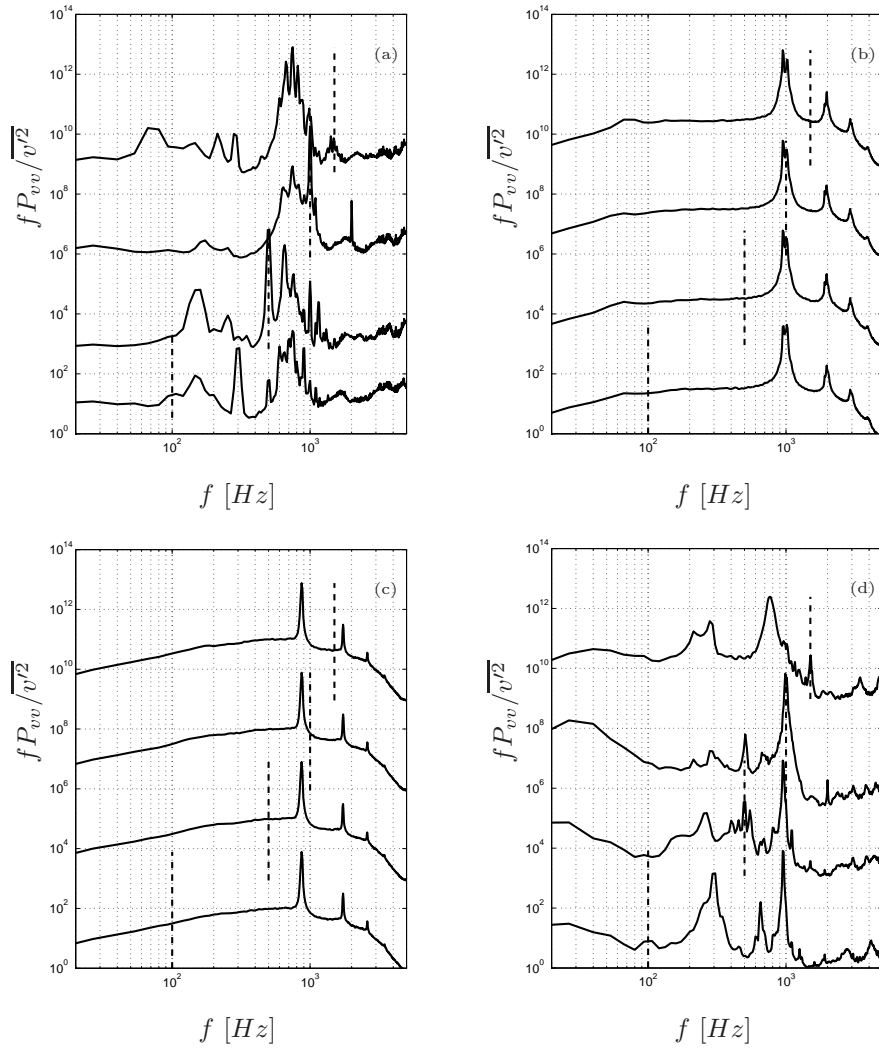


FIGURE 7.1. Radial velocity power density spectra measured at $x/D_i = 0.25$ $r/D_i = 0.5$ with four different excitation frequencies f_x at (a) $r_u = 0.33$, (b) $r_u = 1.0$, (c) $r_u = 1.25$, (d) $r_u = 3.1$. The dashed lines are the different excitation frequencies used in each test.

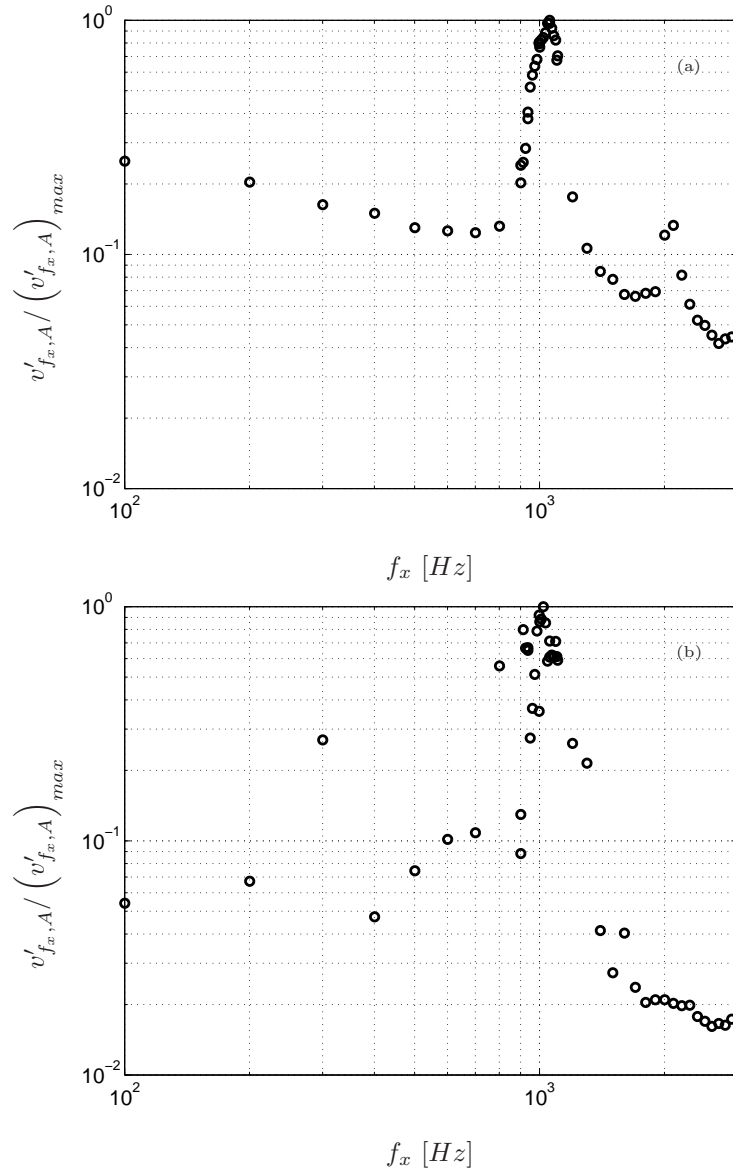


FIGURE 7.2. $v'_{f_x, A}$ distribution for various excitation frequencies f_x at (a) $r_u = 1.0$, (b) $r_u = 3.1$

the outer variables Strouhal number $St_{\theta_o} = \bar{f}\theta_o/U_o$ toward 0.012 which again agrees well with Zaman & Hussain (1980) (figure 7.3(c)). It is worth noting that the control point, which lies in the ISL, had a preferred frequency which scales in outer variables and, indeed, is dominated by the dynamics of the outer shear layer as already stated by Dahm *et al.* (1992) and da Silva *et al.* (2003).

From the above considerations there are three regions distinguished by the velocity ratio where it is possible to argue what is the observed main instability. To investigate the character of such instabilities different forcing amplitudes have been tested to check the flow response. Figures 7.4-7.6 report some details regarding this aspect for three different velocity ratios. At the lowest and highest velocity ratio reported here, there is a clear dependence on the excitation level clearly visible in the radial velocity power density spectra and in the probability density functions. Variations in the pdfs indicate a strong change in the whole time history character and could be due to an excessive forcing amplitude, or to a change in the flow behavior by an enhanced feedback mechanism for an increased vortex organization. The dependence on the pdfs is relatively small for low and intermediate velocity ratios, but becomes significant at high velocity ratios, implying a dramatic change in the whole velocity signal due to the forcing.

To evaluate the effect of forcing amplitude to the measured $v'_{f,A}$, part (c) of figures 7.4- 7.6 reports the variation of $v'_{f,A}$ with $(u_{CL})'_{f,A}$ scaled by their minimum value. The latter quantity is an indicator of the forcing strength by means of the amplitude of the streamwise velocity oscillation around the excitation frequency at the inner jet centerline. Again, while the low and high velocity ratios show a clear dependence, the unitary velocity ratio case does not show a remarkable increase of $v'_{f,A}$, except for the highest $(u_{CL})'_{f,A}$ where the loudspeaker has been loud enough to alter the whole flow field.

In order to analyze all the investigated velocity ratios and to determine where the sensibility is low, three different indexes are defined. The first one I_1 , reported for different velocity ratios r_u in figure 7.7, is related to the standard deviation of the fluctuation intensity $v'_{f,A}$ divided by its mean value:

$$I_1 = \frac{E_A \left[\left(v'_{f,A} - E_A \left(v'_{f,A} \right) \right)^2 \right]}{E_A \left(v'_{f,A} \right)}$$

where the operator $E_A(\cdot)$ is the mean estimator with respect to the changing forcing amplitude A .

The second index, with distribution reported in 7.8, is related to the standard deviation of the pdf $p_{f,A}(v)$ due to the forcing A and is defined as:

$$I_2 = \int_{\mathbb{R}} \sqrt{E_A \left(p_{f,A}^2(v) \right) - E_A^2 \left(p_{f,A}(v) \right)} dv$$

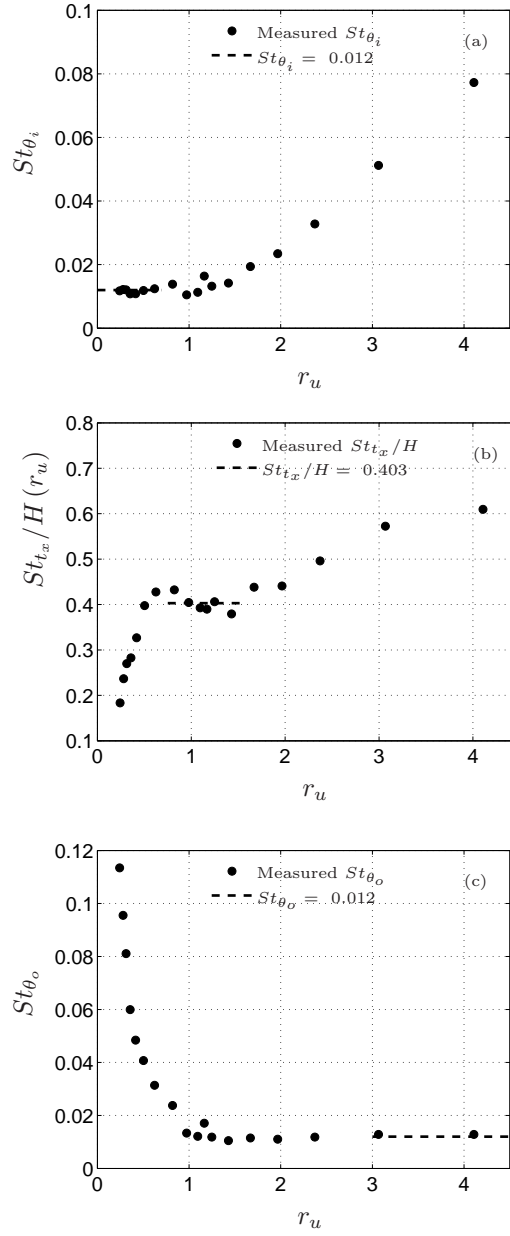


FIGURE 7.3. Preferred dimensionless frequency versus velocity ratio. (a) $St_{\theta_i} = \bar{f}\theta_i/U_i$ (b) $St_{t_x}/H(r_u) = \bar{f}t_x/(U_m H(r_u))$, (c) $St_{\theta_o} = \bar{f}\theta_o/U_o$

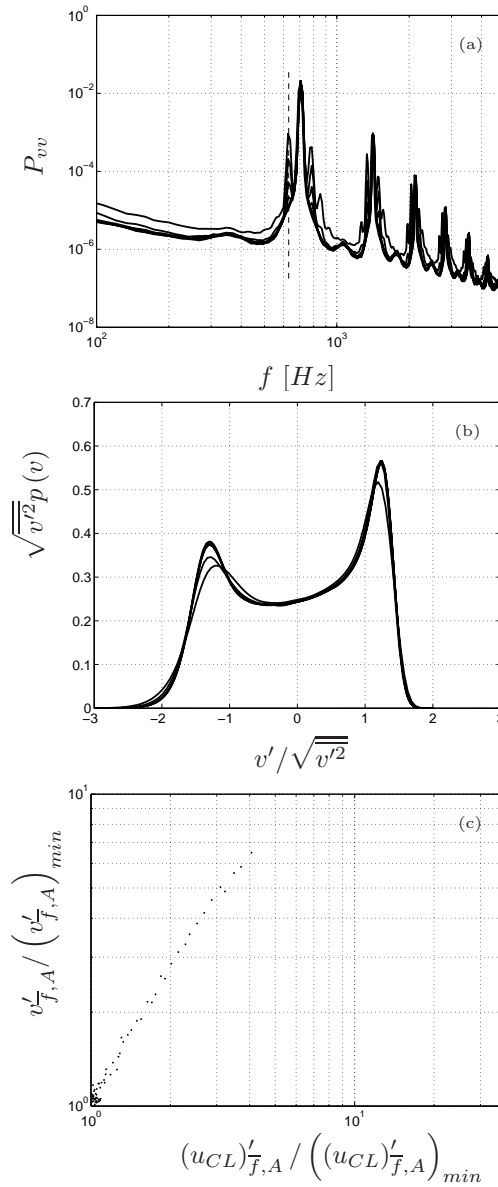


FIGURE 7.4. Flow response at the control point due to the acoustic forcing at $r_u = 0.36$. (a) radial velocity power spectral density at seven excitation amplitudes (b) scaled probability density function at seven excitation amplitudes (c) variation of $v'_{f,A}$ with $(u_{CL})'_{f,A}$ for all excitation amplitudes.

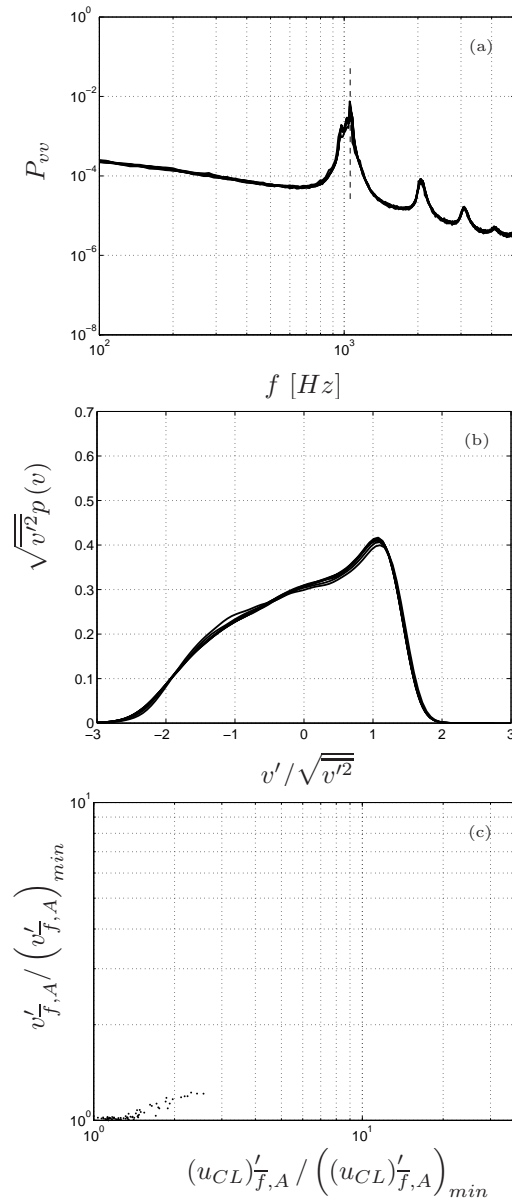


FIGURE 7.5. Flow response at the control point due to the acoustic forcing at $r_u = 1.0$. (a) radial velocity power spectral density at seven excitation amplitudes (b) scaled probability density function at seven excitation amplitudes (c) variation of $v'_{f,A}$ with $(u_{CL})'_{f,A}$ for all excitation amplitudes.

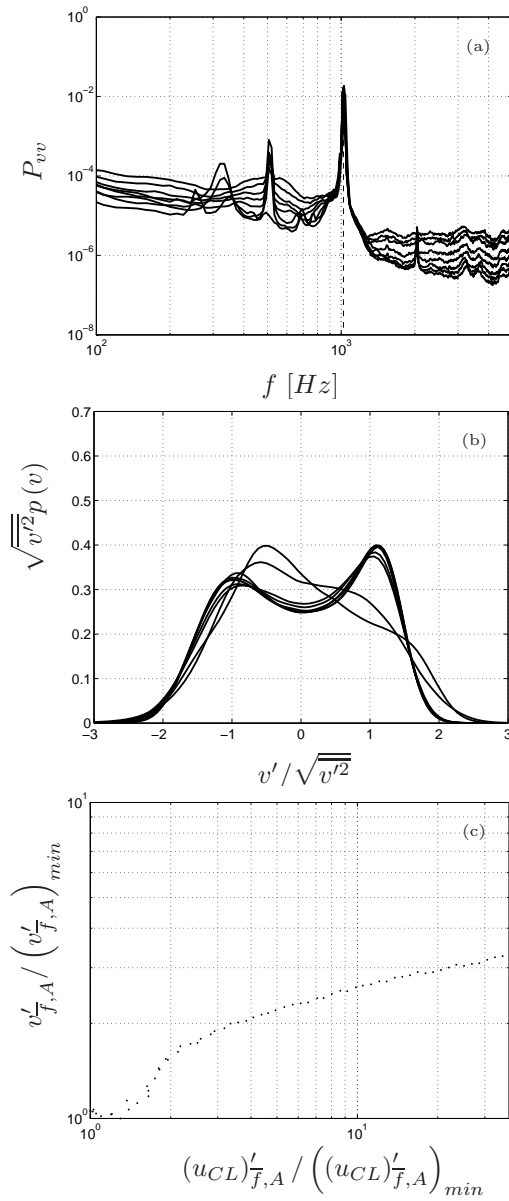
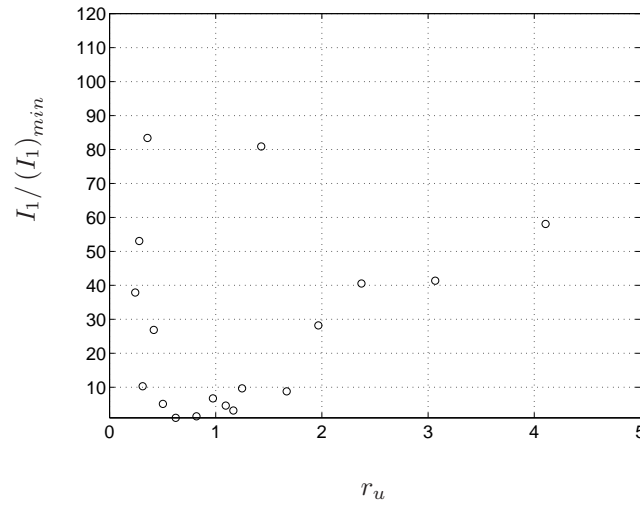
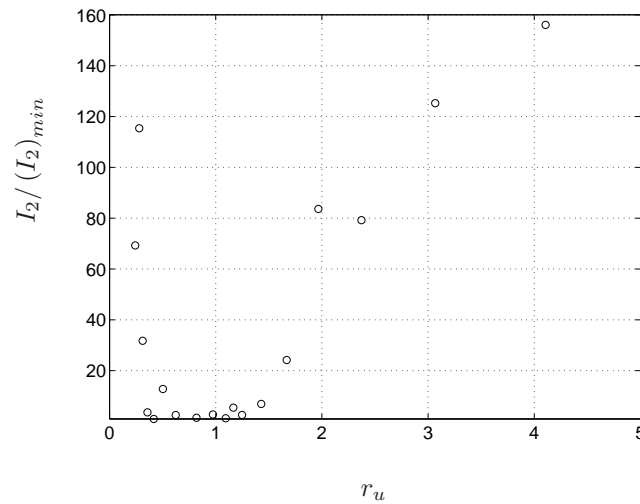
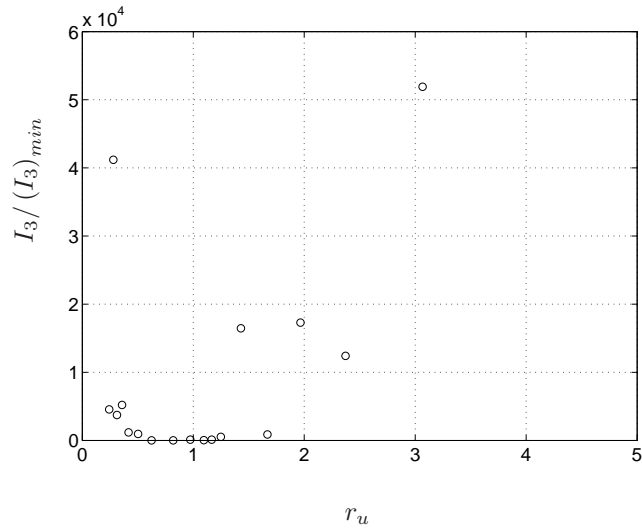


FIGURE 7.6. Flow response at the control point due to the acoustic forcing at $r_u = 3.3$. (a) radial velocity power spectral density at seven excitation amplitudes (b) scaled probability density function at seven excitation amplitudes (c) variation of $v'_{f,A}$ with $(u_{CL})'_{f,A}$ for all excitation amplitudes.

FIGURE 7.7. I_1 distribution at various velocity ratios r_u FIGURE 7.8. I_2 distribution at various velocity ratios r_u

The third index I_3 is the correlation coefficient between $(u_{CL})'_{f,A}$ and $v'_{f,A}$ able to evince the dependence on the forcing amplitude. Its variation with the velocity ratio is reported in figure 7.9.

When someone of these indexes is low, it means that the sensibility is low, while the opposite is true if the index is high. Since the three indexes

FIGURE 7.9. I_3 distribution at various velocity ratios r_u

are related to different physical properties, a quantitative comparison is not possible. However, after the choice of a proper threshold, it appears that at high and low velocity ratios there is a remarkable dependence on the acoustic excitation which affect the velocity fluctuations, spectra and even the whole probability density function. At velocity ratios inside the range $0.6 < r_u < 1.6$ the flow appears to be independent on the forcing except for very strong forcing.

CHAPTER 8

Conclusions

In this thesis, the experimental analysis of flow and mixing in the near and intermediate field of coaxial jets has been performed with the aim to study the flow evolution and to determine the leading parameters which affect the dynamics. In particular, the experimental campaign has focused on the characterization of a vortex shedding phenomenon behind the thick separating wall between the two streams and on its potential as a passive control mechanism. All the experiments have been performed through hot-wire anemometry and flow-visualizations to get a quantitative and qualitative description of the flow.

According to many authors (Olsen & Karchmer 1976; Buresti *et al.* 1994; Örlü *et al.* 2008a), when the separating wall is thick enough and the velocity ratio close to one, an hydrodynamic resonance is observed in the flow field with the form of some periodic vortices shed from the wall itself. Örlü *et al.* (2008a) observed that the vortex shedding, behind a separating wall with high thickness, dictates the passage frequency of the external shear layers vortices and thereby controls the inner and outer shear layers evolution in the whole near-field region. This property reverses the conventional picture of the “lock-in phenomenon” (Dahm *et al.* 1992; da Silva *et al.* 2003) where the outer vortices dominate the dynamics of the inner layer, with the inner vortices that are trapped into the free spaces of the Kelvin-Helmholtz instability of the external shear layer. The justification of the vortex shedding phenomenon was put forward by the theoretical analysis of Talamelli & Gavarini (2006), which underlined that the coaxial jets flow is absolutely unstable, under certain operating conditions, and therefore a global oscillating mode could exists.

The main instabilities that are in charge of the dynamics of the near field region have been here investigated for different operating conditions. By varying the velocity ratio $r_u = U_o/U_i$ between the two streams, it has been possible to significantly change the operating regime. Depending on the velocity ratio, three different dominant instabilities have emerged:

- For low velocity ratios, the inner jet determines the main instability which has been observed in the inner shear layer, while the outer layer develops its own preferred instability separately. This picture is in agreement with the model proposed by Ko & Kwan (1976) in which the coaxial jets flow is thought as a combination of several single jets;

- In the intermediate velocity ratio region a vortex pattern (similar to the Von Karman vortex street) is distinguishable behind the separation wall, as found by Buresti *et al.* (1994), Burattini (2002) and Örlü *et al.* (2008a). The wake instability is found to be dominant and it affects the dynamics of both the inner and the outer layer, reversing the lock-in phenomenon described by Dahm *et al.* (1992). A different scaling from the one present in literature (Buresti *et al.* 1994) has been proposed to reduce the Reynolds number and velocity ratio effects on the dimensionless frequency. The Reynolds number dependence has been corrected by adding to the separation wall thickness t the δ_{99} of the boundary layers adjacent the wall, in agreement with the empirical law proposed by Dziomba & Fiedler (1985). The velocity ratio dependence, due to the competition of the wake versus the mixing layer component, has been estimated via a simple empirical expression. The resulted scaled Strouhal number has been found to be constant in the whole intermediate region, namely in the range $0.75 \leq r_u \leq 1.6$;
- For high velocity ratios there is a dominance of the outer shear layer which forces the inner one to follow its dynamic. In this case the classical lock-in phenomenon is found, namely the velocity spectra of both shear layers present a peak at the same frequency dictated by the outer shear layer dynamics (da Silva *et al.* 2003).

The extension of the intermediate region seems to be a function of the thickness of the separating wall. Flow visualizations of coaxial jets with a sharp separating wall (with $t \approx 0$) have been reported in figure 2.10 for unitary velocity ratio. They have not shown any vortex shedding instability in the whole near field region but rather a sort of vortex organization in the ISL far downstream, with dynamics that prove totally different from the ones with the thick wall (figure 2.9) and treated in chapters 4 and 5. It can be conjectured that the switch between the two flow behaviors happens when a threshold thickness is surpassed. It is possible to use the result of Dziomba & Fiedler (1985) to both support this hypothesis and state that there is no wake effect when the separating wall thickness is small enough compared to the boundary layers.

The velocity and mixing fields in coaxial jets have then been studied experimentally with two different boundary conditions: one defined by a sharp separation wall between the two streams, and the other with a thick one, with the aim to investigate the flow field with and without a wake component in the velocity profile.

The comparison between the two different wall geometries for three different velocity ratios (namely $r_u = 0.33$, $r_u = 0.96$ and $r_u = 3.14$) has underlined that the duct wall wake affects the flow for all these velocity ratios with a maximum effect at r_u of about 1. In this case, the presence of the wake

instability is the cause of the enhanced fluctuation intensity in the velocity and temperature fields, due to the passive excitation of the velocity field which is triggered by the periodical detaching of vortices from the thick wall. This effects is evident in the inner region for all the considered cases. Spectral analysis as well as conditionally sampled measurements have confirmed this analysis, and highlighted that two clear rows of vortices have been observed in the inner layer for $r_u \approx 1$. The outer layer is clearly affected by these structures and develops outer vortices at the same frequency of the inner ones as described by Segalini & Talamelli (2007) and Örlü *et al.* (2008a). The coupling of both rows of vortices is observable inside the first inner diameter, after which pairing phenomena start in the outer layer while, at the same time, the inner vortices begin to loose continuously strength even if they are still clearly visible up to $3 D_i$.

The flow picture is different in the low velocity ratio range where the inner layer develops its own shear layer mode which does not influence noticeably the outer layer. In this case, the thick wake behind the duct wall increases the ISL vortex formation, mainly because introduces strong perturbations immediately at the jet exit where velocity gradients are higher. The same mechanisms is responsible for the higher fluctuations observed at the high velocity ratios, where an increase in shear stress has been observed whereas streamwise and temperature fluctuations achieve the same qualitative profile with a slightly faster growth. The wake component, which is visible immediately at the exit in both cases, soon disappears and it is substituted by a mixing layer profile. Therefore difference between the two walls will be soon smoothed out.

The analysis of the velocity spectra and of the joint probability density functions has confirmed that the thick wall geometry imposes a greater coherency in the whole flow field and especially in the shear layers. On the other hand, the analysis of inner/outer layer thickness slope (dL/dx) has also confirmed that both layers grow faster when the thick wall is mounted, underlying indeed the practical value of the use of a thick wall geometry, which does not need any external energy supply and can be so viewed as a passive way to excite the flow field. The flow control can be achieved efficiently for intermediate velocity ratios (namely r_u near 1), where the wake has its greatest effect due to the presence of the absolute wake instability which, in this case, drives the whole near field (Buresti *et al.* 1994)-(Örlü *et al.* 2008a).

Finally, the flow response to acoustic excitation has been studied in order to investigate the stability nature of the shedding phenomenon. Several velocity pairs (U_i, U_o) have been investigated to understand the dependence at different velocity ratios and Reynolds numbers to the acoustic forcing. One of the first result presented here shows clearly that the frequencies where the maximum flow response is observed, are linked to some characteristic velocity and length scales depending on the velocity ratio r_u . In particular, for low velocity ratios ($r_u < 0.5$), the frequency scales with the inner jet velocity and the innermost

boundary layer momentum thickness θ_i , obtaining a Strouhal number of 0.012, which is in close agreement with the results of Zaman & Hussain (1980) for axisymmetric shear layers. Indeed, for low velocity ratios, the dynamics is ruled by the inner shear layer which has typically a convective-type instability. For high velocity ratios the frequency scales with the outer jet velocity and the outermost boundary layer momentum thickness θ_o , obtaining a Strouhal number of about 0.012 again. This agrees with the observations of da Silva *et al.* (2003) where it was observed that, for high velocity ratios, the vortices of the inner and outer shear layer develop with the same passage frequency due to the stronger influence of the Kelvin-Helmholtz vortices on the OSL which is convective-type, too. At intermediate Reynolds number ($0.6 < r_u < 1.4$) the influence of the thick wake behind the separating wall becomes relevant and the preferred frequency is equal to the one of the vortex shedding phenomenon.

By means of acoustic forcing it has been possible to evince that the flow is sensible to external perturbations at low and high velocity ratios, while this dependence is absent for nearly unitary velocity ratios, underlining the different instability character of this flow regime. According to the stability analysis of Talamelli & Gavarini (2006), the region where the absolute instability is observable is centered around $r_u \approx 1$ with an extension which is a strong function of the wake velocity defect. By means of three indexes it has been possible to determine the boundaries inside which the sensibility to external perturbations has been negligible at the control point. Even if this does not mean rigorously the presence of an absolute instability, reversely only an absolute instability can provide this behavior confirming, indeed, the theoretical analysis.

These investigations underline the potential of this passive mechanism as an easy, effective and practical way to control the near-field of interacting shear layers, and shows that it can be used to increase the turbulence activity in both shear layers and hence the mixing between the two coaxial jet streams as well as the annular jet with the ambient fluid.

Despite the current trend to utilize mainly active flow control strategies in coaxial jet flows, there are basic flow features, like the vortex shedding behind a thick wall which, if correctly recognized, can be facilitated to control the flow field without external energy supply. Inside the intermediate velocity ratio range, there is an absolutely unstable region which self-excites the flow driving the dynamics with vortices shed from the separating wall. As demonstrated in this thesis, the reduced dependence on external perturbations underlines the robustness of the shedding phenomenon in the intermediate velocity ratio regime in a variety of possible operating conditions including the industrial ones.

APPENDIX A

The effect of oblique waves on jet turbulence

The material reported in this appendix has been presented by Segalini, Örlü, Alfredsson & Talamelli (2008) in the iTi Conference on Turbulence III, Bertinoro, Italy, during October 12-15.

A.1. Introduction

For many years investigations have been conducted in order to understand the flow instabilities that lead to transition in jets. Among the earliest, the inviscid linear stability analysis of Batchelor & Gill (1962) showed that immediately at the jet exit, where the velocity profile has a 'top-hat' behaviour, all the instability modes are able to be exponentially amplified while in the far field region only the helical mode seems to be unstable. The transition between these two different instability regions is still unclear and the analysis is complicated by the presence of several unstable modes embedded in the turbulence background. Therefore, a large amount of analytical theories, simulations and experiments have been done in order to highlight the role and the dynamics of a single or few modes in the evolution of the flow (Corke & Kusek 1993; Zaman & Hussain 1981).

Investigations in naturally and artificially excited jets have determined the importance of two instability lengthscales: one associated with the initial shear-layer thickness at the exit of the nozzle (Zaman & Hussain 1981), and the other associated with the jet diameter which governs the shape of the mean velocity profile at the end of the potential core (Crow & Champagne 1971). The instability modes in the first region develop through continuous and gradual frequency and phase adjustments to produce a smooth merging with the second region.

Axisymmetric excitation by means of acoustic forcing has been able to highlight several important aspects of the complex dynamics involved, like the role played by the so called shear layer (Zaman & Hussain 1981) and jet column mode (Crow & Champagne 1971) acting in the near field of the jet at the nozzle exit and at the end of the potential core, respectively, as well as the presence of several nonlinear interactions between scales and their strong influence in the flow evolution. However, fewer works have been devoted to the investigation

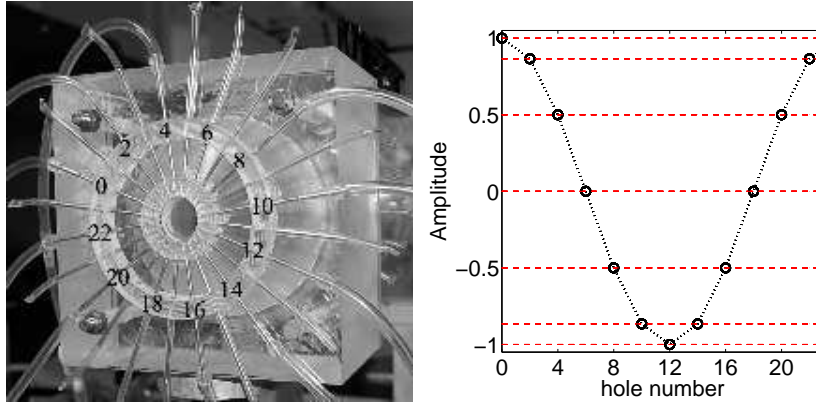


FIGURE A.1. Photo of the nozzle and excitation rig (*left*).
Excitation pattern (*right*).

of higher azimuthal modes principally due to the higher complexity of the excitation facility (Cohen & Wygnanski 1987*b*; Corke & Kusek 1993).

The motivation of this work was to investigate the possibility that non-linear combination of oblique waves generated by blowing and suction, in a manner similar to the one of Elofsson & Alfredsson (1998), could generate streamwise streaks able to alter the dynamics of the flow field.

In this paper a preliminary analysis on the effect of this excitation is presented. A detailed investigation with different excitation amplitudes, frequencies and velocities has been performed in order to evaluate the effects on the flow dynamics. In the future the possibility of the complete description of this complex evolution will be further investigated.

A.2. Experimental setup

The experiments have been carried out in the Fluid Physics Laboratory at the Linné Flow Centre at KTH Mechanics in Stockholm. The air, driven by a centrifugal fan, passed through a pre-settling chamber placed 3 m downstream in order to reduce the incoming disturbances from the fan. Flow conditioning is performed by means of a honeycomb positioned in the settling chamber after which a plexiglass nozzle with 0.025 m exit diameter is mounted. A short straight plexiglass tube section to provide the acoustic excitation, equipped with 24 perpendicular aligned metal tubes, is fixed to the nozzle exit as shown in figure A.1.

Velocity measurements have been performed by means of an in-house built X-wire probe using an *A.A. LAB AN-1003* anemometry system in CTA mode.

At the beginning of each set of experiments, the amplitude of each loud-speaker has been regulated in such a way that the streamwise velocity rms level

around the excitation frequency, measured with a single hot-wire, followed the law depicted in figure A.1.

A.3. Results, discussion and conclusions

Figure A.2 depicts flow visualisations from both an axisymmetric and oblique excitation. While the axisymmetry prevails for the $m = 0$ excitation, as apparent from figure A.2(a) and (b), the $m = \pm 1$ excitation produces a clear helical structure, as would be expected.

An extensive parametric study in terms of frequencies and amplitudes for a selected range of Reynolds numbers was performed in order to focus on the most influential parameter set. Since the aim of this work was to investigate the flow in the near field of the jet, a streamwise station of $x/D = 3$ has been chosen to investigate the effect of the excitation on the flow. Several combinations of Reynolds number and excitation frequency have been tested in order to evince the effect on the streamwise rms level. In figure A.3 the relative rms (compared to the unexcited or natural case) against the dimensionless frequency $St_{\theta_0} = f\theta_0/U_J$, where θ_0 is the initial momentum thickness of the boundary layer at the nozzle lip and U_J the jet exit velocity, has been reported. Due to the non negligible scatter, a moving average has been performed to clarify the figure. It is interesting to note that the largest reduction in the turbulence intensity can be observed around $St_{\theta_0} \simeq 0.012$, which is close to the value found for an axisymmetrically excited jet (Husain & Hussain 1995). This is

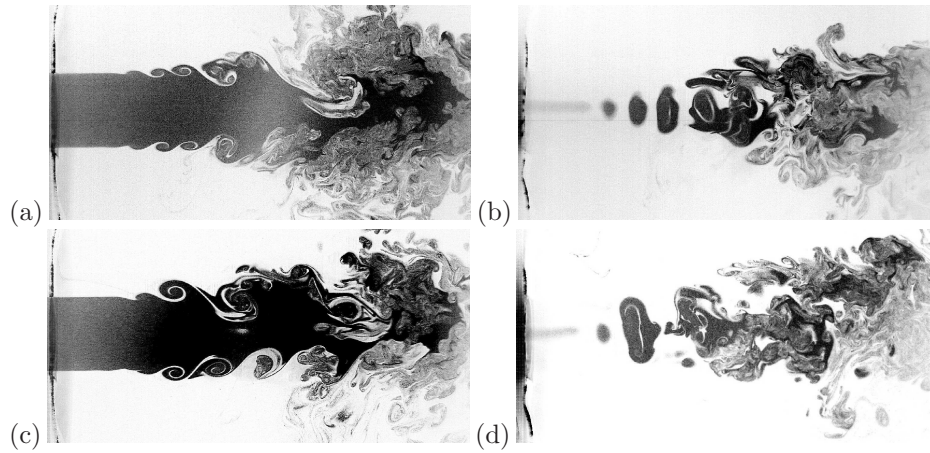


FIGURE A.2. Smoke flow visualisations at $Re_D \approx 8500$, based on nozzle diameter and exit velocity: unexcited jet, across $r/D = 0$ (a) and 0.5 (b), excited jet, $St_D = 0.5$ ($St_{\theta_0} \approx 0.005$) and $m = \pm 1$, across $r/D = 0$ (c) and 0.5 (d)

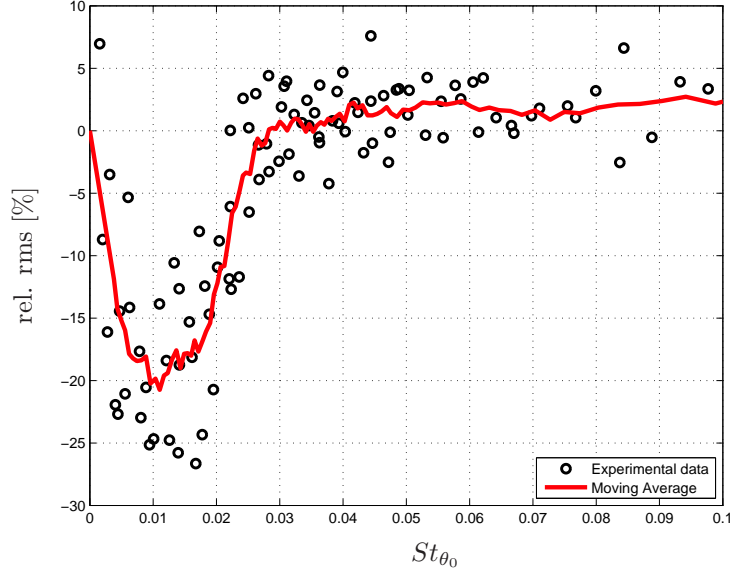


FIGURE A.3. Relative change in streamwise velocity rms at $x/D = 3$ between excited and unexcited case for different exit velocities.

also in accordance with the flow visualisations shown in figure A.2, where for the excited case a reduction in the incoherent (small-scale) turbulence can be anticipated.

In the following results for a Reynolds number of $Re_D = 25000$ will be presented where a frequency $f_{ex} = 1500$ Hz showed the strongest turbulence reduction (at least at $x = 3D$) and it will be referred to as the “excited case” in contrast to the natural case.

Some important aspects can be deduced from the autocorrelation function or the velocity spectra, reported in figure A.4. When the excitation frequency is close to the characteristic frequency of the shear layer, several nonlinear interactions appear within the first half diameter and then decay further downstream. At $x/D = 2$ the remaining peak is a subharmonic of the excitation frequency, which is somewhat similar to what was observed by Corke and Kusek Corke & Kusek (1993). It is worthwhile to note that the low frequency energy is lower than the unexcited case, meaning a strength reduction in the large scales due to the excitation at the jet exit.

The evolution of the spectra confirms that the excitation has a strong impact on the evolution of the whole flow field with the imposed periodicity given by the excitation itself. The scenario seems to be in agreement with the

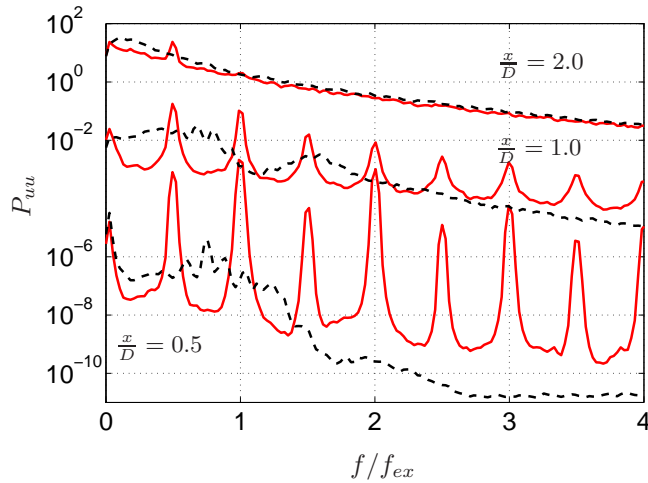


FIGURE A.4. Spectra in the shear layer region with highest turbulence intensity for $Re_D = 25000$ w/ excitation 1500 Hz (solid line) and w/o (dashed line).

one depicted by Batchelor & Gill (1962) with two unstable oblique modes that will combine to generate several nonlinear interactions. This process saturates most of the energy of the shear layer at the various frequencies and starts to decay faster compared to the natural case, with only some modes that will decay slower than others (from the spectral analysis it seems to be the subharmonic of the fundamental).

This reduction of turbulence could be connected to the same phenomenon described by Elofsson & Alfredsson (1998) about the effect of oblique waves in laminar boundary layers, where the authors showed that the interaction of two waves is able to generate streamwise streaks by means of nonlinear interaction. Unfortunately, in this first investigation it was not possible to detect the presence of such streaks, and this aspect must be further investigated in the future in order to understand the connection between the turbulence reduction and the azimuthal forcing.

APPENDIX B

Effect of probe alignment error in the mean and rms estimation of a turbulent boundary layer

B.1. Generalities

In wall bounded experiments great efforts are spent to ensure that measurements uncertainties are reduced as much as possible. The position of the measuring point with respect to the wall is one of them, because it generates sensible errors in the turbulence quantities we want to measure (see appendix C, for instance). Another effect, which has been less discussed, is the effect of the probe misalignment with respect to the wall in hot-wire measurements. The presence of a probe angle ε affects clearly the measurements due to the finite length of the wire. Many authors have studied the issue of the wire length and its filtering effect (Frenkiel 1949; Alfredsson *et al.* 1988; Ligrani & Bradshaw 1987; Suzuki & Kasagi 1992; Örlü & Alfredsson 2010) but, up to the author's knowledge, there is no literature where the effect of the probe misalignment has been quantified. This appendix aims therefore at the theoretical investigation of this error source in the mean and rms of the measured streamwise velocity and at the determination of a leading order correction.

B.2. Theoretical results

A xyz reference frame is defined with the x -axis aligned with the mean flow, the y -axis and the z -axis normal and parallel to the wall, respectively. As schematically reported in figure B.1, the wire is placed in the flow with its centre in $\mathbf{x}_0 = (x_0, y_0, z_0)$ and directed normally to the mean flow but with a small angle $\varepsilon \ll 1$ with respect to the z direction with a tangential versor $\mathbf{w} = (0, \varepsilon, 1)$. The generic point along the wire will be denoted as $\mathbf{s} = \mathbf{x}_0 + s\mathbf{w}$, where s ranges from $-L/2$ to $L/2$. In the followings, bold letter will indicate vector quantities to differentiate them from scalar quantities.

At this point, the cooling law of the wire has to be assumed. The convective heat transfer is often expressed with the King's correlation for infinite wire length:

$$Nu = A + BRe^{0.5} \tag{B.1}$$

where A and B are constants which depend of the fluid and of the thermal conditions (Bruun 1995). When the wire length is not infinite, the exponent in

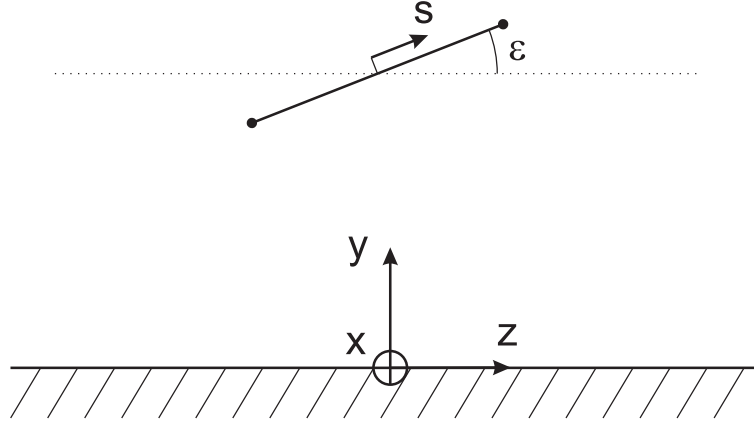


FIGURE B.1. Used reference frame.

equation B.1 becomes slightly less than 0.5 (usually around 0.45) and therefore will be denoted as the generic constant n . It is reasonable to consider now that the heat produced by the Joule effect is exchanged continuously with the fluid through forced convection rather than natural convection, which is negligible for high Reynolds numbers and low Grashof numbers, and irradiation (which becomes relevant only for very low Reynolds numbers). The conduction to the prongs is usually made small by using wires with high L/d which is the case assumed here. The heat transfer process is ruled by the average convective heat transfer h as:

$$\rho_w c \frac{\partial T_w}{\partial t} = \dot{Q} - h(\mathbf{s}, t) S_w (T_w(\mathbf{s}) - T_\infty) \quad (\text{B.2})$$

where ρ_w , c and S_w are the wire density, the thermal capacity and the wet surface. $T_w(\mathbf{s})$ and T_∞ are the local wire temperature and the ambient temperature, respectively. If the wire has negligible thermal inertia, as a wire operating in constant temperature mode (CTA), the RHS balances to zero, and equation B.2 becomes:

$$\dot{Q} = \frac{e_w^2}{R_w} = \int_{-L/2}^{-L/2} h(\mathbf{s}, t) \pi d (T_w(\mathbf{s}) - T_\infty) ds \quad (\text{B.3})$$

where e_w and R_w are the hot-wire tension and resistance, respectively. If we assume that the temperature along the wire $T_w(x)$ is constant in space and time, equation B.3 can be re-written as:

$$e_w^2 = A + B \int_{-L/2}^{-L/2} u^n(\mathbf{s}, t) ds \quad (\text{B.4})$$

where $u(\mathbf{s}, t)$ is the local streamwise velocity along the wire in the point \mathbf{s} and A and B are constants. The effect of other velocity components has not been taken into account in the present appendix.

It is possible to assume now that the hot-wire calibration law has the following general form:

$$\left(\frac{1}{L} \int_{[-\frac{L}{2}, \frac{L}{2}]} u^n(\mathbf{s}, t) ds \right)^{1/n} = f[e_w(t)] \quad (\text{B.5})$$

From equation B.5 we note that the RHS is the calibration function of the anemometer (which could be the King's law, a polynomial or a look-up table), while the LHS is similar to the integral average of the velocity along the wire.

Here a time average operator $\langle \cdot \rangle$ is defined, while the local flow velocity it is assumed to be described by an ergodic process. Consequently, the average operator can be interchanged with the mean integral value (in time) or the arithmetic mean if the acquired data are discrete. By applying now the Reynolds decomposition to the instantaneous flow:

$$u(\mathbf{s}, t) = \langle u \rangle(\mathbf{s}) + u'(\mathbf{s}, t) \quad (\text{B.6})$$

where the mean flow is assumed to be of the form $\langle u \rangle = (U(y), 0, 0)$. The effect of streamwise variations has not considered here because the y -variations are much faster than the x ones. The streamwise velocity standard deviation $\sqrt{\sigma^2(u)}$ (also called rms) is also assumed to be a function of y only with no spanwise dependence and negligible x variation.

It is possible to average equation B.5 in order to obtain the experimental mean velocity

$$\left\langle \left(\frac{1}{L} \int_{[-\frac{L}{2}, \frac{L}{2}]} u^n(\mathbf{s}) ds \right)^{1/n} \right\rangle = \langle f[e_w(t)] \rangle \quad (\text{B.7})$$

It is useful at this point, to find a simplifying formula to linearize the term inside the brackets:

$$\begin{aligned} \left[\frac{1}{L} \int_{[-\frac{L}{2}, \frac{L}{2}]} (1 + f(s))^n ds \right]^{1/n} &= \left[\frac{1}{L} \int_{[-\frac{L}{2}, \frac{L}{2}]} 1 + nf(s) ds + o(f) \right]^{1/n} = \\ &= \left[1 + \frac{n}{L} \int_{[-\frac{L}{2}, \frac{L}{2}]} f(s) ds + o(f) \right]^{1/n} = \\ &= 1 + \frac{1}{L} \int_{[-\frac{L}{2}, \frac{L}{2}]} f(s) ds + o(f) \quad (\text{B.8}) \end{aligned}$$

The application of the simplification B.8 does not consider the non-linearities of the power law expression, which becomes the same of the one with $n = 1$. By expanding equation B.8 up to the order f^2 , second order terms will appear and

velocity fluctuations must be therefore included. Also, to be consistent with the order analysis, the other velocity components v and w should be included, making the formulation more complex and less useful. Therefore we will keep the approximation B.8 carrying with each expression the extra terms in the form of the Landau term $o(\cdot)$.

The term inside the brackets can be simplified by applying the Reynolds decomposition (B.6), where the function $\langle u \rangle(\mathbf{s})$ can be approximated as:

$$\langle u \rangle(\mathbf{s}) = \langle u \rangle(\mathbf{x}_0) + s \left(\frac{\partial \langle u \rangle}{\partial \mathbf{w}} \right)_{\mathbf{x}_0} + \frac{s^2}{2} \left(\frac{\partial^2 \langle u \rangle}{\partial \mathbf{w}^2} \right)_{\mathbf{x}_0} + o(s^2) \quad (\text{B.9})$$

which can be re-written as:

$$\langle u \rangle(\mathbf{s}) = U_0 (1 + s\varepsilon\beta + s^2\varepsilon^2\theta) + o(\varepsilon^2) \quad (\text{B.10})$$

where $\beta = \frac{1}{U_0} \left(\frac{\partial \langle u \rangle}{\partial y} \right)_{\mathbf{x}_0}$, $\theta = \frac{1}{2U_0} \left(\frac{\partial^2 \langle u \rangle}{\partial y^2} \right)_{\mathbf{x}_0}$ and $U_0 = U(y_0)$. Indeed:

$$u(\mathbf{s}, t) = U_0 \left(1 + s\varepsilon\beta + s^2\varepsilon^2\theta + \frac{u'(\mathbf{s}, t)}{U_0} \right) + o(\varepsilon^2) \quad (\text{B.11})$$

To proceed forward the approximation $u'/U_0 \ll 1$ is done here. This approximation is valid outside the buffer layer region, while it is questionable inside this region because the ratio of the two quantities rises up to 0.4 (Alfredsson *et al.* 1988). By substituting now the expression B.11 into equation B.7, and by using the simplifying formula B.8, it is possible to find:

$$U_0 \left(1 + \varepsilon^2\theta \frac{L^2}{12} \right) + o\left(\varepsilon^3, \frac{u'}{U_0}\right) = \langle f[e_w(t)] \rangle \quad (\text{B.12})$$

which means that, with the assumed local linear velocity profile, the hot-wire output is related to the velocity on the wire middle-point, with a small correction due to the probe angle. The even exponent of such error it is not surprising because the error in the mean quantities due to the probe angle is an even function of the probe angle itself and, therefore, no ε or ε^3 should appear.

To determine the variance of the hot-wire signal, the average operator is applied to the square of B.5 (simplified with B.8) minus equation B.12, namely:

$$\frac{1}{L^2} \left\langle \left(\int_{[-\frac{L}{2}, \frac{L}{2}]} u'(\mathbf{s}, t) ds \right)^2 \right\rangle + o\left(\varepsilon^2, \left(\frac{u'}{U_0}\right)^2\right) = \langle (f[e_w(t)] - \langle f[e_w(t)] \rangle)^2 \rangle \quad (\text{B.13})$$

The RHS will be renamed $\sigma^2[f(e_w)]$ since it is the variance of $f(e)$. After the multiplication of the integrals, equation B.13 becomes:

$$\frac{1}{L^2} \int_{[-\frac{L}{2}, \frac{L}{2}]^2} \langle u'(\mathbf{s}, t) u'(\mathbf{q}, t) \rangle dsdq + o\left(\varepsilon^2, \left(\frac{u'}{U_0}\right)^2\right) = \sigma^2[f(e_w)] \quad (\text{B.14})$$

The two-point correlation $\langle u'(\mathbf{s}, t) u'(\mathbf{q}, t) \rangle$ can be re-expressed by using the two-point correlation coefficient $C_{11}(s, q)$ which will be defined as:

$$C_{11}(\mathbf{s}, \mathbf{q}) = \frac{\langle u'(\mathbf{s}, t) u'(\mathbf{q}, t) \rangle}{\sqrt{\langle u'^2(\mathbf{s}, t) \rangle} \sqrt{\langle u'^2(\mathbf{q}, t) \rangle}} \quad (\text{B.15})$$

The correlation coefficient can be approximated locally by a Taylor expansion around the wire middle-point \mathbf{x}_0 . The coefficients of this expansion can be further simplified by applying the three important properties of the C_{11} :

- boundedness: $|C_{11}(\mathbf{s}, \mathbf{q})| \leq 1 \forall (\mathbf{s}, \mathbf{q})$
- simmetry: $C_{11}(\mathbf{s}, \mathbf{q}) = C_{11}(\mathbf{q}, \mathbf{s}) \forall (\mathbf{s}, \mathbf{q})$
- locality: $C_{11}(\mathbf{s}, \mathbf{s}) = 1 \forall \mathbf{s}$

To facilitate the expression of C_{11} , a change of variables can be used as:

$$(\mathbf{s}_m, \mathbf{r}) = \left(\mathbf{x}_0 + \frac{s+q}{2} \mathbf{w}, (s-q) \mathbf{w} \right)$$

where \mathbf{s}_m and \mathbf{r} are the mid-point and vector between \mathbf{s} and \mathbf{q} , respectively. The requirements becomes:

- boundedness: $|C_{11}(\mathbf{s}_m, \mathbf{r})| \leq 1 \forall (\mathbf{s}_m, \mathbf{r})$
- simmetry: $C_{11}(\mathbf{s}_m, \mathbf{r}) = C_{11}(\mathbf{s}_m, -\mathbf{r}) \forall (\mathbf{s}_m, \mathbf{r})$
- locality: $C_{11}(\mathbf{s}_m, \mathbf{0}) = 1 \forall \mathbf{s}_m$

Now, a polynomial expression of C_{11} can be found by means of a Taylor expansion around the point $(\mathbf{x}_0, \mathbf{0})$. Up to the fourth order, the only polynomial which satisfies the above requirements is:

$$\begin{aligned} C_{11}(\mathbf{s}_m, \mathbf{r}) = & 1 + \sum_{i,j} A_{ij} r_i r_j + \sum_{i,j,k} B_{ij,k} r_i r_j (\mathbf{s}_m - \mathbf{x}_0)_k \\ & + \sum_{i,j,k,m} C_{ij,km} r_i r_j (\mathbf{s}_m - \mathbf{x}_0)_k (\mathbf{s}_m - \mathbf{x}_0)_m + \sum_{i,j,k,m} D_{ijklm} r_i r_j r_k r_m \end{aligned} \quad (\text{B.16})$$

where:

$$\begin{aligned} A_{ij} &= \frac{1}{2} \left(\frac{\partial^2 C_{11}}{\partial r_i \partial r_j} \right)_{\mathbf{x}_0} \\ B_{ij,k} &= \frac{1}{6} \left(\frac{\partial^3 C_{11}}{\partial r_i \partial r_j \partial s_{m,k}} \right)_{\mathbf{x}_0} \end{aligned} \quad (\text{B.17})$$

$$\begin{aligned} C_{ij,km} &= \frac{1}{24} \left(\frac{\partial^4 C_{11}}{\partial r_i \partial r_j \partial s_{m,k} \partial s_{m,m}} \right)_{\mathbf{x}_0} \\ D_{ijklm} &= \frac{1}{24} \left(\frac{\partial^4 C_{11}}{\partial r_i \partial r_j \partial r_k \partial r_m} \right)_{\mathbf{x}_0} \end{aligned} \quad (\text{B.18})$$

The above coefficients can be simplified by considering that:

- There is no x dependence in the present formulation;
- Due to the homogeneity in the z -direction all the derivatives in $s_{m,3}$ are zero;
- Due to the symmetry of the turbulent field to the reflections in the xy -plane, all the odd derivative in r_3 are zero.

It is possible now to express the two-point correlation coefficient as:

$$C_{11}(\mathbf{s}, \mathbf{q}) = 1 + (s - q)^2 \left[\Gamma_2 + \Gamma_3 (s + q) + \Gamma_{4,1} (s + q)^2 + \Gamma_{4,2} (s - q)^2 \right] \quad (\text{B.19})$$

where

$$\begin{aligned} \Gamma_2 &= A_{33} + A_{22}\varepsilon^2 \\ \Gamma_3 &= \frac{3\varepsilon}{2} (B_{33,2} + B_{22,2}\varepsilon^2) \\ \Gamma_{4,1} &= \frac{3\varepsilon^2}{2} (C_{33,22} + C_{22,22}\varepsilon^2) \\ \Gamma_{4,2} &= D_{3333} + 6D_{3322}\varepsilon^2 + D_{2222}\varepsilon^4 \end{aligned} \quad (\text{B.20})$$

$$(\text{B.21})$$

The coefficient Γ_2 has special properties since it must be negative everywhere to ensure the boundedness and it is related to the transverse Taylor microscale λ_g^2 :

$$\Gamma_2 = A_{33} + o(\varepsilon) = \frac{1}{2} \left(\frac{\partial^2 C_{11}}{\partial r_3^2} \right) + o(\varepsilon) = -\frac{1}{\lambda_g^2} + o(\varepsilon) \quad (\text{B.22})$$

Going back to equation B.14, the standard deviations of the local velocity can be expressed with a procedure analogous to the one used for equations B.9 and B.10, namely:

$$\sqrt{\langle u'^2(\mathbf{s}, t) \rangle} = \sqrt{\langle u'^2 \rangle_0} (1 + s\varepsilon\gamma + s^2\varepsilon^2\omega) + o(\varepsilon^2) \quad (\text{B.23})$$

$$\text{with } \gamma = \frac{1}{\sqrt{\langle u'^2 \rangle_0}} \left(\frac{\partial \sqrt{\langle u'^2 \rangle}}{\partial y} \right)_{\mathbf{x}_0}, \quad \omega = \frac{1}{2\sqrt{\langle u'^2 \rangle_0}} \left(\frac{\partial^2 \sqrt{\langle u'^2 \rangle}}{\partial y^2} \right)_{\mathbf{x}_0}$$

and $\sqrt{\langle u'^2 \rangle_0} = \sqrt{\langle u'^2(\mathbf{x}_0, t) \rangle}$.

Equation B.14 becomes:

$$\frac{\langle u'^2 \rangle_0}{L^2} \int_{[-\frac{L}{2}, \frac{L}{2}]^2} \frac{\sqrt{\langle u'^2(\mathbf{s}, t) \rangle} \sqrt{\langle u'^2(\mathbf{q}, t) \rangle}}{\langle u'^2 \rangle_0} C_{11}(s, q) dsdq + o(\varepsilon) = \sigma^2 [f(e_w)] \quad (\text{B.24})$$

by performing the integration:

$$\langle u'^2 \rangle_0 (1 + F_0 + \varepsilon^2 F_2) + o(\varepsilon^2) = \sigma^2 [f(e_w)] \quad (\text{B.25})$$

in which:

$$\begin{aligned}
F_0 &= \frac{1}{6}A_{33}L^2 + \frac{1}{15}D_{3333}L^4 \\
F_2 &= \frac{L^2}{2520}(420(A_{22} + \omega) + 7L^2(144D_{3322} + 6\gamma B_{33,2} + 14\omega A_{33} - 5\gamma^2 A_{33})) + \\
&\quad + 3L^4 D_{3333}(16\omega - 7\gamma^2)
\end{aligned}
\tag{B.26}$$

Which means that the measured rms is affected by a factor

$$\sqrt{1 + F_0 + \varepsilon^2 F_2}$$

which in case of isotropic turbulence becomes

$$\sqrt{1 - \left(\frac{L}{6\lambda_g}\right)^2 + \frac{1}{360} \frac{\partial^4 C_{11}}{\partial r_z^4} L^4}$$

which is similar to the one proposed by Frenkiel (1949) in isotropic conditions. In that relationship, the first order correction is the same, while the second order has a factor of $\frac{1}{120}$ instead than our $\frac{1}{360}$ due to the different derivation method.

B.3. Numerical results

To investigate the effect of the presented expression, data from two DNS will be used. The numerical simulations have been performed on a channel flow with half height h at $Re_\tau = u_\tau h / \nu = 300$ and $Re_\tau = 550$. The simulation at $Re_\tau = 300$ has $Re = hU_b / \nu = 10000$ with a domain extension $(L_x, L_y, L_z) = (2\pi h, 2h, \pi h)$. The simulation at $Re_\tau = 550$ has $Re = hU_b / \nu = 10000$ with a domain extension $(L_x, L_y, L_z) = (8\pi h, 2h, 4\pi h)$.

B.3.1. Effect of the wire spatial resolution

In this first section the probe angle will be assumed to be zero in order to investigate the wire length filtering effect. The greatest effect in the turbulent quantities is usually observed in the streamwise velocity rms profile. As an example, figure B.2 reports the effect of the wire length in the squared rms for the simulation with the highest Re_τ . In the case of parallel wire the expression of F_0 in B.26 has been further expanded as:

$$F_0 = \frac{1}{6}A_{33}L^2 + \frac{1}{15}D_{3333}L^4 + \frac{1}{28}G_{333333}L^6$$

to include the effect of $G_{333333} = \frac{1}{6!} \frac{\partial^6 C_{11}}{\partial r_z^6}$. This extends the precision of the estimated C_{11} expression and, therefore, the validity of the Taylor expansion towards higher L^+ : it was observed that the use of an expansion up to the 4th order term caused the divergence of the correction for $L^+ > 30$. It is worth to note from figure B.2 that the maximum of u'^2/u_τ^2 is strongly affected by the

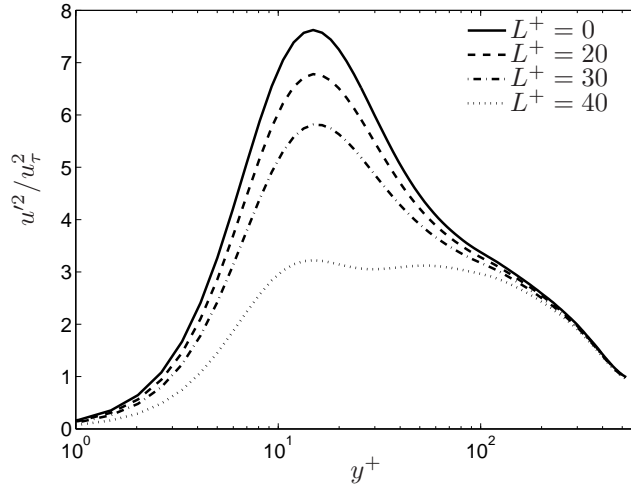


FIGURE B.2. u'^2/u_τ^2 distribution for different wire lengths L^+ at $Re_\tau = 550$.

wire length and, also, for $L^+ = 40$ a second peak in the profile appears which is not observable in the original profile. We are not able to state whether or not this second peak is due to the wire resolution, since we will need more higher order derivatives for such high L^+ , but the trend indicates the formation of this second peak which agrees with the conclusions of other experiments (Hutchins & Marusic 2007, for instance).

The comparison of the above expression of F_0 with the 6^{th} order term with the simplified one with only the 2^{nd} order term is reported in figure B.3 where the same profiles are compared. While for $L^+ = 20$ the differences are small, they become relevant for higher L^+ , (especially for $y^+ \approx 15$) and hide the second peak at $L^+ = 40$. Nevertheless, even such simple expression is able to find a leading order correction to determine the main reduction in the rms.

The effect of the wire length on the maximum squared rms $(u'^2/u_\tau^2)_m$ is reported in figure B.4 together with the empirical fit proposed by many authors, as well as with a quadratic fit that the present author did with the collection of data made by Suzuki & Kasagi (1992). The agreement between the complete theory (including the 6^{th} order term) and the latter quadratic fit is remarkable up to $L^+ = 30$ and it is comparable to the other laws proposed by Ligrani & Bradshaw (1987) and Hutchins *et al.* (2009), even if they have been found from experiments with higher Reynolds numbers. The correction with the 2^{nd} derivative only is lower than the one with the higher order terms but, on the other hand, it certainly gives a first reasonable approximation of it.

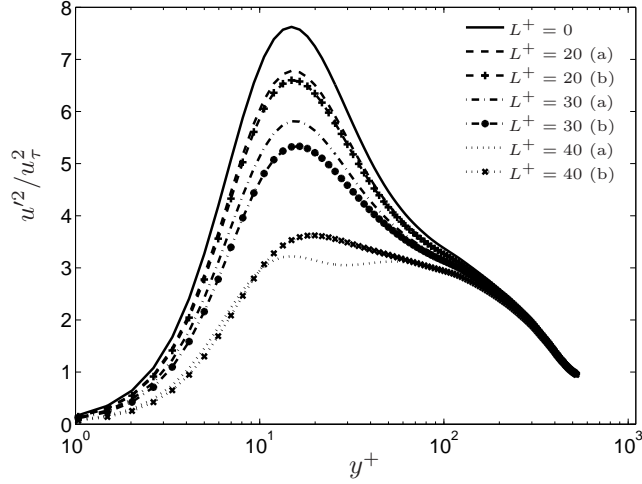


FIGURE B.3. u'^2/u_τ^2 distribution for different wire lengths L^+ at $Re_\tau = 550$ with (a) and without (b) the 4th and 6th order derivative terms.

B.3.2. Estimation of the Taylor transverse microscale in Turbulent Wall Bounded Flows

As shown in the section B.2, the most important contribution to the coefficient Γ_2 is given by the term,

$$\frac{1}{2} \left(\frac{\partial^2 C_{11}}{\partial r_z^2} \right)_{\mathbf{x}_0} \quad (\text{B.27})$$

which represents the effects of the spanwise resolution of the hot wire. Since this term in homogeneous isotropic turbulence is related to the transverse Taylor microscale λ_g (c.f. equation B.22), a well-defined scaling is expected. In isotropic turbulence, the scale λ_g can be related to the Kolmogorov scale η in the form,

$$\lambda_g = \sqrt{10} \eta^{2/3} L_c^{1/3} \quad (\text{B.28})$$

where L_c is a length scale characterizing the large eddies. Even if wall-turbulence is an intrinsically anisotropic and inhomogeneous phenomenon, an isotropic recovery at the small scales of the logarithmic and bulk region is expected, at least for large Reynolds number. Therefore, a scaling behavior similar to B.28 is expected to hold.

According to the classical theory, the logarithmic layer is an equilibrium region where global turbulent production and dissipation balance. With this assumptions, since the mean shear S can be written as $S \approx u^*/(\kappa y)$, it is possible to find that the local dissipation $\langle \epsilon \rangle(y)$ can be estimated as $\langle \epsilon \rangle(y) = u'^3/(\kappa y)$, where κ is the Karman constant. Therefore, the Kolmogorov scale

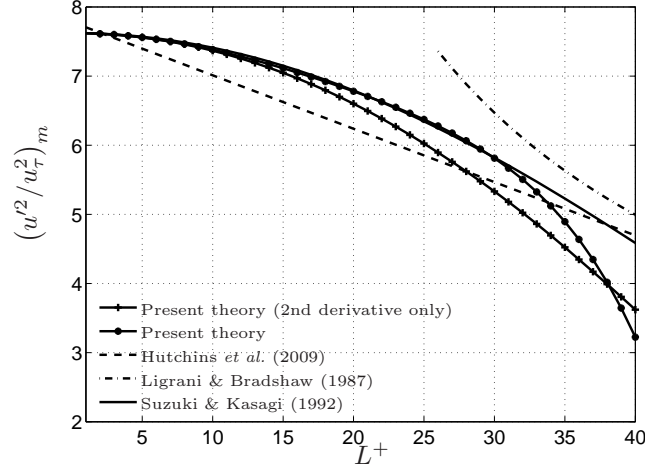


FIGURE B.4. Effect of the wire length L^+ on the maximum measured value of u'^2/u_τ^2 for $Re_\tau = 550$. Here the present theory is compared to the fits proposed by Hutchins *et al.* (2009), by Ligrani & Bradshaw (1987) and by Suzuki & Kasagi (1992).

$\eta = (\nu^3/\epsilon)^{1/4}$ is expected to scale with the wall-distance as $\eta(y) \propto (ky)^{1/4}$, and the shear scale $L_s = \sqrt{\langle \epsilon \rangle / S^3}$, which can be considered as the length scale characterizing the large eddies, is expected to scale with the wall-distance as $L_s \propto (\kappa y)$. Substituting this two expression in equation B.28, a scaling with the wall-distance for the transverse Taylor microscale λ_g can be obtained as,

$$\lambda_g = A (ky)^{1/2} \quad (\text{B.29})$$

where A is a constant. If this is true, the wall-distance scaling of the term B.27, responsible for the spanwise resolution effects of the hot-wire, leads to:

$$\frac{1}{2} \left(\frac{\partial^2 C_{11}}{\partial r_z^2} \right)_{\mathbf{x}_0} = -\frac{1}{C^2(ky)} \quad (\text{B.30})$$

The numerical investigation of relation B.30, shown in figure B.5, exhibits a good agreements between the theoretical and the numerical behavior. This relation could be very useful for the assessment of the spatial resolution errors which affect hot-wire measurements in wall-bounded turbulent flows.

To practically estimate the constant A the following approach is proposed: from a single probe, and by using the Taylor hypothesis of frozen turbulence,

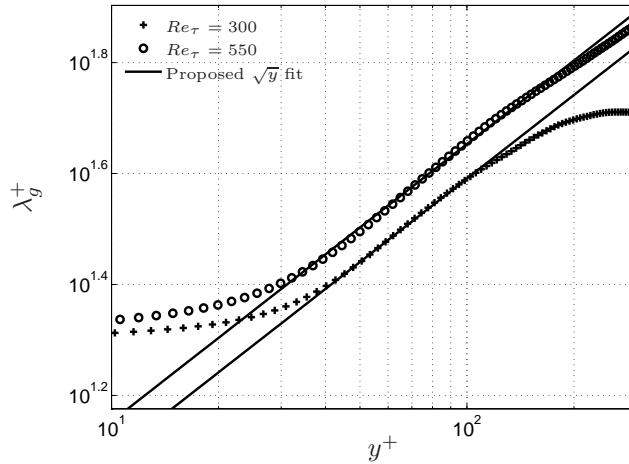


FIGURE B.5. Comparison between the calculated value of the Taylor transverse microscale λ_g^+ with the one predicted by the law $\lambda_g^+ \propto \sqrt{y^+}$, for two Re_τ .

it is possible to estimate the longitudinal Taylor microscale λ_f from the longitudinal autocorrelation function F_{11} :

$$\lambda_f = \left(-\frac{1}{2} \frac{\partial F_{11}}{\partial r_x} \right)^{-1/2}. \quad (\text{B.31})$$

Since, for isotropic turbulence, the transverse Taylor microscale λ_g is strictly related to the longitudinal Taylor microscale λ_f with the relation,

$$\lambda_g = \frac{\lambda_f}{\sqrt{2}} \quad (\text{B.32})$$

it is possible to measure a point of the curve defined by relation B.30 and then evaluate the constant of proportionality A .

To assess the potential of this estimation, figure B.6 reports the streamwise velocity rms profile with the correction calculated from the complete theory and with the approximate one, which comprises only the 2^{nd} order term in F_0 where the Taylor transverse microscale has been estimated as $\lambda_g = A\sqrt{y^+}$ (where $A = 4.5$ for $Re_\tau = 550$). The good agreement between the two formulations for $y^+ > 30$ which underlines that the proposed methodology is highly efficient in wall bounded turbulent flows.

B.3.3. Effect of the probe angle

The effect of the probe angle is now considered. Figure B.7 shows the effect of a misalignment of $\varepsilon = 5^\circ$ with respect to the wall. Such misalignment is

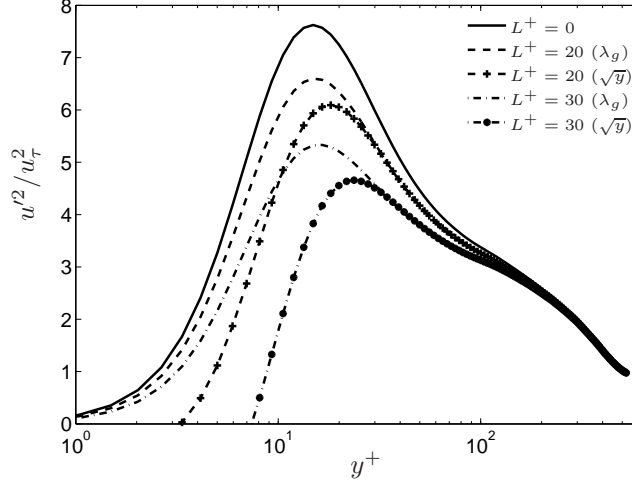


FIGURE B.6. u'^2/u_τ^2 distribution for different wire lengths L^+ at $Re_\tau = 550$. The Taylor microscale has been here calculated from the numerical simulation and estimated from the proposed $\lambda_g \propto \sqrt{y}$ scaling.

inside the experimental accuracy used to locate the hot wire, unless optical methods are applied to fix it. As expected, the mean streamwise velocity is almost unaffected by this error far from the wall. However, once the wall is approached this becomes sensible and of the order of -0.5% of the local mean velocity. It is clear from B.12 that this error source increases by increasing the wire length, but it is almost negligible in experiments for conventional hot-wires.

The streamwise velocity rms relative error profile is reported in figure B.8. Here the corrective term is the F_2 function expressed in equation B.26, where only an expansion up to the 4th order term has been used. Again, far from the wall only the filtering effect of the wire affects the measured rms, while the situation changes dramatically for $y^+ < 5$, where the rms rises abruptly. To further appreciate such differences, the rms profile is reported in figure B.9 for $L^+ = 30$ and for different values of ε . for $y^+ > 15$ there is no difference even for $\varepsilon = 15^\circ$, while in the viscous sublayer and initial buffer region there is an increasing error effect with the probe angle, especially for the two highest probe angles. It can be expected, therefore, that the probe angle is not a serious issue if we are concerned with regions far from the wall (namely $y^+ > 15^\circ$), but becomes a crescent error source as soon as the probe approaches the wall.

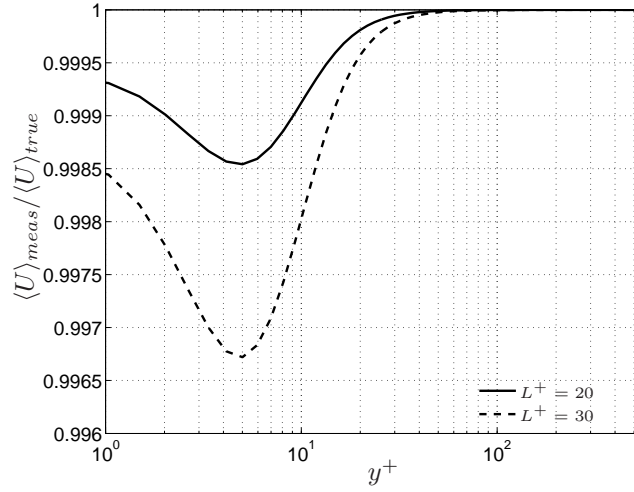


FIGURE B.7. Relative error in the mean streamwise velocity at $Re_\tau = 550$ due to the probe angle for $\varepsilon = 5^\circ$.

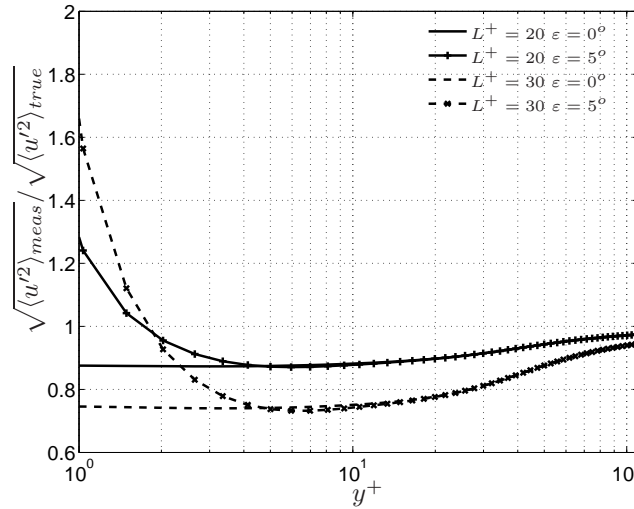


FIGURE B.8. Relative error in the rms of the streamwise velocity at $Re_\tau = 550$ due to the probe angle for $\varepsilon = 5^\circ$.

Acknowledgements

The DNS data and the proposed scaling for the Taylor microscale have been provided by A.Cimarelli which is greatly acknowledged.

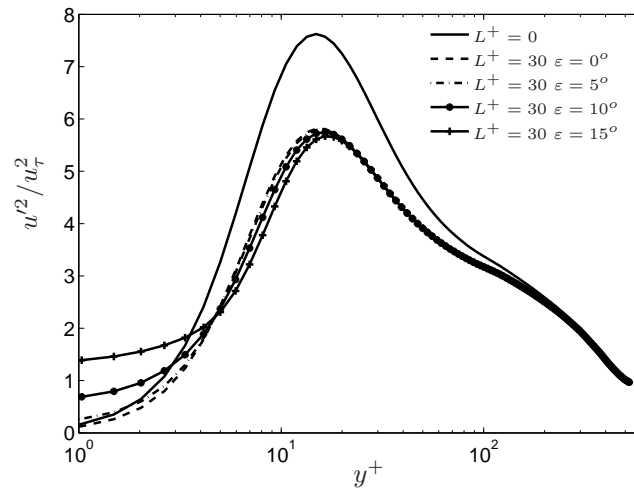


FIGURE B.9. u'^2/u_τ^2 distribution for $L^+ = 30$ at $Re_\tau = 550$ for different probe angles ε .

APPENDIX C

Effect of position uncertainty on the estimation of the Kármán constant for turbulent boundary layers

Let's assume that the probe position is known inside a certain error that can be quantified in wall units as ε^+ , while the friction velocity u_τ is known with infinite precision by means of separate measurements (namely oil film interferometry or the Preston tube method). The displacement error ε^+ is assumed to be a systematic error independent from the actual y position and, therefore, constant. This implies that:

$$y_{meas}^+ = y^+ + \varepsilon^+$$

Let's assume that the probe measured inside the logarithmic region of the velocity profile in a turbulent boundary layer a set of points, all satisfying the logarithmic law:

$$U^+ = \frac{1}{\kappa} \ln(y^+) + B$$

Since the friction velocity is known, $U_{meas}^+(y^+ + \varepsilon^+) = U^+(y^+)$. To determine the Kármán constant value, the experimentalist will try to fit the measurements with the relation:

$$U_{meas}^+ = \frac{1}{\kappa_\varepsilon} \ln(y_{meas}^+) + B_\varepsilon = \frac{1}{\kappa_\varepsilon} \ln(y^+ + \varepsilon^+) + B_\varepsilon = U^+ \quad (C.1)$$

where κ_ε and B_ε are the estimated Kármán constant and the shift of the logarithmic law.

C.1. Continuous approach

In the hypothesis of a continuous distribution of points ($N \rightarrow +\infty$), the coefficients κ_ε and B_ε of equation C.1 can be found by a least square technique which minimizes the functional:

$$F(\kappa_\varepsilon^{-1}, B_\varepsilon) = \frac{1}{2} \int_{y_{min}^+}^{y_{max}^+} \left(\frac{1}{\kappa_\varepsilon} \ln(y^+ + \varepsilon^+) + B_\varepsilon - \frac{1}{\kappa} \ln(y^+) - B \right)^2 dy^+ \quad (C.2)$$

through the solution of equations:

$$\begin{cases} 0 = \frac{\partial F}{\partial \kappa_\varepsilon^{-1}} = \int_{y_{min}^+}^{y_{max}^+} \left(\frac{1}{\kappa_\varepsilon} \ln(y^+ + \varepsilon^+) + B_\varepsilon - \frac{1}{\kappa} \ln(y^+) \ln - B \right) \ln(y^+ + \varepsilon^+) dy^+ \\ 0 = \frac{\partial F}{\partial B_\varepsilon} = \int_{y_{min}^+}^{y_{max}^+} \left(\frac{1}{\kappa_\varepsilon} \ln(y^+ + \varepsilon^+) + B_\varepsilon - \frac{1}{\kappa} \ln(y^+) \ln - B \right) dy^+ \end{cases} \quad (C.3)$$

with the hypothesis of small error $\varepsilon^+ \ll y^+$ in the logarithmic region, the logarithmic term can be approximated as:

$$\ln(y^+ + \varepsilon^+) = \ln(y^+) + \ln\left(1 + \frac{\varepsilon^+}{y^+}\right) \simeq \ln(y^+) + \frac{\varepsilon^+}{y^+}$$

By neglecting second order terms, equations C.3 becomes now:

$$\begin{cases} \frac{1}{\kappa_\varepsilon} (C_1 + 2\varepsilon^+ C_2) + B_\varepsilon (C_3 + \varepsilon^+ C_4) = \frac{1}{\kappa} (C_1 + \varepsilon^+ C_2) + B (C_3 + \varepsilon^+ C_4) \\ \frac{1}{\kappa_\varepsilon} (C_3 + \varepsilon^+ C_4) + B_\varepsilon (C_5) = \frac{1}{\kappa} (C_3) + B (C_5 + \varepsilon^+ C_4) \end{cases} \quad (C.4)$$

where:

$$\begin{aligned} C_1 &= \int_{y_{min}^+}^{y_{max}^+} \ln^2(y^+) dy^+ = [y^+ (\ln^2(y^+) - 2\ln(y^+) + 2)]_{y_{min}^+}^{y_{max}^+} \\ C_2 &= \int_{y_{min}^+}^{y_{max}^+} \frac{\ln(y^+)}{y^+} dy^+ = \left[\frac{1}{2} \ln^2(y^+) \right]_{y_{min}^+}^{y_{max}^+} \\ C_3 &= \int_{y_{min}^+}^{y_{max}^+} \ln(y^+) dy^+ = [y^+ (\ln(y^+) - 1)]_{y_{min}^+}^{y_{max}^+} \\ C_4 &= \int_{y_{min}^+}^{y_{max}^+} \frac{1}{y^+} dy^+ = [\ln(y^+)]_{y_{min}^+}^{y_{max}^+} \\ C_5 &= \int_{y_{min}^+}^{y_{max}^+} dy^+ = [y^+]_{y_{min}^+}^{y_{max}^+} \end{aligned}$$

are coefficients which depend on the width on the logarithmic region (namely y_{min}^+ and y_{max}^+). While y_{min}^+ could be approximately 100 for high enough Reynolds number, the y_{max}^+ value is still a strong function of the Reynolds number and of the outer conditions.

The system C.4 can be re-written in matricial form:

$$\begin{bmatrix} \frac{1}{\kappa_\varepsilon} \\ B_\varepsilon \end{bmatrix} = \begin{bmatrix} C_1 + 2\varepsilon^+ C_2 & C_3 + \varepsilon^+ C_4 \\ C_3 + \varepsilon^+ C_4 & C_5 \end{bmatrix}^{-1} \begin{bmatrix} C_1 + \varepsilon^+ C_2 & C_3 + \varepsilon^+ C_4 \\ C_3 & C_5 \end{bmatrix} \begin{bmatrix} \frac{1}{\kappa} \\ B \end{bmatrix} \quad (C.5)$$

which has the following solution:

$$\frac{\kappa_\varepsilon}{\kappa} = \frac{1 + 2\varepsilon^+ K}{1 + \varepsilon^+ K} = 1 + \varepsilon^+ K + o(\varepsilon^+) \quad (C.6)$$

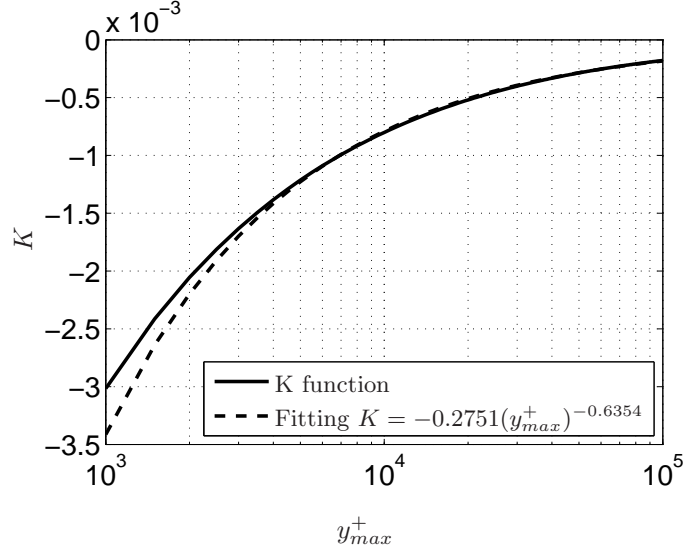


FIGURE C.1. K function distribution for various y_{max}^+ value with $y_{min}^+ = 100$.

where:

$$K = \frac{C_2 C_5 - C_3 C_4}{C_1 C_5 - C_3^2}$$

The coefficient K represents the sensibility of the κ_ε value to the error ε^+ and is a function of the Reynolds number through the value y_{max}^+ as depicted in figure C.1. A power law fitting function is proposed to calculate K from the knowledge of the outer boundary of the logarithmic region. Therefore the estimated Kármán constant has the following expression:

$$\kappa_\varepsilon \approx \kappa \left[1 - 0.2751 \varepsilon^+ (y_{max}^+)^{-0.6354} \right] \quad (C.7)$$

If we assume that the y_{max} value is almost $\frac{\delta}{10}$, then $y_{max}^+ \approx 0.1 \frac{u_\tau \delta}{\nu} = 0.1 Re_\tau$, where Re_τ is also known as the Kármán number. Therefore, equation C.7 can be re-written as:

$$\kappa_\varepsilon \approx \kappa \left[1 - 1.1882 Re_\tau^{-0.6354} \varepsilon^+ \right] \quad (C.8)$$

The effect of the displacement error ε^+ on the estimated Kármán constant can be further appreciated from figures C.2 where a value of $y_{max}^+ = 1000$ has been chosen being a reasonable value for most wind tunnels turbulent boundary layers. It is clear that an error of $\varepsilon^+ = \pm 10$ (ε should be around $150 \mu m$ for $u_\tau = 1 m/s$ and standard air as working fluid) will lead to an error in the estimated Kármán constant of the order of 3% which is quite high.

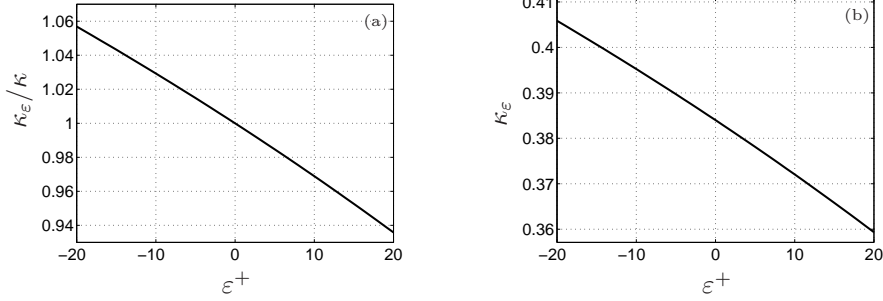


FIGURE C.2. (a) $\kappa_\varepsilon/\kappa$ (b) κ_ε (assumed $\kappa = 0.384$) variation for different ε^+ with $y_{max}^+ = 1000$.

C.2. Discrete approach

Usually, the experimentalist will collect a finite number of points to extrapolate the Kármán constant by means of a least square technique in order to minimize the following functional:

$$F(\kappa_\varepsilon^{-1}, B_\varepsilon) = \sum_{i=1}^N \left(\frac{1}{\kappa_\varepsilon} \ln(y_i^+ + \varepsilon_i^+) + B_\varepsilon - U^+(y_i^+) \right)^2 \quad (\text{C.9})$$

The minimum of equation C.9 will be obtained by calculating the derivative of C.9 and equating them to 0. After some algebra:

$$\begin{cases} \sum_{i=1}^N \left(\frac{1}{\kappa_\varepsilon} \ln(y_i^+ + \varepsilon_i^+) + B_\varepsilon \right) = \sum_{i=1}^N (U^+(y_i^+)) \\ \sum_{i=1}^N \left(\frac{1}{\kappa_\varepsilon} \ln^2(y_i^+ + \varepsilon_i^+) + B_\varepsilon \ln(y_i^+ + \varepsilon_i^+) \right) = \sum_{i=1}^N (U^+(y_i^+) \ln(y_i^+ + \varepsilon_i^+)) \end{cases} \quad (\text{C.10})$$

that can be expressed in matricial form:

$$\begin{bmatrix} \sum_{i=1}^N \ln(y_i^+ + \varepsilon_i^+) & N \\ \sum_{i=1}^N \ln^2(y_i^+ + \varepsilon_i^+) & \sum_{i=1}^N \ln(y_i^+ + \varepsilon_i^+) \end{bmatrix} \begin{bmatrix} \frac{1}{\kappa_\varepsilon} \\ B_\varepsilon \end{bmatrix} = \begin{bmatrix} \sum_{i=1}^N (U^+(y_i^+)) \\ \sum_{i=1}^N (U^+(y_i^+) \ln(y_i^+ + \varepsilon_i^+)) \end{bmatrix} \quad (\text{C.11})$$

and, by inverting the linear system:

$$\begin{bmatrix} \frac{1}{\kappa_\varepsilon} \\ B_\varepsilon \end{bmatrix} = \frac{1}{\Delta} \begin{bmatrix} \sum_{i=1}^N \ln(y_i^+ + \varepsilon_i^+) & -N \\ -\sum_{i=1}^N \ln^2(y_i^+ + \varepsilon_i^+) & \sum_{i=1}^N \ln(y_i^+ + \varepsilon_i^+) \end{bmatrix} \begin{bmatrix} \sum_{i=1}^N (U^+(y_i^+)) \\ \sum_{i=1}^N (U^+(y_i^+) \ln(y_i^+ + \varepsilon_i^+)) \end{bmatrix} \quad (\text{C.12})$$

where

$$\Delta = \left[\sum_{i=1}^N \ln(y_i^+ + \varepsilon_i^+) \right]^2 - N \sum_{i=1}^N \ln^2(y_i^+ + \varepsilon_i^+)$$

Since the measurement points are in the logarithmic region $U_i^+ = \frac{1}{\kappa} \ln(y_i^+) + B$ and the second matrix of the RHS of equation C.12 becomes:

$$\begin{bmatrix} \sum_{i=1}^N (U^+(y_i^+)) \\ \sum_{i=1}^N (U^+(y_i^+) \ln(y_i^+ + \varepsilon_i^+)) \end{bmatrix} = \begin{bmatrix} \sum_{i=1}^N \ln(y_i^+) & N \\ \sum_{i=1}^N \ln(y_i^+) \ln(y_i^+ + \varepsilon_i^+) & \sum_{i=1}^N \ln(y_i^+ + \varepsilon_i^+) \end{bmatrix} \begin{bmatrix} \frac{1}{\kappa} \\ B \end{bmatrix} \quad (\text{C.13})$$

Hence, the relation between κ_ε and κ will be:

$$\frac{1}{\kappa_\varepsilon} = \frac{1}{\Delta} \left[\sum_{i=1}^N \ln(y_i^+ + \varepsilon_i^+) \sum_{i=1}^N \ln(y_i^+) - N \sum_{i=1}^N \ln(y_i^+) \ln(y_i^+ + \varepsilon_i^+) \right] \frac{1}{\kappa} \quad (\text{C.14})$$

with the hypothesis of small error $\varepsilon^+ \ll y^+$ in the logarithmic region, the logarithmic term will be approximated as:

$$\ln(y^+ + \varepsilon^+) = \ln(y^+) + \ln\left(1 + \frac{\varepsilon^+}{y^+}\right) \simeq \ln(y^+) + \frac{\varepsilon^+}{y^+}$$

With this approximation equation C.14 becomes:

$$\frac{1}{\kappa_\varepsilon} = \frac{1}{\Delta'} \left\{ \left[\sum_{i=1}^N \ln(y_i^+) \right]^2 + \sum_{i=1}^N \frac{\varepsilon_i^+}{y_i^+} \sum_{i=1}^N \ln(y_i^+) - N \sum_{i=1}^N \ln^2(y_i^+) - N \sum_{i=1}^N \frac{\varepsilon_i^+}{y_i^+} \ln(y_i^+) \right\} \frac{1}{\kappa} \quad (\text{C.15})$$

with:

$$\begin{aligned} \Delta' &= \left[\sum_{i=1}^N \ln(y_i^+) \right]^2 + \left[\sum_{i=1}^N \frac{\varepsilon_i^+}{y_i^+} \right]^2 + 2 \sum_{i=1}^N \ln(y_i^+) \sum_{i=1}^N \frac{\varepsilon_i^+}{y_i^+} - N \sum_{i=1}^N \ln^2(y_i^+) - \\ &\quad - N \sum_{i=1}^N \left(\frac{\varepsilon_i^+}{y_i^+} \right)^2 - 2N \sum_{i=1}^N \frac{\varepsilon_i^+}{y_i^+} \ln(y_i^+) \simeq \\ &\simeq \left[\sum_{i=1}^N \ln(y_i^+) \right]^2 + 2 \sum_{i=1}^N \ln(y_i^+) \sum_{i=1}^N \frac{\varepsilon_i^+}{y_i^+} - N \sum_{i=1}^N \ln^2(y_i^+) - 2N \sum_{i=1}^N \frac{\varepsilon_i^+}{y_i^+} \ln(y_i^+) \end{aligned}$$

by neglecting the second order terms and by dividing both numerator and denominator by $\left[\sum_{i=1}^N \ln(y_i^+) \right]^2 - N \sum_{i=1}^N \ln^2(y_i^+)$, it will be possible to obtain:

$$\frac{1}{\kappa_\varepsilon} = \frac{1 + \frac{\sum_{i=1}^N \frac{\varepsilon_i^+}{y_i^+} \sum_{i=1}^N \ln(y_i^+) - N \sum_{i=1}^N \frac{\varepsilon_i^+}{y_i^+} \ln(y_i^+)}{\left[\sum_{i=1}^N \ln(y_i^+) \right]^2 - N \sum_{i=1}^N \ln^2(y_i^+)}}{1 + \frac{2 \sum_{i=1}^N \ln(y_i^+) \sum_{i=1}^N \frac{\varepsilon_i^+}{y_i^+} - 2N \sum_{i=1}^N \frac{\varepsilon_i^+}{y_i^+} \ln(y_i^+)}{\left[\sum_{i=1}^N \ln(y_i^+) \right]^2 - N \sum_{i=1}^N \ln^2(y_i^+)}} \frac{1}{\kappa} \quad (\text{C.16})$$

$$\frac{\kappa}{\kappa_\varepsilon} = 1 + \frac{N \sum_{i=1}^N \frac{\varepsilon_i^+}{y_i^+} \ln(y_i^+) - \sum_{i=1}^N \frac{\varepsilon_i^+}{y_i^+} \sum_{i=1}^N \ln(y_i^+)}{\left[\sum_{i=1}^N \ln(y_i^+) \right]^2 - N \sum_{i=1}^N \ln^2(y_i^+)} = \quad (\text{C.17})$$

if $\varepsilon_i^+ = \varepsilon_m^+$, where ε_m^+ is a constant error, the above expression will become:

$$\frac{\kappa}{\kappa_\varepsilon} = 1 + \varepsilon_m^+ \frac{N \sum_{i=1}^N \frac{1}{y_i^+} \ln(y_i^+) - \sum_{i=1}^N \frac{1}{y_i^+} \sum_{i=1}^N \ln(y_i^+)}{\left[\sum_{i=1}^N \ln(y_i^+) \right]^2 - N \sum_{i=1}^N \ln^2(y_i^+)}$$

which is the equivalent of equation C.6 with a the discrete set of points. Differently from before, the error ε_i^+ has not been assumed constant over all the velocity profile, in order to obtain an equation which was more general. It is certain that these relations are sensible on the actual distribution of points and, therefore, equation C.2 could be applied to find the optimum distribution to achieve the least error on the Kármán constant estimation.

Acknowledgements

This thesis is a collection of many works that have accompanied my path as a PhD student. I should thank so many people for their support that I have immediately to apologize if I shall not mention all of them.

The first is certainly my supervisor Prof. A. Talamelli which has been of great inspiration during my career. He has always been available to discuss with me many crucial aspects of my coaxial jets research as well as to be an inexhaustible source of new challenges. His simple approach to each complex problem amazes me every time as well as his curiosity and interest in many branches of fluid mechanics.

Prof. H. Alfredsson and Dr. R. Örlü of KTH in Stockholm are also acknowledged. They are both examples of people who love their job and do that with passion. From them I have learned much and I hope to learn more. I have to thank all of them for their patience with me and my modest English level. I am still trying to improve my speech....

Thanks again to Ramis Örlü for his friendship: he has sustained me when he was in Italy and when I was in Sweden. He taught me many technical and non technical things being always kind and clear. He was one of my first tests when I started to cook pizza for someone else. Thank you for the trust!

Thanks to Dr. Jean Daniel Rüedi which is a friend before a scientist. From him, I have learned that good things need great care and efforts. I am proud to had the occasion to work with him on the Oil Film Interferometry since 2008. and I hope to study with him a thousand of other topics.

Prof. G. Buresti is greatly acknowledged for placing the coaxial jet facility to the disposal of the *Second Faculty of Engineering* of the *University of Bologna*.

I have to acknowledge also all the staff of the CICLoPE laboratory in Forlì which have supported me in this PhD: Mr. Andrea Cimarelli, Dr. Alessandro Rossetti, Mr. Paolo Proli, Prof. Elisabetta De Angelis, and Dr. Riccardo Rossi. Thanks to all of them for being a source of inspiration with many technical conversations. Many thanks to Luciano Amadori and Mauro Ricci

for their help in the coaxial jets facility setup as well to Marco Amadori, who encouraged me during my third year with his thesis on coaxial jets instabilities.

Thanks to all my friends just for their friendship.

This thesis is dedicated to my wife Francesca and to my daughter. I love both of you from the deep of my heart.

The last dedication is for the chaos which has always accompanied me in each thought. I am not a person which goes straight to the solution of some problem. Sometimes random paths brings me to a different way with the possibility to see something unexpected: this is not a good quality but neither a bad one...

References

- ABRAMOVICH, G. N. 1963 *The theory of turbulent jets*. Cambridge, MA: The M.I.T. Press.
- ALFREDSSON, P. H., JOHANSSON, A. V., HARITONIDIS, J. H. & ECKELMANN, H. 1988 The fluctuating wall-shear stress and the velocity field in the viscous sub-layer. *Phys. Fluids* **31** (5), 1026–1033.
- ANDERSON, J. D. 1984 *Fundamentals of aerodynamics*. McGraw-Hill.
- ANGELE, K. P., KURIMOTO, N., SUZUKI, Y. & KASAGI, N. 2006 Evolution of the streamwise vortices in a coaxial jet controlled with micro flap-actuators. *J. Turbulence* **7** (73).
- BALARAC, G. & MÉTAIS, O. 2005 The near field of coaxial jets: A numerical study. *Phys. Fluids* **17** (065102).
- BATCHELOR, G. K. 2002 *An introduction to fluid dynamics*. Cambridge university press, UK.
- BATCHELOR, G. K. & GILL, A. E. 1962 Analysis of the stability of axisymmetric jets. *J. Fluid Mech.* **14**, 529–551.
- BECKER, H. A. & MASSARO, T. A. 1968 Vortex evolution in a round jet. *J. Fluid Mech.* **31**, 435–448.
- BOLDMAN, D. R., BRINICH, P. F. & GOLDSTEIN, M. E. 1976 Vortex shedding from a blunt trailing edge with equal and unequal external mean velocities. *J. Fluid Mech.* **75**, 721–735.
- BRADBURY, L. J. S. & KHADEM, A. H. 1975 The distortion of a jet by tabs. *J. Fluid Mech.* **70**, 801–813.
- BRAUD, C., HEITZ, D., ARROYO, G., PERRET, L., DELVILLE, J. & BONNET, J. P. 2004 Low-dimensional analysis, using pod, for two mixing layer-wake interactions. *Int. J. Heat and Fluid Flow* (25), 351–363.
- BROWN, G. L. & ROSHKO, A. 1974 On density effects and large structures in turbulent mixing layers. *J. Fluid Mech.* **64**, 775–816.
- BROZE, G. & HUSSAIN, A. K. M. F. 1996 Transitions to chaos in a forced jet: intermittency, tangent bifurcations and hysteresis. *J. Fluid Mech.* **311**, 37–71.
- BRUUN, H. H. 1995 *Hot-Wire Anemometry: Principles and Signal Analysis*. Oxford University Press.

- BURATTINI, P. 2002 Transitional coaxial jets: Coherent structures dynamics, chaos, and flow control. PhD thesis, University of Pisa.
- BURATTINI, P. & TALAMELLI, A. 2007 Acoustic control of a coaxial jet. *J. Turbulence* **8** (47).
- BURESTI, G. 2000 Strutture fluidodinamiche e miscelamento in prossimità dello sbocco di getti coassiali. *Tech. Rep.* DDIA 2000-20. Dipartimento di Ingegneria Aerospaziale di Pisa.
- BURESTI, G., TALAMELLI, A. & PETAGNA, P. 1994 Experimental characterization of the velocity field of a coaxial jet configuration. *Exp. Therm. Fluid Sci.* **9**, 135–146.
- CHOMAZ, J. M. 2005 Global instabilities in spatially developing flows. *Annual Review Fluid Mechanics* **37**, 357–392.
- CHOMAZ, J. M., HUERRE, P. & REDEKOPP, L. G. 1988 Bifurcations from local to global modes in spatially developing flows. *Phys. Rev. Lett.* **60** (1), 25–28.
- COHEN, J. & WYGNANSKI, I. J. 1987*a* The evolution of instabilities in the axisymmetric jet. part 1. the linear growth of disturbances near the nozzle. *J. Fluid Mech.* **176**, 191–219.
- COHEN, J. & WYGNANSKI, I. J. 1987*b* The evolution of instabilities in the axisymmetric jet. part 2. the flow resulting from the interaction between two waves. *J. Fluid Mech.* **176**, 221–235.
- CORCOS, G. M. & SHERMAN, F. S. 1978 Vorticity concentration and the dynamics of unstable free shear layers. *J. Fluid Mech.* pp. 241–284.
- CORKE, T. C. & KUSEK, S. M. 1993 Resonance in axisymmetric jets with controlled helical-mode input. *J. Fluid Mech.* **249**, 307–336.
- CROW, S. C. & CHAMPAGNE, F. H. 1971 Orderly structure in jet turbulence. *J. Fluid Mech.* **48**, 547–591.
- DA SILVA, C. B., BALARAC, G. & MÉTAIS, O. 2003 Transition in high velocity ratio coaxial jets analysed from direct numerical simulations. *J. Turbulence* **24**.
- DAHM, W. J. A., FRIELER, C. E. & TRYGGVASON, G. 1992 Vortex structure and dynamics in the near field of a coaxial jet. *J. Fluid Mech.* **241**, 371–402.
- DRAZIN, P. G. 1992 *Nonlinear systems*. Cambridge university press, UK.
- DRAZIN, P. G. 2002 *Introduction to Hydrodynamic Instability*. Cambridge university press, UK.
- DRUBKA, R. E., REISENTHIEL, P. & NAGIB, H. M. 1989 The dynamics of low initial disturbance turbulent jets. *Phys. Fluids A* **1** (10), 1723–1735.
- DZIOMBA, B. & FIEDLER, H. E. 1985 Effect of initial conditions on two-dimensional free shear layers. *J. Fluid Mech.* **152**, 419–442.
- ELOFSSON, P. A. & ALFREDSSON, P. H. 1998 An experimental study of oblique transition in plane poiseuille flow. *J. Fluid Mech.* **358**, 177–202.
- FIEDLER, H. E. 1987 Coherent structures. *Advances in Turbulence* pp. 320–336.
- FOUNTAIN, G. O., KHAKHAR, D. V., MEZIC, I. & OTTINO, J. M. 2000 Chaotic mixing in a bounded three-dimensional flow. *J. Fluid Mech.* **417**, 265–301.
- FRENKIEL, F. N. 1949 The influence of the length of a hot wire on the measurements of turbulence. *Phys. Rev.* **75**, 1263–1264.

- GAD-EL-HAK, M., POLLARD, M. & BONNET, J. P. 1998 *Flow Control: Fundamentals and Practices*. Cambridge university press, UK.
- GAMARD, S., JUNG, D. & GEORGE, W. K. 2004 Downstream evolution of the most energetic modes in a turbulent axisymmetric jet at high reynolds number. part 2. the far-field region. *J. Fluid Mech.* **514**, 205–230.
- GEORGE, W. K. 1989 The self-preservation of turbulent flows and its relation to initial conditions and coherent structures. *Advances in Turbulence* .
- HERNAN, M. & JIMENEZ, J. 1982 Computer analysis of a high-speed film of the plane turbulent mixing layer. *J. Fluid Mech.* **119**, 323–345.
- HO, C. M. & HUERRE, P. 1984 Perturbed free shear layers. *Annual Review Fluid Mechanics* **16**, 365–422.
- HUERRE, P. & MONKEWITZ, P. A. 1985 Absolute and convective instabilities in free shear layers. *J. Fluid Mech.* **159**, 151–168.
- HUSSAIN, H. S. & HUSSAIN, A. K. M. F. 1995 Experiments on subharmonic resonance in a shear layer. *J. Fluid Mech.* **304**, 343–372.
- HUSSAIN, A. K. M. F. 1986 Coherent structures and turbulence. *J. Fluid Mech.* **173**, 303–356.
- HUSSAIN, A. K. M. F. & ZAMAN, K. B. M. Q. 1978 The free shear layer tone phenomenon and probe interference. *J. Fluid Mech.* **87**, 349–383.
- HUSSAIN, A. K. M. F. & ZEDAN, M. F. 1978 Effects of the initial condition on the axisymmetric free shear layer: Effect of the initial fluctuation level. *Phys. Fluids* **21** (9), 1475–1481.
- HUTCHINS, N. & MARUSIC, I. 2007 Large-scale influence in near-wall turbulence. *Phil. Trans. Roy. Soc. Lond. A* **365**, 647–664.
- HUTCHINS, N., NICKELS, T. B., MARUSIC, I. & CHONG, M. S. 2009 Hot-wire spatial resolution issues in wall-bounded turbulence. *J. Fluid Mech.* **635**, 103–136.
- IQBAL, M. O. & THOMAS, F. O. 2007 Coherent structure in a turbulent jet via a vector implementation of the proper orthogonal decomposition. *J. Fluid Mech.* **571**, 281–326.
- JEONG, J. & HUSSAIN, A. K. M. F. 1995 On the identification of a vortex. *J. Fluid Mech.* **285**, 69–94.
- JUNG, D., GAMARD, S. & GEORGE, W. K. 2004 Downstream evolution of the most energetic modes in a turbulent axisymmetric jet at high reynolds number. part 1. the near-field region. *J. Fluid Mech.* **514**, 173–204.
- KIWATA, T., ISHII, T., KIMURA, S., OKAJIMA, A. & MIYAZAKI, K. 2006 Flow visualization and characteristics of a coaxial jet with a tabbed annular nozzle. *JSME International Journal Series B* **49**, 906–913.
- KIWATA, T., OKAJIMA, A., KIMURA, S. & ANDO, K. 2001 Flow visualization of vortex structure of an excited coaxial jet. *J. Visualization* **4** (1), 99–107.
- KO, N. W. M. & KWAN, A. S. H. 1976 The initial region of subsonic coaxial jets. *J. Fluid Mech.* **73**, 305–332.
- KOCH, W. 1985 Local instability characteristics and frequency determination on self-excited wake flows. *J. Sound Vib.* **99** (1), 53–83.
- KUNDU, P. K. & COHEN, I. M. 2002 *Fluid Mechanics*, 2nd edn. Academic Press.

- LAIZET, S., LARDEAU, S. & LAMBALLAIS, E. 2010 Direct numerical simulation of a mixing layer downstream a thick splitter plate. *Phys. Fluids* **22**.
- LEPICOVSKY, J., AHUJA, K. K. & BURRIN, R. H. 1985 Tone excited jets, part iii: Flow measurements. *J. Sound Vib.* **102**, 71–91.
- LIGRANI, P. M. & BRADSHAW, P. 1987 Spatial resolution and measurement of turbulence in the viscous sublayer using subminiature hot-wire probes. *Exp. Fluids* **5**, 407–417.
- MEHTA, R. D. 1991*a* Effect of velocity ratio on plane mixing layer development: Influence of the splitter plate wake. *Exp. Fluids* **10**, 194–204.
- MEHTA, R. D. 1991*b* Effect of velocity ratio on plane mixing layer development: Influence of the splitter plate wake. *Exp. Fluids* **10**, 194–204.
- MEUNIER, P. & VILLERMAUX, E. 2003 How vortices mix. *J. Fluid Mech.* **476**, 213–222.
- MICHALKE, H. 1965 On spatially growing disturbances in an inviscid shear layer. *J. Fluid Mech.* **23**, 521–544.
- NICKELS, T. B. & MARUSIC, I. 2001 On the different contributions of coherent structures to the spectra of a turbulent round jet and a turbulent boundary layer. *J. Fluid Mech.* **448**, 367–385.
- OLSEN, W. & KARCHMER, A. 1976 Lip noise generated by flow separation from nozzle surfaces. *AIAA J.* (76-3).
- ÖRLÜ, R. & ALFREDSSON, P. H. 2010 On spatial resolution issues related to time-averaged quantities using hot-wire anemometry. *Exp. Fluids* .
- ÖRLÜ, R., SEGALINI, A., ALFREDSSON, P. H. & TALAMELLI, A. 2008*a* On the passive control of the near-field of coaxial jets by means of vortex shedding. In *Proc. of the Int. Conf. on Jets, Wakes and Separated Flows, ICJWSF-2008, September 16–19, 2008, Technical University of Berlin, Berlin, Germany*.
- ÖRLÜ, R., SEGALINI, A., ALFREDSSON, P. H. & TALAMELLI, A. 2008*b* Passive control of mixing in a coaxial jet. In *Proceedings of ETMM7 conference*.
- OTTINO, J. M. 1990 Mixing, chaotic advection and turbulence. *Annual Review Fluid Mechanics* **22**, 207–253.
- PANCHAPAKESAN, N. R. & LUMLEY, J. L. 1993 Turbulence measurements in axisymmetric jets of air and helium. part 1. air jet. *J. Fluid Mech.* **246**, 197–223.
- POPE, S. B. 2000 *Turbulent flows*. Cambridge university press, UK.
- REHAB, H., VILLERMAUX, E. & HOPFINGER, E. J. 1997 Flow regimes of large-velocity-ratio coaxial jets. *J. Fluid Mech.* **345**, 357–381.
- REYNOLDS, O. 1883 An experimental investigation of the circumstances which determine whether the motion of water shall be direct or sinuous, and of the law of resistance in parallel channels. *Phil. Trans. Roy. Soc. Lond. A* **174**, 935–982.
- RIBEIRO, M. M. & WHITELAW, J. H. 1980 Coaxial jets with and without swirl. *J. Fluid Mech.* **96**, 769–795.
- ROSHKO, A. 1976 Structure of turbulent shear flows: A new look. *AIAA J.* **14**, 1349–1357.
- SCHLICHTING, H. 1968 *Boundary layer theory*, 7th edn. McGraw-Hill.
- SCHMID, P. J. & HENNINGSON, D. S. 2001 *Stability and Transition in Shear Flows*. New York: Springer-Verlag.

- SCHOPPA, W. & HUSSAIN, A. K. M. F. 2002 Coherent structure generation in near-wall turbulence. *J. Fluid Mech.* **453**, 57–108.
- SEGALINI, A., ÖRLÜ, R., ALFREDSSON, P. H. & TALAMELLI, A. 2008 The effect of oblique waves on jet turbulence. In *Progress in Turbulence III*, , vol. 131, pp. 231–234. Springer.
- SEGALINI, A. & TALAMELLI, A. 2007 The role of vortex shedding in the mixing of coaxial jets. In *Proc. of the AIDAA Congress, 17-21 September, 2007 Forlì, Italy*.
- STRANGE, P. J. R. & CRIGHTON, D. G. 1983 Spinning modes on axisymmetric jets. part 1. *J. Fluid Mech.* **134**, 231–245.
- SUZUKI, Y. & KASAGI, N. 1992 Evaluation of hot-wire measurements in wall shear turbulence using a direct numerical simulation database. *Exp. Therm. Fluid Sci.* **5**, 69–77.
- TALAMELLI, A. & GAVARINI, I. 2006 Linear instability characteristics of incompressible coaxial jets. *Flow Turbulence Combust.* .
- TANG, S. K. & KO, N. W. M. 1994 Experimental investigation of the structure interaction in an excited coaxial jet. *Exp. Therm. Fluid Sci.* **8** (3), 214–229.
- TONG, C. & WARHAFT, Z. 1994 Turbulence suppression in a jet by means of a fine ring. *Phys. Fluids* **6**, 328–333.
- VAN DYKE, M. 1982 *An Album of Fluid Motion*. Parabolic Press.
- VILLERMAUX, E. & REHAB, H. 2000 Mixing in coaxial jets. *J. Fluid Mech.* **425**, 161–185.
- WALLACE, D. & REDEKOPP, L. G. 1992 Linear instability of wake-shear flows. *Phys. Fluids* **4** (1), 189–191.
- WANG, A. B., TRÀVNÍČEK, Z. & CHIA, K. C. 2000 On the relationship of effective reynolds number and strouhal number for the laminar vortex shedding of a heated circular cylinder. *Phys. Fluids* **12** (6), 1401–1410.
- WICKER, R. B. & EATON, J. K. 1994 Near field of a coaxial jet with and without axial excitation. *AIAA J.* **32**, 542–546.
- WINANT, C. D. & BROWAND, F. K. 1974 Vortex pairing:the mechanism of turbulent mixing-layer growth at moderate reynolds number. *J. Fluid Mech.* **63**, 237–255.
- ZAMAN, K. B. M. Q. & HUSSAIN, A. K. M. F. 1980 Vortex pairing in a circular jet under controlled excitation. part 1. general jet response. *J. Fluid Mech.* **101**, 449–491.
- ZAMAN, K. B. M. Q. & HUSSAIN, A. K. M. F. 1981 Turbulence suppression in free shear flows by controlled excitation. *J. Fluid Mech.* **103**, 133–159.
- ZAMAN, K. B. M. Q. & HUSSAIN, A. K. M. F. 1984 Natural large-scale structures in the axisymmetric mixing layer. *J. Fluid Mech.* **138**, 325–351.
- ZHOU, J., ADRIAN, R. J., BALACHANDAR, S. & KENDALL, T. M. 1999 Mechanisms for generating coherent packets of hairpin vortices in channel flow. *J. Fluid Mech.* **387**, 353–396.